VRIJE
UNIVERSITEIT
BRUSSEL

Faculty of Sciences and Bio Engineering Sciences
Department of Bio Engineering Science
Research group of In Vivo Cellular and Molecular Imaging (ICMI), faculty of Medicine and Pharmacy
Research Group of Cellular and Molecular Immunology (CMIM), faculty of Sciences and Bio Engineering Sciences

Master thesis submitted in fulfilment of the requirements to obtain the degree of Master of Science in Bio Engineering Sciences – Cell and Gene Biotechnology

GENERATION AND VALIDATION OF NANOBODIES TARGETING BRAIN TUMORS WITH ABERRANT EXPRESSION OF EPIDERMAL GROWTH FACTOR RECEPTOR AND HUMAN EPIDERMAL GROWTH FACTOR RECEPTOR 2

HELEEN HANSSENS
Academic year 2017-2018

Promotor: Prof. Dr. Nick Devoogdt
Faculty of Medicine and Pharmacy

Co-promotor: Prof. Dr. Serge Muyldermans
Faculty of Sciences and Bio Engineering Sciences

Supervisor: Janik Puttemans

Faculty of Sciences and Bio Engineering Sciences
Department of Bio Engineering Science
Research group of In Vivo Cellular and Molecular Imaging (ICMI), faculty of Medicine and Pharmacy
Research Group of Cellular and Molecular Immunology (CMIM), faculty of Sciences and Bio Engineering Sciences

Master thesis submitted in fulfilment of the requirements to obtain the degree of Master of Science in Bio Engineering Sciences – Cell and Gene Biotechnology

GENERATION AND VALIDATION OF NANOBODIES TARGETING BRAIN TUMORS WITH ABERRANT EXPRESSION OF EPIDERMAL GROWTH FACTOR RECEPTOR AND HUMAN EPIDERMAL GROWTH FACTOR RECEPTOR 2

HELEEN HANSSENS
Academic year 2017-2018

Promotor: Prof. Dr. Nick Devoogdt
Faculty of Medicine and Pharmacy

Co-promotor: Prof. Dr. Serge Muyldermans
Faculty of Sciences and Bio Engineering Sciences

Supervisor: Janik Puttemans

Copyright

Promotor
Prof. Dr. Nick Devoogdt

Co-promotor
Prof. Dr. Serge Muyldermans

Supervisor
Janik Puttemans

Author
Heleen Hanssens

Acknowledgements

I would like to express my gratitude to the many people who have given me the opportunity to work on a project that has been enormously interesting, compelling and challenging at the same time.

A first very important person during this master thesis was my supervisor Janik Puttemans. I would like to sincerely thank him for allowing me to participate in such an important project and to teach me all the laboratory knowledge, not only in theory, but also with great care in practice. Thank you, Janik, for being constantly willing to listen and to discuss the project, and to strengthen my passion for scientific research in that way.

I also want to thank my promotor, Professor Nick Devoogdt, the person who gave me the opportunity and the possibilities to work on a project at the In Vivo Cellular and Molecular Imaging (ICMI) research group. He has always encouraged me to get the best out of the project, and his insights and perspectives have often helped me forward.

Thirdly, my thanks go to my co-promotor, Professor Serge Muyldermans, for sharing the nanobody expertise and conveying such groundbreaking insights and knowledge with incredible enthusiasm. I would also like to thank Professor Jo Van Ginderachter. His enthusiastic narrative skills during immunology and vaccination technology lessons have awakened my passion for medical biotechnology. He is also the person who listened to my interest in applied projects, and in this way guided me to this fascinating research topic for my master thesis.

Not to be forgotten are the many people at both the ICMI and CMIM laboratories, who were always happy to help, listen to my questions and discuss obtained results. I would like to especially thank Ema Romão, who has directed me forward with her knowledge and explicative skills, and who has very often taken the time to help me with my project. I also want to thank Jessica Bridoux, Henri Baudhuin and Pieterjan Debie for their assistance in certain tests and for sharing their insights.

I thank my class mates, for lending an ear from time to time. In particular, I would like to thank Rani Destrijcker, Nele Van Vaerenbergh, Stefan Verbeeck, Anaïs St-Martin and Pauline Bardet, the class mates who also performed their master thesis at the CMIM laboratory, for being ready to discuss any progresses or struggles in the lab.

List of abbreviations

Abbreviations	
^{18}F-FDG	[^{18}F] fluoro-2-deoxyglucose
^{99m}Tc	Technetium-99 metastable
^{111}In	Indium-111
^{177}Lu	Luthetium-177
AP	Alkaline phosphatase
ATP	Adenosine triphosphate
BBB	Blood-brain barrier
BCBM	Breast cancer brain metastases
BiTEs	Bispecific T-cell engagers
BLI	Bioluminescence imaging
BTB	Blood-tumor barrier
CAR	Chimeric antigen receptors
CDR	Complementarity determining region
CH	Constant parts of the heavy chain of an antibody
CHO	Chinese Hamster Ovarian
CL	Constant parts of the light chain of a conventional antibody
CMIM	Cellular and Molecular Immunology
CNS	Central nervous system
CSF	Cerebral spinal fluid
CT	Computed Tomography
DMEM	Dulbecco's Modified Eagle Medium
DPBS	Dulbecco's Phosphate-Buffered Saline
DTPA	Diethylenetriaminepentaacetic acid
ECF	Extracellular fluid
EGFR	Epidermal growth factor receptor
EGFRvIII	Epidermal growth factor receptor variant three
ELISA	Enzyme-Linked Immunosorbent Assay
FACS	Fluorescence-activated cell sorting
FBS	Fetal Bovine serum
FLI	Fluorescence imaging
Fluc	Firefly Luciferase
Fv	Variable part of a conventional antibody
GBM	Glioblastoma multiforme
GFP	Green Fluorescent Protein
HA	Hemagglutinin
HCAbs	Heavy Chain Antibodies
H-Chain	Heavy polypeptide chains of a conventional antibody
HER	Human Epidermal growth factor Receptor
His-tag	Hexahistidine tag
HPLC	High-performance liquid chromatography
ICMI	In vivo Cellular and Molecular Imaging
IMAC	Immobilized Metal Affinity Chromatography
IP	Intraperitoneal
IPTG	Isopropyl β-D-1-thiogalactopyranoside
iTLC	Instant thin layer chromatography
IV	Intravenous
k_a	Association constant
k_d	Dissociation constant
K_D	Equilibrium constant
KLH	Keyhole limpet hemocyanin
L-Chain	Light polypeptide chains of a conventional antibody
LET	Linear energy transfer
mAb	Monoclonal antibody
MGMT	O^6-methylguanine DNA methyltransferase
MMR	DNA mismatch repair system
MRI	Magnetic resonance imaging
MW	Molecular weight
Nb	Nanobody
NIR	Near-infrared
OD	Optical density
PBS	Phosphate buffered saline
PCR	Polymerase chain reaction
PE	Phycoerythrin
PET	Positron emission tomography
pI	Iso-electric point
p.i.	Post injection
QoL	Quality of life
ROI	Region of interest

RPMI	Roswell Park Memorial Institute
ScFv	Single chain Fv
SDS-PAGE	Sodium dodecyl sulfate Polyacrylamide gel electrophoresis
SEC	Size-exclusion chromatography
SEM	Standard error of mean
SPECT	Single-photon emission computed tomography
su	Suppressor strain
TKI	Tyrosine kinase inhibitors
TMZ	Temozolomide
TRNT	Targeted radionuclide therapy
VH	Variable domain of the heavy chain of an antibody
VL	Variable domain of the light chain of an antibody
WHO	World Health Organization
wt	Wild type

Units

Da	Dalton
h	hours
eV	electron Volt
MW	Molecular weight
AU	Absorbance units
IA	Injected activity
M	mole/l
rpm	rotations per minute
bp	base pairs
g	gravitational force
Ci	Curie

Amino acids

Alanine	Ala	A
Arginine	Arg	R
Asparagine	Asn	N
Aspartic acid	Asp	D
Cysteine	Cys	C
Glutamic acid	Glu	E
Glutamine	Gln	Q
Glycine	Gly	G
Histidine	His	H
Isoleucine	Ile	I
Leucine	Leu	L
Lysine	Lys	K
Methionine	Met	M
Phenylalanine	Phe	F
Proline	Pro	P
Serine	Ser	S
Threonine	Thr	T
Tryptophan	Trp	W
Tyrosine	Tyr	Y
Valine	Val	V

Table of contents

1. Introduction

The brain is a very complex organ, in which a strictly maintained homeostasis is of crucial importance for a normal and healthy life. This homeostasis is to a large extent achieved by the blood-brain barrier (BBB); a barrier that is mainly made up of tight junctions in between endothelial cells in the capillaries of the brain. These junctions restrict the passage of molecules from the peripheral circulation to the brain and limit the infiltration of circulating antibodies. This characteristic makes the brain an immune-privileged site, in which pathogens and diseases such as cancer can be hidden from the immune system.

Cancer is a prevalent disease, that can derive from any tissue type. Due to its immune-privileged nature, the brain is an organ in which disease management is more challenging. In the United States of America, the incidence of primary brain tumors in adults is estimated to be about 28,6/100 000. The most common and most lethal of these primary brain tumors is glioblastoma multiforme (GBM), which is a glial cell-derived cancer of the highest grade (grade IV). In many cases of GBM, epidermal growth factor receptor (EGFR/*ErbB-1*) is overexpressed and/or expressed in a mutated form. The most common mutant receptor in glioblastoma is the mutant variant three receptor, abbreviated EGFRvIII. This variant receptor arises from an in-frame deletion of six exons in the extracellular part, resulting in a peptide stretch that does not occur on the wild type receptor and is therefore not present in healthy tissues.

This tumor-exclusivity is of special importance in immunotherapy approaches, since any expression of the target molecule on non-tumorous tissue, leads to toxic side-effects. Antibodies directed specifically against the EGFRvIII protein have been developed, but are yet to be introduced in clinical trials due to intellectual property restrictions. Other antibodies that recognize both the wild-type and the mutated form of the receptor have been evaluated in clinical trials, but have failed to prove their therapeutic relevance in patients with high-grade glioma so far.

Another important type of brain-localized tumors, are metastases from cancers that derive from other tissue types. Breast cancer is the second most commonly diagnosed cancer type worldwide and makes up about one fourth of the cancer diagnoses in women. Metastases to

the brain are relatively common, especially if the tumor is overexpressing the human epidermal growth factor receptor 2 (HER2/*ErbB-2*). This might be partially due to the therapeutic approach in case of this phenotype, which consists of anti-HER2 antibody-based immunotherapy, amongst other approaches. The frequency of brain metastasis could be a consequence of the size of these conventional antibodies, which are too large to trespass the tight junctions in the BBB and to reach the brain, making it a therapy-resistant environment and potentially a preferred site for metastasis. The effect of antibodies that do reach the tumor might also be dampened by a suppressive micro-environment in the brain.

Smaller antibody fragments have many advantages over complete antibodies, most of which are related to their size. Antigen recognition can be achieved by using only the small antigen-binding part of the antibody. Problem remains that this antigen-binding part is made up of two domains that are matured as a whole *in vivo*, but of which the combination gets lost during DNA amplification. This renders the recovery of naturally-generated high affinity constructs very complex and labor-intensive.

In the blood of *Camelidae*, such as camels and alpacas, an atypical antibody format naturally occurs. These so-called heavy-chain-only antibodies (HCAbs) lack a light chain and therefore have an antigen-binding paratope that is present in only one domain and one gene product, instead of two, making the antigen-binding fragment smaller and easier to recover from a pool of lymphocytes. This fragment is what is commercially called a nanobody, referring to its small size.

Like antibodies, nanobodies can be labeled with either diagnostic or therapeutic compounds and after intravenous administration, they accumulate at antigen-expressing disease lesion sites. The main advantage of nanobodies over antibodies in this context is their quick distribution and elimination from the body.

In this master thesis project, the potential of nanobodies in the context of brain tumors will be evaluated. To do so, two models will be considered, both expressing a target antigen of the *ErbB* family of tyrosine kinase receptors in aberrant form. For the GBM model, two targets are considered. The first target is EGFRvIII, for which no exclusively binding nanobody has been reported. The second target is the wild-type EGF-receptor, which is overexpressed in

many cases of the disease. An EGFR-binding nanobody has been developed and will be validated in a preclinical model of glioma.

The second model that will be considered is brain-metastatic breast cancer with overexpression of HER2. Nanobodies targeting this receptor have been successfully developed. *In vivo* tests on animals with intracranial breast cancer-derived tumors should give preliminary insights of this nanobody's potential in the case of breast cancer brain metastasis.

2. Literature study

2.1. Glioblastoma multiforme

2.1.1. Introduction and epidemiology

In 2012, 257,000 people worldwide were diagnosed with a cancer of the brain or central nervous system (CNS) (Ferlay, et al., 2015), and it is believed that today, 700,000 people in the USA are living with a primary brain tumor (National Brain Tumor Society, 2018). Most of the primary brain tumors that are found in humans are gliomas, and most of these are diffuse gliomas (glial tumors). The World Health Organization (WHO) categorizes gliomas according to the cell type from which they are derived and the malignancy grade they have (Louis, et al., 2007). The most prevalent and most life-threatening form of gliomas is glioblastoma multiforme (GBM), an astrocytoma of the highest grade – grade IV (Wen & Kesari, 2008). This cancer derives from glial cells of the CNS, namely astrocytes, which are glial cells that function as a nourishing, supporting and protective layer for nerves in the brain (Sanai, et al., 2005).

Grade III and grade IV gliomas, together categorized as high-grade gliomas, are the most prevalent tumors that originate in the brain in human adults. GBM makes up 80-90 % of the grade IV brain tumors and 40-45 % of all high-grade gliomas. Without therapy, survival time rarely exceeds 3 months. This makes GBM the most prevalent and most lethal brain tumor, accounting for 50-60% of all astrocytic tumors (Bruce & Kennedy, 2017) (Henriksson, et al., 2011) (Bruce, et al., 2009).

2.1.2. Current treatment

2.1.2.1. Standard treatment

Current treatment of glioblastoma consists of surgery followed by radiation and temozolomide (TMZ, Temodal®) chemotherapy. Survival time after this standard treatment is 15 months on average for firstly diagnosed brain tumors and up to 7 months for relapse cases (Johnson & O'Neill, 2012) (Henriksson, et al., 2011).

The life expectancy of GBM patients depends on multiple factors including the size of the tumor and its location, since an important step in current therapies is surgery. Because of the

delicate nature of the brain, tumor resection in specific zones is more reasonable than in other regions. In for example brainstem-located tumors, radiotherapy is a more acceptable option than surgery. A combination of radio-, and chemotherapy with surgery has a higher success rate than any of these administered alone (Walid, 2008).

TMZ is an alkylating agent, which is only stable at acidic pH, making oral administration possible. When the compound reaches the blood or the tissue, it will undergo a ring-opening event to form 3-methyl-(triazen-1-yl) imidazole-4-carboxamide, the biologically active compound. When in contact with H_2O, this compound will break down into 5-aminoimidazole-4-carboxamide and a methyldiazonium cation. The cation can methylate purines within the DNA at O^6 and N^7 positions of guanine bases and at N^3 on adenine bases. Methylated O^6 guanine induces expression of the death receptor and activates the mitochondrial pathway for apoptosis. This occurs because any attempts of the cell in repairing the alkylations result in DNA breaks (Messaoudi, et al., 2015) (Agarwala & Kirkwood, 2000).

Therapeutic properties of TMZ arise from its physicochemical characteristics. It is a small (194 Da) and very lipophilic molecule. This allows efficient absorption in the digestive tract after oral administration, and most importantly a good transport over the blood-brain barrier (BBB). Up to 30-40% of the concentration in the blood accumulates in the CNS (Agarwala & Kirkwood, 2000).

Intracranial tumors usually cause damage to the neurocognitive functioning of the patient, which results in emotional, intellectual and behavioral issues and an important decrease in quality of life (QoL). Tumor resection usually improves the QoL, while radiotherapy decreases it as it evokes hair loss, fatigue, drowsiness and mental problems. TMZ does not negatively affect the QoL, except in terms of social functioning. In other domains, TMZ causes a slight QoL improvement, as long as the disease regresses (Henriksson, et al., 2011). Despite slight improvements in therapy success rates have been noted since the use of TMZ, relapses are very frequently observed. They are observed in 68 % - 79 % of the cases. Altogether, GBM is a frequently diagnosed disease, with a very poor prognosis, as current therapies do not prevent relapse and a real cure does not exist. This leaves a highly unmet clinical need (Sherriff, et al., 2013).

2.1.2.2. Problems with therapy resistance

Several mechanisms of resistance to TMZ can occur. A first of these is the occurrence of highly activated O^6-methylguanine DNA methyltransferase (MGMT) in cancer cells, due to a

reduced methylation status of its promotor (Park, et al., 2012). MGMT is a protein that removes methyl and other alkyl groups from the DNA, and therefore it undoes the cytotoxic effect of TMZ.

In new GBM patients, 55% of the cases show hypo-methylation of the MGTM promotor, indicating reduced sensitivity to TMZ treatment (Hegi, et al., 2005). Because of this high prevalence rate, MGMT inhibitors such as O (6)-benzyl guanine and O (6)-[4-bromothenyl]guanine have been tested for their relevance in restituting the TMZ activity. These kinds of molecules however show toxicity in normal cells as well, since MGMT activity is lowered there as well, leading to a toxic effect from TMZ (Messaoudi, et al., 2015).

Another mechanism of TMZ resistance occurs when MGMT is not present, and therefore the O^6 guanine bases are persistently methylated. The methylated guanine will base pair incorrectly with thymine instead of cytosine. The DNA mismatch repair system (MMR) recognizes this as a mistake and will lead the cell towards apoptosis, resulting in a positive outcome for cancer treatment. If however alterations occur in proteins of the MMR pathway, this signal for apoptosis can no longer occur and cellular growth will not be stopped, leading to non-efficacy of the alkylating drug. Selection for these mutations occurs while TMZ therapy is performed (Messaoudi, et al., 2015) (Yip, et al., 2009).

A third mechanism to undo the DNA modifying effects of TMZ, is the base excision repair pathway (BER). This pathway in responsible for the repair of DNA modifications on N^3 and N^7 positions and plays a less significant role in the resistance to TMZ therapy (Messaoudi, et al., 2015).

As the success of current treatment remains rather low, a more targeted approach is needed, in which markers of GBM are used to distinguish cancer cells from healthy cells. In this way, diseased cells can be specifically targeted, damaged or killed.

2.1.3. Epidermal Growth Factor Receptor

In many cancerous tissues, such as glioblastoma as well as cancers of the neck, colon and lung, epidermal growth factor receptor (EGFR), a tyrosine kinase, is overexpressed compared to normal cells and therefore is a useful property to distinguish between tumorous and non-tumorous tissue. This overexpression occurs in 34-63 % of all GBM (Gan, et al., 2013).

EGFR belongs to the *ErbB* family of tyrosine kinases, which is a class of growth factor receptors, consisting of four proteins: EGFR/*ErbB-1* and Human Epidermal growth factor

Receptors 2 to 4 (HER2/*ErbB-2*, HER3/*ErbB-3* and HER4/*ErbB-4*). These proteins bind growth factors and other ligands with their extracellular domain and onset an intracellular signalization as a consequence (Yarden, 2001).

Binding of natural ligands to these receptors induces homo- or heterodimerization. This leads to a conformational change in the receptor upon which receptor-receptor interactions become possible. The residues needed for this interaction are conserved in the *ErbB* family of tyrosine kinase receptors (Garrett, et al., 2002). After ligand binding and dimerization, an autophosphorylation occurs on the receptors' intracellular tyrosine residues. Consequently, these newly phosphorylated residues are binding sites for intracellular proteins, inducing the activation of several signaling pathways, which ultimately result in cell survival and proliferation. With normal expression levels of EGFR, these signaling pathways make sure that a normal growth rate of cells is maintained (Yarden, 2001).

The intracellular autophosphorylation is achieved by the action of tyrosine kinases. Several tyrosine kinase inhibitors (TKIs) have been developed to inhibit oncogenic effects of the altered EGFR signaling in cancer. The first generation of TKIs consists of ATP analogues that bind the ATP binding pockets in a reversible way, and thereby inhibit intracellular signaling that results in proliferation. Later generations (generation two and three) bind the same pocket irreversibly. Examples of first generation TKIs are gefitinib, erlotinib and lapatinib, second generation TKIs comprise afatinib and dacomitinib and third generation TKIs include rociletinib and AZD9291 (Seshacharyulu, et al., 2012) (An, et al., 2018).

2.1.4. Mutations in the Epidermal Growth factor Receptor in cancer

Out of all EGFR-overexpressing cancers, 63-75 % also show genomic rearrangements in the *ErbB-1* gene encoding the EGFR protein, resulting in cancer cells that express both a wild-type form of the receptor and a mutated form (Gan, et al., 2013).

Multiple mutations are known to frequently occur in the EGFR-protein in several cancer types. In for example non-small cell lung cancer, mutations in the tyrosine kinase domain (exons 19-21) are frequently observed. In GBM however, these are infrequent mutations. Deletion mutations, referred to as variants, are more often perceived in glioblastoma. (Furnari, et al., 2015).

Variants I to III contain a deletion in the extracellular part of the protein, while variants IV and V contain an intracellular deletion. Of these mutant forms, EGFR variant II and III show

constitutive signaling activity and therefore they contribute to the oncogenic character of the tumor (Furnari, et al., 2015).

First generation TKIs have shown beneficial effects on therapy outcome in non-small cell lung cancer, but have a much smaller effect in the case of GBM. A possible explanation for this is the fact that these drugs work better in cancers that express mutations in exons 19-21 (Slobbe, et al., 2015), which are rare in GBM. Second and third generation TKIs show potential in the treatment of GBM in preclinical trials (Zahonero, et al., 2015), but clinical data concerning their effect in glioblastoma patients are not yet available (An, et al., 2018).

2.1.5. Epidermal Growth factor Receptor variant III in glioblastoma

The most common receptor variant in GBM, EGFR-variant three (EGFRvIII), is found in well over 25 % of all glioblastoma. This mutant shows an in-frame deletion of exons 2-7 in the EGF-receptor, resulting in a receptor lacking a part of its extracellular domain. The occurrence of this receptor variant is in almost all cases associated with EGFR gene amplification and protein overexpression (Gan, et al., 2013).

EGFRvIII expression is unique to tumor cells. The same is not true for wt EGFR; this receptor is often overexpressed in tumor tissues, but also occurs in healthy tissues (Gan, et al., 2013). Compared to wt EGFR, EGFRvIII lacks a great part of the protein's extracellular (ligand-binding) domain. The mutant has a molecular weight of 145 kDa, compared to the 170 kDa molecular weight of the wild-type receptor. This arises from the in-frame deletion of several exons and the resulting absence of 801 bp and the 267 matching amino acids. As a consequence of the disappearance of amino acids 6 through 273, a glycine appears at the new junction site at position 6. This generates a unique and reachable peptide sequence (**figure 2.1 and 2.2**) (Wikstrand, et al., 1998).

The introduction of the EGFRvIII gene in glioblastoma cells has shown to augment cell proliferation rate and invasiveness, while it lessens the degree of apoptosis. It therefore contributes to the tumorigenic potential of GBM cells (Lal, et al., 2002) (Nagane, et al., 1996).

In a relatively large-scale study, the relationship between EGFR status and survival was evaluated in 87 GBM patients. An important correlation was found between the occurrence of EGFR gene amplification and corresponding protein overexpression (Shinojima, et al., 2003).
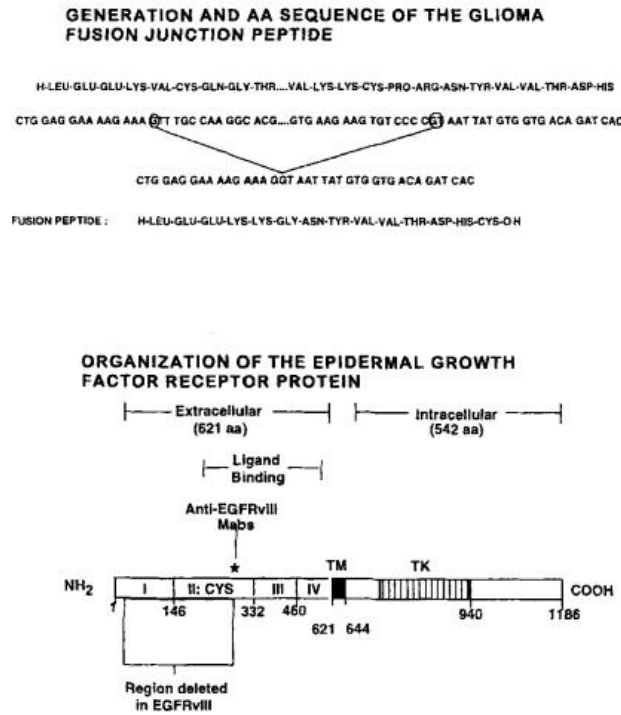
Figure 2.1: Representation of the genetic deletion in the EGFRvIII mutant receptor. *Exons two until seven are deleted. This results in a 25kDa deleted extracellular part of the receptor. The in-frame deletion of this extracellular part results in a novel and unique glycine residue at the new junction site. Figure retrieved from (Wikstrand, et al., 1998).*
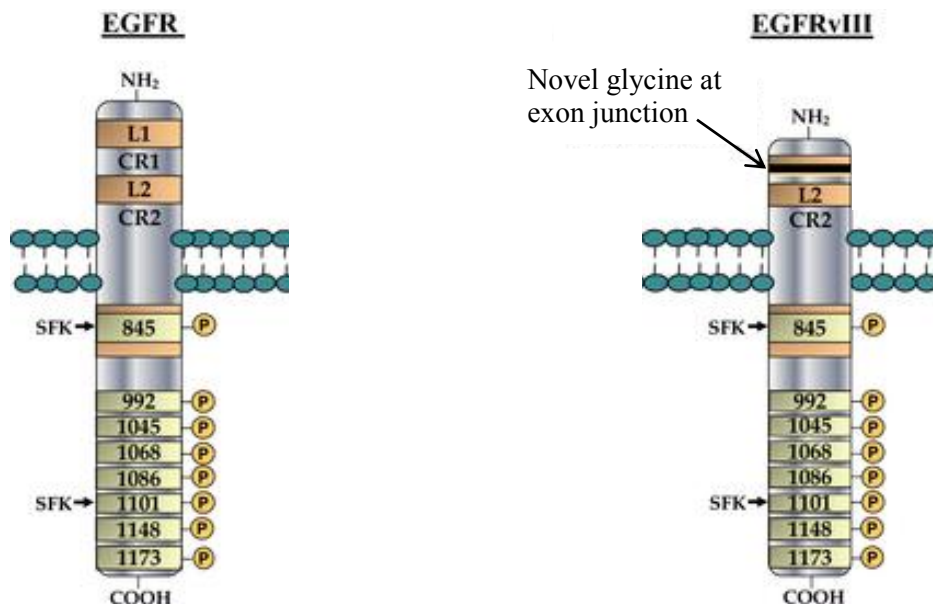
Figure 2.2: Comparison of the EGFR protein and the variant form. *Intracellularly, both receptors are identical and phosphorylation points remain unaltered. On the extracellular side a large part is missing in EGFRvIII, resulting in ligand independency and continuous intracellular phosphorylation. A unique peptide is present in this receptor mutant. Figure adapted from (Gan, et al., 2013).*

Also, the occurrence of EGFRvIII was detected in 45 % of the patients with a wt EGFR gene amplification and only in 8.5 % of the patients without this genetic amplification. It was shown that the amplification of EGFR expression is a sign of poor survival. In patients with this overexpression, the subgroup that had an additional presence of the EGFRvIII, showed the worst survival rates (Shinojima, et al., 2003).

2.1.6. Comparison of wt EGFR and EGFRvIII signaling

The variant III receptor shows permanent intracellular phosphorylation of tyrosine residues, while the wild-type receptor only shows autophosphorylation after ligand exposure (**figure 2.3**). This constitutive phosphorylation and thus constitutive activation of the signaling pathway is however much lower (± 10 %) than the phosphorylation of the wild-type receptor after ligand binding. Also, no down-regulation of the expression (endocytosis and lysosomal degradation) of the mutated receptor is observed (Huang, et al., 1997).
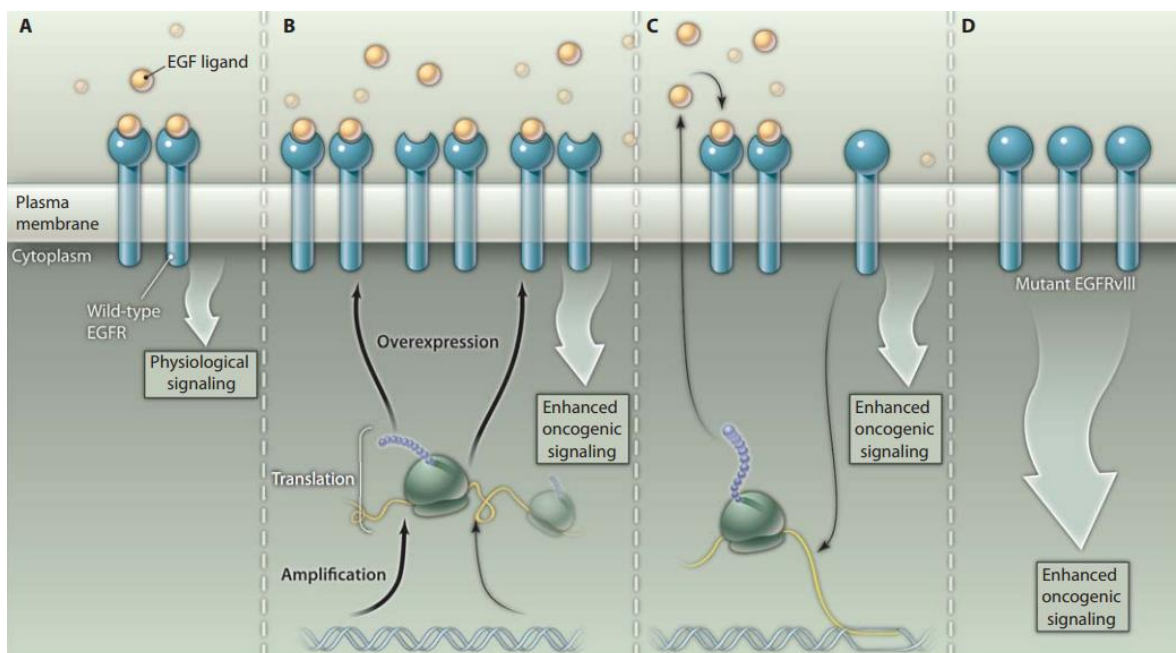
*Figure 2.3: Different alterations in EGFR signaling. A) normal signaling via wt EGFR. This results in normal cellular growth rates. B) Genetic amplification of ErbB1 genes and subsequent receptor overexpression. This leads to enhanced signaling and enhanced growth rates. C) activation of genetic expression of natural ligands of the EGF receptors. This leads to autocrine overactivation of receptor signaling. D) Some receptor mutants lead to constitutive activation of receptor signaling that is independent of ligand binding. One of those mutations is the EGFRvIII receptor. Figure retrieved from (Huang, et al., 2009).*

If the mutant form of EGFR and the wt form are co-expressed, a dimerization can occur and this can lead to wt EGFR activation after trans-phosphorylation. Trans-phosphorylation is observed because the wild-type receptor shows phosphorylation in a ligand independent manner in EGFRvIII$^+$ cells. The formation of such heterodimers increases tumor development by reducing cell death (Luwor, et al., 2004).

EGFR mostly signals through enhanced phosphorylation of STAT3 and a mild activation of the Ras-Raf-MEK-Erk1/2 pathway. The Cb1 protein is also activated and recruited to the phosphorylated receptor, leading to poly-ubiquitination, receptor internalization and degradation. This while the variant form of EGFR, which shows permanent intracellular phosphorylation, over-activates the Ras-Raf-MEK pathway and PI3K-Akt-mTor pathway signaling, often in combination with a loss of PTEN (PI3K-Akt-mTor pathway antagonist). The activation of the Ras-Raf pathway does not lead to high phosphorylation levels of Erk1/2. Therefore, especially signaling through the PI3K-Akt-mTor pathway is enhanced in these EGFRvIII expressing cells. The latter results in high levels of activated Akt, an important effector in the PI3K-Akt-mTor pathway, contributing to rapid cell growth and tumorigenic properties. BCL-X$_L$ is highly activated in the mutant receptor-bearing cells, which contributes to resistance to chemotherapeutics (**figure 2.4**) (Huang, et al., 2009).

In cells expressing the normal EGF receptor, the phosphorylation of Tyr1045, one of the intracellular phosphorylation sites required for signaling, is important for the recruitment of c-Cbl, a ubiquitin ligase. This phosphorylation occurs after extracellular ligand binding. It results in receptor desensitization by the sequential steps of internalization, ubiquitination and degradation. This is however not observed in the variant III form of the receptor, where the crucial Tyr1045 residue is under- or non-phosphorylated, as is observed by blotting experiments with an antibody against phosphorylated Tyr1045. Due to this specific hypo-phosphorylation, downregulation of the truncated receptor is impossible, and enhanced cell growth results from it (Han, et al., 2006).

PTEN, a molecule that is antagonistic for the PI3K pathway is often deleted or mutated in cancers. Its mutation is found to be present in 31% of GBM cell lines (Li, et al., 1997). It is also mutated in 40% of the EGFRvIII$^+$ tumors, which may have a pro-tumorigenic effect *in vivo* by enhancing the PI3K pathway activity (Gan, et al., 2013).
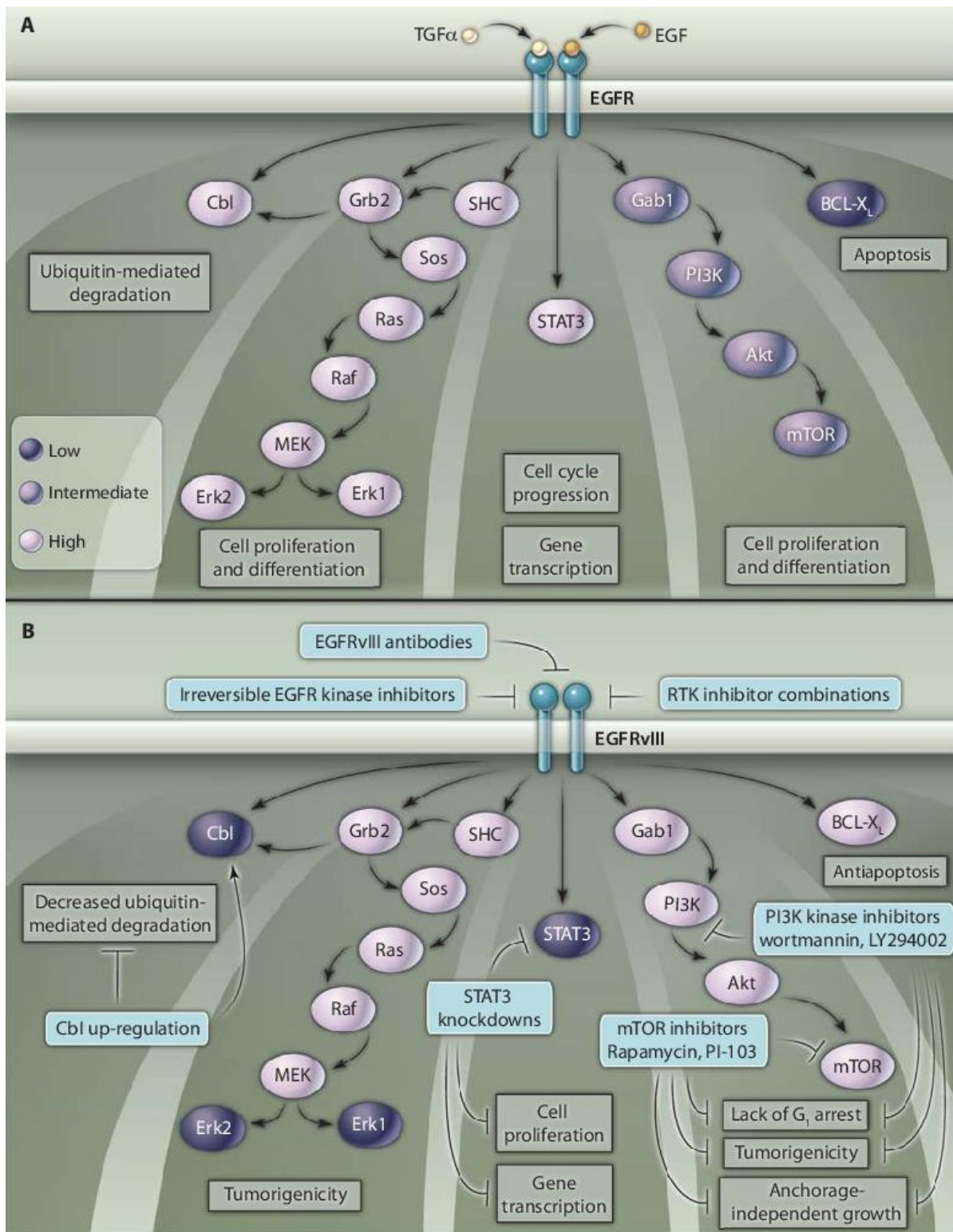
Figure 2.4: Comparison of wt EGFR signaling and mutant EGFR signaling. A) Signaling in wt EGFR mostly occurs via STAT3 phosphorylation, the Ras-Raf-MEK-Erk1/2 pathway and CbI recruitment, leading to receptor desensitization. B) Signaling via the variant III mutant form of the EGF receptor occurs mostly via the PI3K-Akt-mTor pathway. The Ras-Raf-MEK-Erk1/2 pathway is activated as well, but no phosphorylation of Erk1/Erk2 occurs. CbI is not recruited and BCL-X_L is activated. Figure retrieved from (Huang, et al., 2009).

The PI3K pathway, with Akt as a central signaling molecule, enhances the anaerobic glycolysis and also rises lipogenesis (synthesis of cholesterol and fatty acids), which are important metabolic processes in fast growing cancer cells (Gan, et al., 2013).

2.1.7. Exploiting the tumor-specificity of EGFRvIII

Several therapeutic strategies have been developed in the last years that exploit the tumor-specificity of EGFRvIII protein expression. For example, the Rindopepimut[®] vaccine has been constructed based on the unique epitope present in EGFRvIII molecules. This 14-amino acid peptide, PEP-3: H-Leu-Glu-Glu-Lys-Lys-Gln-Asn-Tyr-Val-Val-Thr-Asp-His-Cys-OH is administered to GBM patients with the correct cancer phenotype in a keyhole limpet hemocyanin (KLH) hapten-carrier system in order to generate an immune response and to eliminate reoccurring EGFRvIII^{+} cells in patients after treatment. In this treatment strategy, an immune response is induced in 45% of the patients and EGFRvIII cells that reoccur are eliminated. However, EGFRvIII expression is often lost at reoccurrence and reoccurring tumor cells that overexpress wt EGFR are not eliminated. Since the survival rate in patients that developed anti-EGFRvIII antibodies more than doubled compared to patients that didn't, the generated antibodies must be able to cross the BBB in the tumor microenvironment, possibly due to a disturbed barrier (Sampson, et al., 2010). In a phase 3 clinical trial however, this approach did not show an approved overall survival (Malikki, 2016). In another randomized double-blind phase 3 clinical trial, treatment with PEP3-KLH plus TMZ failed to improve overall survival compared to TMZ alone for newly diagnosed EGFRvIII[+] GBM patients (Weller, et al., 2017).

Since EGFRvIII is a tumor-specific marker, and therefore a very interesting target molecule, several EGFRvIII-specific antibodies have been developed. For example, L8A4 is an antibody that only recognizes the mutant receptor and not the wild-type receptor, and it has proven its preclinical value (Melchers, et al., 2014). Limitations due to intellectual property rights have prevented these antibodies from being tested in clinical trials (Gan, et al., 2013). Other antibodies are known to bind both the mutant receptor and the wild-type form. Of these, cetuximab is the best known. Receptor-binding of cetuximab induces internalization. However, this antibody failed to show beneficial effects for high-grade glioma patients in a phase II clinical trial (An, et al., 2018) (Neyns, et al., 2009). The limited success of these antibody-based approaches is possibly due to the large size of antibodies, which limits both brain and tumor penetration (An, et al., 2018).

Chimeric antigen receptor (CAR) T-cells are T cells that carry a designed receptor, specific for a predetermined antigen. A single chain Fv (scFv), which is the smallest antigen-binding part derived from conventional antibodies with a peptide linker to fuse the two antigen binding domains, that specifically recognizes EGFRvIII can be used as this recombinant T-cell receptor part. The aim of this strategy is to generate Helper T-cells with a designed specificity for EGFRvIII, in order to achieve an optimal anti-cancer immune response. Because this approach showed good results in terms of T-cell proliferation and cytokine secretion, it is currently evaluated in a phase I clinical trial (Johnson, et al., 2015) (U.S. National Library of Medicine, 2018).

Another strategy that is currently investigated to eliminate EGFRvIII[+] cancer lesions, is the use of bispecific T-cell engagers (BiTEs). These are coupled scFv molecules that specifically recognize EGFRvIII with one scFv and the CD3 molecule on T-cells with another scFv. In that way, T-cells are directed specifically to the tumor. These BiTE molecules have shown great results in preclinical studies with regards to tumor elimination and EGFRvIII specificity (Gedeon, et al., 2014).

2.2. Breast cancer

2.2.1. Introduction and epidemiology

In 2012, approximately 1.67 million people were diagnosed with breast cancer worldwide. This made up almost 12 % of all cancer diagnoses. It is the second most common cancer type worldwide, after lung cancer, and in the female population, it is the most frequently diagnosed cancer type. Globally, breast cancer is the fifth most deadly cancer type with approximately 522,000 deaths in 2012 (Ferlay, et al., 2015).

Breast cancers originate from breast tissue, as the result of a loss of control over cellular growth. The breast comprises several tissue types, of which milk production glands (lobules), and ducts that connect the lobules to the nipple are originator tissues for breast cancer. (American Cancer Society, 2015)

2.2.2. Breast cancer: current treatment

First line treatment for breast cancer consists of (combinations of) surgery or resection to remove the bulk tumor mass, radiation therapy and/or systemic chemotherapy. Since these treatments are severely invasive and cause off-target damage to the body, a trend towards a

more tumor-targeted treatment approach is arising (The American Cancer Society Medical and Editorial Content Team, 2017).

2.2.3. Human Epidermal growth factor Receptor 2 in breast cancer

Like EGFR, the HER2 receptor belongs to the *ErbB* family of tyrosine kinases, being the protein product of *ErbB-2* (Yarden, 2001). HER2 is a receptor on epidermal derived cell types, which upon ligand binding and subsequent homo- or heterodimerization allows an autophosphorylation event on the intracellular tyrosine residues. Several signaling molecules can then bind these phosphorylated sites and the signaling cascade that follows enhances the activity of pathways involved in cell reproduction (Iqbal & Iqbal, 2014) (Yarden, 2001).

Non-cancerous cells possess a single copy of the *erbB-2* gene on the 17th chromosome. Overexpression of this receptor (HER2$^+$ phenotype) is observed in approximately 15-30% of breast cancer cases. The copy number of the gene can amplify up to 20 times and the protein expression can rise to a 100-fold of normal expression levels. As with EGFR, the overexpression of this membrane receptor is linked to malignancy rather than to benign cancers. Because the great difference in HER2 expression quantity between normal cells and cancer cells, its accessible localization and its continuous importance during cancer spreading, it is an important target in imaging and therapy (Iqbal & Iqbal, 2014) (Yarden, 2001) (Vaneycken, et al., 2011a) (Hicks & Kulkarni, 2008).

2.2.4. HER2$^+$ breast cancer: current diagnostics

Since HER2 is overexpressed in 15-30 % of the breast cancers, it is an attractive target for cancer discovery and treatment. Existing therapies that use this cancer antigen as a basis for treatment- lapatinib (TKI), trastuzumab (monoclonal antibody, mAb) and pertuzumab (mAb)- require a selection of patients that qualify for having a HER2$^+$ cancer phenotype. This is important since the HER2 receptor is not tumor exclusive, but can be present on certain normal cells, such as cardiomyocytes. A HER2-based treatment could therefore damage healthy heart tissue and may cause unnecessary side effects in patients with HER2$^-$ tumors. Therefore, a tumor phenotype characterization, most often on a biopsy of the original tumor, is needed to determine the expression level of HER2 case by case. This is usually done *in vitro* by immunohistochemistry and/or fluorescent *in situ* hybridization. However, these approaches do not give an accurate view of the overall HER2 status, due to heterogeneity between the primary tumor and metastatic lesions and within lesions (Vaneycken, et al., 2011a) (Hicks & Kulkarni, 2008).

Primary and secondary breast cancer lesions possess the same HER2 status in approximately 94% of the cases. In the non-corresponding cases, both increase and decrease of expression level is possible. If metastatic lesions are easily reachable, separate HER2-status determining tests are therefore warranted (Gancberg, et al., 2002).

In modern HER2^{+} breast carcinoma diagnostics, specific anti-HER2 molecules are coupled to compounds that emit a measurable signal - for example radio-isotopes or fluorescent dyes - which can be used to visualize tumor lesion(s) and localize them throughout the body. This makes it possible to avoid the biopsy step and to get a more systemic representation of the HER2 status in all cancerous regions within the body, allowing a more straightforward screening and an easy follow-up of cancer evolution during treatment (**figure 2.5**) (Vaneycken, et al., 2011a) (Dijkers, et al., 2010) (Debie, et al., 2017) (Becker, et al., 2001).

2.2.5. HER2^{+} breast cancer: current treatment

After diagnosis with a HER2^{+} subtype of breast cancer, standard treatment consists of a combination of several therapeutics: taxane- an inhibitor of mitosis-, trastuzumab (Herceptin®) and pertuzumab (Perjeta®), both monoclonal anti-HER2 antibodies. These drugs can be administered in parallel with standard breast cancer treatment. A next step consists of a treatment with an antibody-toxin conjugate: trastuzumab emtansine (T-DM1, sold under the trade name Kadcyla®). The third-line treatment can be a combination of lapatinib (Tyverb®, TKI) or trastuzumab in combination with other agents, such as other TKIs (Verma, 2014).
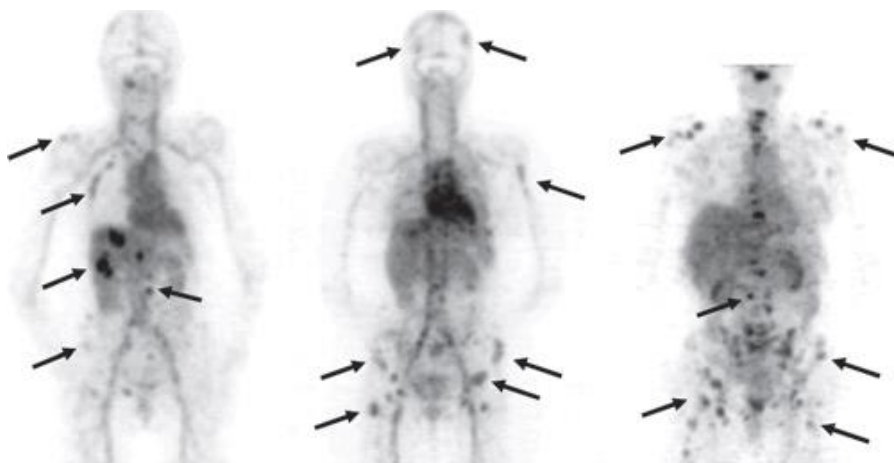

Figure 2.5: Positron emission tomography (PET) images of metastatic HER2^{+} breast cancer patients. *Images were obtained 5 days after intravenous injection of zirconium-89 labeled trastuzumab (anti-HER2 monoclonal antibody). Arrows denote the HER2^{+} lesions. Figure retrieved from (Dijkers, et al., 2010).*

When HER2$^+$ breast cancer patients are treated with standard trastuzumab therapy, beneficial effects are observed on the regression of the primary tumor and in 50% of the cases also in other systemic metastatic sites. A problem with the therapy is however noticed in the brain. Breast cancer brain metastases (BCBM) develop as soon as six months after the initiation of antibody therapy in one fourth to one third of the patients. The increasing percentage of BCBMs observed may be due to the improved management of systemic disease, prolongation of survival, a preference of HER2$^+$ tumors for intracranial localization, or the BBB which is difficult to cross for large molecules like trastuzumab, making the CNS system an immune-privileged site (Bendell, et al., 2003) (Stemmler, et al., 2006) (Kodack, et al., 2015). Other, more recent preclinical and clinical data show that trastuzumab does effectively reach brain tumors, but that its function is undermined in the brain microenvironment (Kabraji, et al., 2018). The latter could still contribute to the brain being a preferred site for metastasis.

2.2.6. Breast cancer brain metastasis

BCBM derived from primary HER2$^+$ breast cancer lesions are observed in up to 50% of metastatic HER2$^+$ breast cancer patients (Leone & Leone, 2015). In addition, BCBM are HER2$^+$ phenotyped in 53% of the cases (Niwinska, et al., 2010). Breast cancer patients that have the HER2$^+$ phenotype generally show higher risks of brain metastasis and relatively low risks of bone metastasis, indicating that the genetic status of the tumor cells has an impact on the location of metastatic lesions (Vaz-Luis, et al., 2012). An important factor in this high prevalence rate of HER2$^+$ BCBM follows from the notion that systemic therapy is antibody-based and these molecules cannot easily reach the CNS. This possibly makes the brain a highly preferred site for metastasis (Leone & Leone, 2015). Other, more recent data suggest that the functioning of trastuzumab is downregulated in the microenvironment of the brain, and that this contributes to the high prevalence rate of HER2$^+$ BCBM (Kabraji, et al., 2018).

A very bad prognosis is associated with metastasis to the brain. BCBM patients have a median survival time of 3 to 6 months, and less than 15% of the BCBM patient population survives longer than 2 years. When diagnosed with BCBM, only whole brain radiotherapy can cause a relief to the neurological symptoms that are caused. This can give an improvement in the patients' QoL for their remaining lifetime (Ogawa, et al., 2008).

The current standard of care for BCBM is surgical resection, stereotactic radiosurgery, whole brain irradiation, or a combination of these methods, each with high risks of death or severe side effects. Treatment options depend on the localization, size and diffuse nature of the

tumor, as well as on the number of lesions (Bachelot, et al., 2013). Since these current treatment options for BCBM are very invasive and include high risks, a search is ongoing for molecular probes that can be used for non-invasive targeted imaging for diagnostics and subsequent targeted therapy.

2.3. Molecular nuclear imaging

In diagnostic molecular nuclear imaging, a molecular tracer with specificity for a certain marker of the disease is coupled to a diagnostic (β^+ or γ-emitting) radionuclide. This construct, referred to as the radiotracer, is then administered intravenously to patients in order to track down disease lesions. If the marker is present, the tracer will accumulate in the lesions, while the unbound fraction is cleared from the body over time. The radioactive signal that is emitted from this radiotracer, can be captured with appropriate machinery (Society of Nuclear Medicine and Molecular Imaging, sd).

Radiotracers for Positron Emission Tomography (PET) contain a radionuclide that emits a positron, which is the antiparticle of an electron and has an opposite charge. This is also known as β^+-decay. If a collision of a positron occurs with an electron from within the body, two photons are emitted in opposite directions. The emission of these photons can be measured and translated into three-dimensional images (National Institute of Biomedical Imaging and Bioengineering, 2016).

Another nuclear imaging technique is Single-Photon Emission Computed Tomography (SPECT) imaging. Radiotracers used in this imaging modality emit γ-rays that can be measured in three dimensions by gamma camera detectors (National Institute of Biomedical Imaging and Bioengineering, 2016).

In Computed Tomography (CT), patients are irradiated by narrow X-ray beams in order to visualize subsequent slices of the body in three dimensions. The detection happens at the opposite site of irradiation. The image obtained from this technique, allows the localization of organs and/or abnormalities throughout the body. This image can be combined with nuclear molecular images to generate an anatomical context for diagnostics. Today, most (pre-) clinical scanners allow SPECT or PET imaging with an integrated CT modality (National Institute of Biomedical Imaging and Bioengineering, sd).

The radiotracer's specific targeting can be achieved with natural antibodies, antibody derivatives or fragments, peptides, chemical compounds, and others.

2.4. Nanobodies

2.4.1. Origin of nanobodies

In mammals, 5 isotypes of antibodies are present in the blood: IgM (immunoglobulin-μ), IgA (immunoglobulin-α), IgG (immunoglobulin-γ), IgD (immunoglobulin-δ) and IgE (immunoglobulin-ε). Of these, the IgG types are the most abundant. The conventional structure of an IgG antibody (MW = 150 kDa) in mammals is heterotetrameric and consists of two identical Heavy polypeptide chains (H-chains, MW = 55 kDa each) and 2 identical Light polypeptide chains (L-chains, MW = 25 kDa each) (Muyldermans, 2013).

Heavy chains are made up of three constant domains (CH1, CH2 and CH3) and one variable domain (VH), and the built-up is as follows: (NH_2)-VH-CH1-CH2-CH3-(COOH). The N-terminal VH part makes contact with the antigen. In every light chain, a similar variable part is present (VL) to do the same, and only one constant part is attached at the C-terminal end of it (CL). Association of H- and L-chains occurs via disulfide bonds between CH1 and CL. Disulfide bonds also exist in between the constant parts of the two identical heavy chains. Together, the two H-chains and the two L-chains are combined to a full antibody, which is Y-shaped, as shown in **figure 2.6** (Muyldermans, 2013).
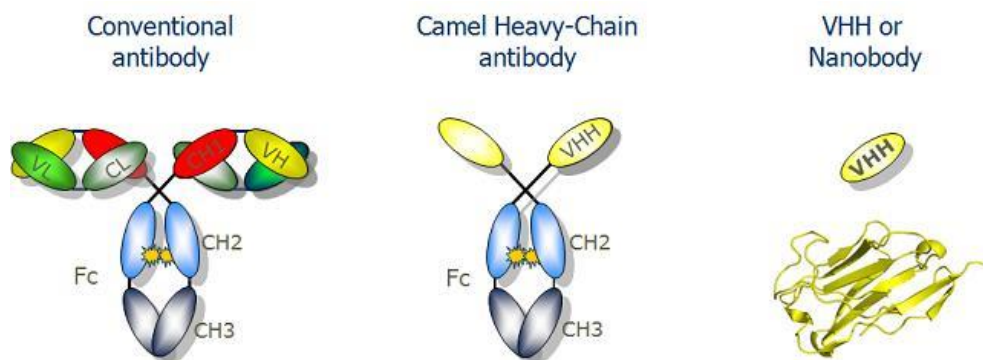

Figure 2.6: Schematic representation of conventional antibodies, heavy-chain only antibodies and nanobodies. *Figure retrieved from (Structural Biology Brussels, 2008).*

In every variable domain, four framework regions separate three peptide loops, referred to as the complementarity determining regions (CDRs). These CDRs make up the paratope surface, which interacts with the epitope. The smallest unit capable of binding antigens derived from a conventional antibody therefore consists of two variable domains, a combination of a VH and a VL molecule, with a combined paratope made up of 6 CDRs (Muyldermans, 2013).

In the blood of *Camelidae* (camels, dromedaries, llamas, alpacas and vicugnas), not only conventional IgG antibodies are found (IgG1 subisotype), but also Heavy Chain Antibodies (HCAbs, subisotypes IgG2 and IgG3), in which no L-chain is present and the CH1 domain is lacking from the H-chain (Hamers-Casterman, et al., 1993). These smaller antibodies have a MW of 90 kDa and the antigen binding part only consists of one domain, instead of two. Therefore, the HCAb contains the smallest autonomous antigen-binding fragment that still binds the antigen: the VHH domain, a genetic variant that has evolved from the family three VH gene, with only few amino acid differences. This VHH domain (15 kDa) is what is called a nanobody (**figure 2.6**) (Muyldermans, 2013) (Muyldermans, 2001).

The differences between a camelid VHH domain and a mammalian VH domain are limited. Four important amino acid substitutions (V37F/V37Y, G44E, L45R and W47G) are observed in the framework two region that separates CDR1 from CDR2. Since this framework region is involved in the formation of a heterodimer with a VL domain on non-HCAbs, these mutations are required to render this part of the antibody less hydrophobic, and therefore less prone to dimerization and aggregation. Another amino acid mutation in the first framework region (L11S) is frequently present in dromedary VHH sequences, but less often in alpacas. This mutation contributes to the solubility of the HCAb, since it is localized at the contact site between the CH1 and VH domains in a conventional antibody. Obviously, this contact is non-existing in a HCAb, since the CH1 is absent, and therefore a more hydrophilic amino acid is useful in obtaining a soluble protein domain (**figure 2.7**) (Muyldermans, 2001).

A third important difference between the VH and the VHH domain, are the lengths of the CDR regions, namely CDR1 and CDR3 are elongated in the VHH domain compared to the VH domain, generating an enlarged paratope surface. This is assumed to compensate for the lack of the three additional CDRs from the VL domain. CDR1 and CDR3 are often connected by a disulfide bond in VHHs, which is never observed in a VH domain. This extra structural constraint is thought to be present to lessen the entropy cost upon binding to the antigen (**figure 2.7**) (Muyldermans, 2001).
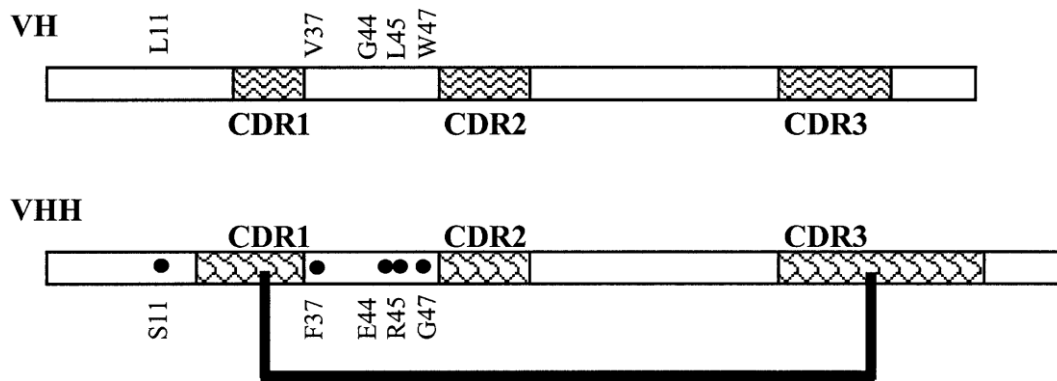
Figure 2.7: Representation of the differences between a VH and a VHH domain. *Main differences are an amino acid substitution in framework region one: L11S, four amino acid substitutions in framework two: V37F/V37Y, G44E, L45R and W47G, an extra disulfide bond between the CDR1 and CDR3 region, and a relatively elongated CDR1 and CDR3 region in the VHH protein compared to the VH domain. Figure retrieved from (Muyldermans, 2001).*

When a camelid is immunized or infected with a certain antigen, all three of the IgG subisotypes will be elicited (Muyldermans, 2013).

2.4.2. Characteristics of nanobodies

A high stability is observed with nanobodies, since they can be stored for several months at a temperature of 4°C in a simple phosphate or Tris buffer. Nanobodies can be resistant to low pH, proteases (Hussack, et al., 2011), denaturating chemicals (ureum or guanidinium chloride) and high temperature or pressure (Dumoulin, et al., 2002). The introduction of an extra disulfide bond can have a stabilizing effect, resulting in resistance to pepsin and chymotrypsin, which could allow oral administration (Hussack, et al., 2011).

The nanobody paratope can take on a tip-like conformation, allowing it to reach buried epitopes, because the CDR3 loop can be protrusive. This is a great advantage compared to antibodies, which are less capable to access catalytic sites of enzymes or other types of buried epitopes (De Genst, et al., 2006).

Nanobodies have low chances of being immunogenic when administered to humans, because of their small size, which allows a fast renal clearance from the blood circulation. Secondly, the stability and the solubility of nanobodies contribute to their low immunogenicity. A third important factor is the sequence resemblance between VHH and human VH fragments of family III, in the non-antigen-binding parts (Muyldermans, 2013). It was stated by the

company Ablynx that the occurrence of antibodies against nanobodies in clinical trials remains very low (3 %) and that neither safety nor effectiveness of the administered nanobodies changes due to this presence (Snoeck, 2013).

Since nanobodies are not human-derived however, a humanization strategy has been developed by Vincke *et al*., in which the antigen-recognizing CDR3 loop of the nanobody is grafted onto a humanized nanobody scaffold (Vincke, et al., 2009). This humanized nanobody shows no loss of targeting potential and is promising in further lowering the risk of immunogenicity when administered in humans (Vaneycken, et al., 2010).

2.4.3. Production and selection of nanobodies

Nanobodies can be produced in a relatively quick, cheap and straightforward way. After the immunization of a camelid and the collection of a blood sample, B lymphocytes can be isolated and the matured VHH genes of ± 360 base pairs (a nanobody is encoded by a single gene) can be amplified in a Polymerase chain reaction (PCR), all at once. The cloning of these VHH amplicons generates a VHH library of $10^6 - 10^8$ fragments which can be screened through different display methods, such as phage display, yeast display, bacterial display, ribosome display and others. The antigen binders can be selected through several rounds of panning and the selected VHH gene can afterwards be cloned into a bacterial expression vector with a secretion signal, leading to soluble nanobodies secreted into the periplasm. These nanobody constructs are often cloned with a C-terminal His-tag, allowing easy purification on nickel columns. Bacterial production of nanobodies normally is highly effective, as the production of several milligrams of the VHH construct per liter of bacterial culture is no exception (Muyldermans, 2013) (Steeland, et al., 2016).

A major difficulty in the use of antibody fragments is being circumvented when working with VHHs, because nanobodies only need one (matured) domain to recognize the antigen, while antibody derived antigen binding fragments need two domains that have undergone maturation together (as a VH and VL pair). It is however not possible to amplify VH and VL as a combination due to a different genomic localization of the two parts. This makes that both domains are amplified separately, and the advantage of the matured combination is lost. Two libraries result from this: one containing 10^6 VL parts and another containing 10^6 VH parts, leading to 10^{12} possible combinations. This scramble is never the case when working

with nanobodies, since they are encoded by a single gene. Therefore, the selection for good affinity binders is less labor intensive (Muyldermans, 2013).

2.4.4. Radiolabeling of nanobodies

Nanobodies can be radiolabeled in various ways. Random labeling occurs via reactive chemical groups that are naturally present in the VHH sequence. These are mainly amine groups on lysine residues. Chelators such as diethylenetriaminepentaacetic acid (DTPA) can for example be coupled via these groups, and be used to chelate radioactive elements, such as Indium-111 (^{111}In) for diagnostic purposes and Luthetium-177 (^{177}Lu) for therapeutic purposes (Liu & Edwards, 2001) (Krasniqi, et al., 2017). Nanobodies can often be mutated in a way that these groups are located at the opposite site of the paratope (Muyldermans, 2013). A more site-specific labeling approach exists for ^{99m}Tc, a γ-emitter that can be complexed by the His-tag of a protein (Kluba & Mindt, 2013). Another site-specific labeling technique is obtained by mediation of the *Streptococcus aureus* sortase enzyme, which can specifically couple a probe with an LPXTG-tag to a protein with an N- or C-terminal tag consisting of a stretch of glycine residues. This reaction and the protocol have been described by Theile and co-workers (Theile, et al., 2013) (Massa, et al., 2016).

An important difference can be made between radiolabeled probes for imaging purposes and for therapeutic purposes, namely that in imaging the main objective is to gain optimal contrast between target and non-target tissue, independently of the absolute amount of delivered activity. All non-specific signals will undermine the imaging capacity. In case of therapeutics, the main goal is to obtain a high concentration of the radiopharmaceutical on the target site. Accumulation of the tracer in non-target sites will not take away the therapeutic effect. It will however have toxic side effects, and therefore limit the amount of activity that can be administered (Vaneycken, et al., 2011b) (D'Huyvetter, et al., 2014b).

2.4.4.1. Radiolabeled nanobodies for diagnostic purposes

In nuclear immuno-imaging, a radiolabeled tracer is administered to a patient, usually through an intravenous route. This tracer consists of a probe with specificity for a certain molecular (disease) characteristic coupled to a β^+ or γ-emitting radionuclide. The tracer will be distributed through the body and stick on sites where the targeted marker is expressed, while unbound tracer molecules are eliminated from the body. The presence of the radionuclide can then be monitored by PET or SPECT in combination with CT or magnetic resonance imaging

(MRI) to generate an anatomical map in order to localize the disease markers within the body (Vaneycken, et al., 2011b).

Since an alternative glucose metabolism is observed in cancer tissues, this feature is used to image cancerous sites throughout the body. The shift from oxidative phosphorylation to aerobic glycolysis coincides with an enhanced uptake of glucose. To localize this alteration in metabolism, [^{18}F] fluoro-2-deoxyglucose (^{18}F-FDG) can be injected in the bloodstream to visualize tissue regions with an enhanced glucose uptake, using PET (Shaw, 2006). This is a non-specific approach that targets metabolically active (cancer) cells. The same is not true for more specific tracers (often antibodies or nanobodies), which target membrane-expressed antigens that specifically appear in diseased tissue. In this way, a molecular specificity is created and phenotypic characterization of cancer lesions throughout the body can be obtained (Vaneycken, et al., 2011b).

The use of full antibodies as tracer entities shows some disadvantages, such as a long blood residence time and slow tissue penetration. This makes that images can only be made 2 to 4 days after tracer injection, in order to obtain sufficient tumor-to-background ratios. As a consequence, the radioactive substance is present in the body for a prolonged time, and long-lived radionuclides are required, which contribute to a high radiotoxicity. The amount of tracer uptake in the tumor will be relatively low and often high liver and other nonspecific uptake is observed as well. These disadvantages can be countered by using smaller antibody-derived molecules such as nanobodies as tracer elements, as schematically represented in **figure 2.8** (Steeland, et al., 2016) (Vaneycken, et al., 2011b) (De Vos, et al., 2013).

It is important to ensure that the (radio)labeled nanobody used for imaging purposes does not function as an agonist on its targeted protein or receptor. This could indeed have inverse effects on treatment or cause unwanted interactions with the receptor expressed in healthy tissues (Steeland, et al., 2016).

2.4.4.2. Radiolabeled nanobodies for therapeutic purposes

Molecular diagnostics can be combined with targeted radionuclide therapy (TRNT). A targeting vehicle for a specific malignant molecular marker can be coupled to a PET or SPECT radionuclide for imaging and in a later stage with an alpha or beta$^-$ particle emitting radionuclide for therapeutic purposes. If both radionuclides are the same element, the diagnostic and therapeutic step can be combined. This combination is referred to as 'theranostic', which is for example possible with iodine (^{124}I for PET/CT scans and ^{131}I for

therapeutic purposes) (Silberstein, 2012) or with Yttrium (^{86}Y and ^{90}Y) (Rösch, et al., 2017) . The combination of Gallium-68 (^{68}Ga) PET/CT imaging with Lutetium-177 (^{177}Lu) radiotherapy is also considered theranostic, since these modalities are 'theranostic twins'. This approach is being evaluated in the clinic in multiple cancer types with different targets (Scarpa, et al., 2016) (Werner, et al., 2015). The inclusion of a diagnostic step can be of use for the selection of patients eligible for the therapy, for estimation of an effective dose, for the prognosis of potential side effects of therapy and for treatment follow-up (D'Huyvetter, et al., 2014b).
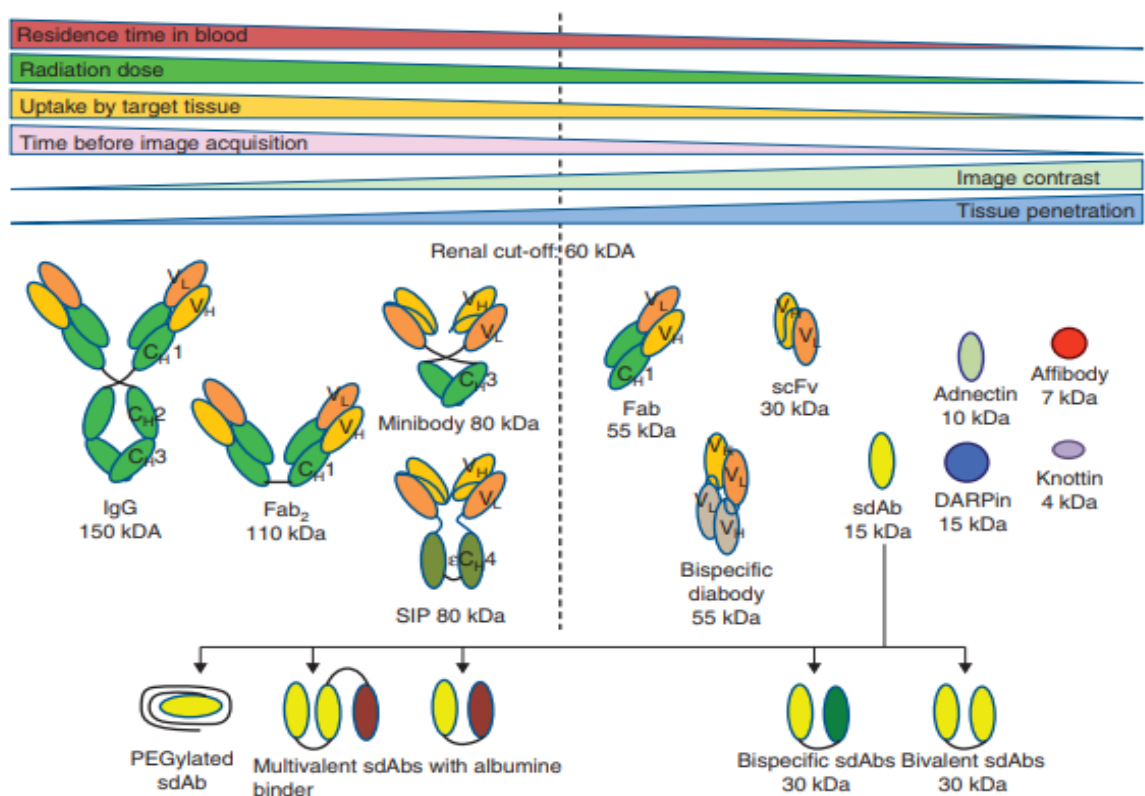
Figure 2.8: Comparison of antibodies and antibody fragments as agents to deliver radionuclides for imaging or therapy. *Figure retrieved from (De Vos, et al., 2013).*

Therapeutic potential of different radioisotopes is ranked based on their linear energy transfer (LET), which indicates the amount of energy that is delivered to the target measured over space. β^{-}-emitters that emit an electron such as ^{131}I and ^{90}Y show relatively low LET values (±

0.2 keV/μm). This corresponds to few and often indirect ionization damage to the DNA, over multiple cell diameters. As a result, targeted tissue might be repaired and survive the therapy and neighboring cells can possibly experience toxic side effects. Therefore, research in the field of TRNT nowadays focuses more on the use of α-emitters, such as ^{211}At and ^{213}Bi, emitting a Helium nucleus. This type of decay enables much higher LET values (50-230 keV/μm) leading to direct and irreparable damage to the DNA or to other vital cellular components, over a shorter range (D'Huyvetter, et al., 2014b) (Dekempeneer, et al., 2016).

Nanobodies as tracers for radio-immunotherapy have been developed preclinically. The comparison of radiation delivery capacity has been made between ^{177}Lu-trastuzumab and anti-HER2 ^{177}Lu-nanobody in HER2$^+$ tumor xenograft mice. Antibodies can deliver more radiation to the tumor in absolute values, which is a very important property in cancer treatment. On the contrary, the trastuzumab construct also delivers significantly more radiation to healthy tissues; a highly unwanted feature. This is not the case for radiolabeled nanobodies. On the contrary, nanobodies might evoke kidney damage, since the nanobodies are eliminated from the body via the renal route, as described in section 2.4.4.3 (D'Huyvetter, et al., 2014a).

HER2-specific nanobodies can also be useful tools in image-guided surgery, where a fluorophore is coupled to the nanobody in order to distinguish healthy from diseased tissue. This could be particularly useful in fragile organs such as the brain to ensure an exact tumor demarcation. Debie and coworkers have shown that labeled nanobodies are useful tools for image-guided surgery because they allow great speed and specificity in tumor labeling in addition to a low background signal. The manner of labelling, as well as the used fluorescent dye have an effect on kidney retention, liver accumulation, and tumor-to background ratios (Debie, et al., 2017).

Unlabeled nanobodies acting as neutralizing antagonist on their target receptor also show anti-tumor effects. The inhibition of cell proliferation signals in fast growing cells can decrease tumor development rates (McMurphy, et al., 2014).

2.4.4.3. Problems with the use of radiolabeled nanobodies *in vivo*

A disadvantage of the small size of nanobodies is the high accumulation in the kidneys due to fast blood clearance. In most cases, this renal uptake will be higher in absolute numbers compared to the tumor uptake (D'Huyvetter, et al., 2014b). For nanobodies labeled with radionuclides for imaging purposes, this is only problematic if a tumor is present in the

vicinity of the kidneys, as the radioactive amounts used to generate an image are very low. In case of therapeutic amounts of radiation, toxicity in the kidneys is an important stumbling block.

D'Huyvetter and co-workers have shown that the renal retention of VHHs is dependent on the nanobodies' C-terminal residues and their polarity. This has been observed in *in vivo* imaging studies using mice with HER2$^+$ xenograft tumors that were injected with 3 different ^{177}Lu - labeled nanobodies, each with a different C-terminal tag. His-tagged nanobodies show 88% more renal accumulation compared to untagged nanobodies and an even greater difference between the two (95%) if Gelofusin (a plasma expander) was co-administered (D'Huyvetter, et al., 2014a).

2.5. The blood brain barrier

2.5.1. Structure of the blood-brain barrier

Transport of cells, molecules and ions between the periphery and the brain is strictly regulated by 3 barriers: the BBB, the blood-cerebrospinal fluid barrier and the arachnoid barrier, all achieved by tight junctions in between cells (**figure 2.9**). These barriers exist because an exact homeostasis needs to be maintained in the brain to allow normal neuronal functioning. The BBB forms the most important and biggest anatomical and physiological interface in the CNS (Serlin, et al., 2015).

The BBB consists of brain capillary endothelial cells in between which tight junctions exist, the extracellular layer, and the basement membrane. The endothelial cells use low permeability in combination with explicit transport and pinocytosis systems, enzymes and receptors to create a very limited molecular passage between the blood and the brain. This low permeability is mainly achieved by the tight junctions in between the cells (Serlin, et al., 2015). The BBB is naturally impermeable for many compounds present in the blood, making the brain an immune-privileged site. Circulating antibodies rarely reach it; less than 0.1% of the full antibodies can enter the normal brain (Li, et al., 2016).

The BBB is permeable for O_2, CO_2, Xe, He, N_2 and some other gasses, such as many anesthetics. Water can also diffuse through the barrier, but dissolved molecules often need to cross the barrier via specific carrier systems. Passive diffusion of these solutes can occur to a limited extent, since the efficiency is dependent on net charge, molecular weight and lipid

fraction. The passage of other molecules is regulated by signals from both the blood and the brain side of the barrier (Serlin, et al., 2015).
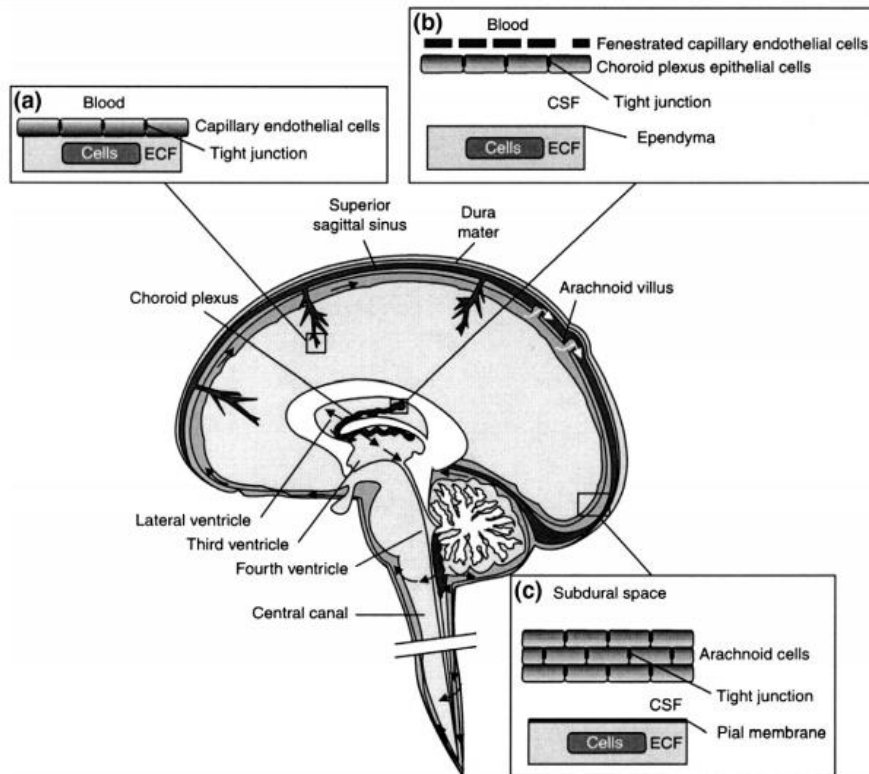
Figure 2.9: Three main barriers exist between the peripheral blood flow and the brain. *A) the BBB that consists of tight junctions between endothelial cells in the capillary of the brain. This separates the blood from the interstitial brain fluid.* ***B)*** *the barrier between the blood and the cerebrospinal fluid, consisting of tight junctions between the epithelial cells at the apical surface of the epithelium.* ***C)*** *arachnoid barrier, a multi-layered epithelium layer with tight junctions between the cells that separate the subdural/arachnoid zone from the cerebrospinal fluid. Abbreviations: CSF: cerebrospinal fluid, ECF: extracellular fluid. Figure retrieved from (Abbott, et al., 2010).*

2.5.2. The blood-brain- and blood-tumor barrier

PET studies on patients with glial cancers reveal a link between tumor grade and BBB permeability. An increased uptake of Methyl-L-^{11}C-Methionine as an administered probe for PET scans is associated with increased malignancy. Also, if a tumor grows out to be more malignant, angiogenesis (accompanied by vascular endothelial growth factor (VEGF)

expression) will augment (Ullrich, et al., 2009). In BCBM, together with increased vascularization in tumors, increased permeability of the BBB is seen, because greater uptake of ^{14}C- paclitaxel and ^{14}C- doxorubicin is observed in intracranial tumors in mice. Due to local impairment of BBB functioning, the blood-tumor barrier (BTB) arises at highly malignant sites, which is less strict compared to the BBB and allows vascular leakage to some extent (Lockman, et al., 2010).

Lockman and colleagues showed that in case of brain metastasis, the BBB takes on a slightly more permeable form. In practice, a greater uptake of fluorescently labeled chemotherapeutics in the brain is observed in mice models with metastatic brain lesions compared to the healthy control group. This enhanced uptake remained rather low, being less than 15% of the uptake in systemic metastatic sites and in the great majority of the cases, no relevant concentrations were observed in the brain. Though enhanced permeability is observed, other techniques might be needed to enhance BBB crossing (Lockman, et al., 2010).

Percey and co-workers further investigated the permeability of the BBB in case of metastases in a BCBM mouse model, using MRI with the gadolinium-based MRI-contrast agent, gadopentetic acid (Gd). This *in vivo* study shows that not all brain metastasis can be detected with Gd-MRI due to impaired BBB permeability (Percy, et al., 2011). The integrity of the BBB is not constant in different parts of the brain tumor. In some (large) tumor lesions, functioning of the BBB might be impaired or absent. This is due to the high metabolic needs of cancer cells, which implies the need of intensive vascularization. In other, often smaller cancer sites in the brain, the BBB is mostly functional. The location of integer BBB sites might therefore change during cancer development, and not all lesion sites are surrounded by a non-functional BBB (Ogawa, et al., 2008).

2.5.3. Trespassing the blood-brain barrier in cerebral tumors

A first strategy to overcome the BBB is by intravenous administration of a mannitol solution. This hyperosmotic liquid causes the endothelial cells to expel water. As a consequence, the cells shrink and the junctions in between them become larger. An *in vivo* study in human brain cancer patients was carried out, administering to them ^{99m}Tc-labeled glucoheptonate after a 25% mannitol injection. The patients were submitted to SPECT scanning at several time points post-injection to determine tracer accumulation in the brain. The BBB is opened maximally for the first 40 min, but an increased permeability stays present up to 8 h post injection. The problem with this prolonged BBB disruption is that it lacks tumor specificity,

which makes other parts of the brain especially vulnerable to influx of all sorts of compounds, followed by water. This may cause swelling and neurotoxic effects (Siegal, et al., 2000).

Another possible way to disrupt the BBB is by stimulating receptors on the endothelial cells in the cerebral arteries that regulate the tight junctions. One of these receptors is the Bradykinin receptor, which is involved in the regulation of blood pressure via the angiotensin pathway. RMP-7 (Cereport) is an agonist of this bradykinin receptor and can lead to transient BBB opening. This was shown in preclinical experiments on mice that were administered Cereport and a high MW product. Delocalization was allowed, after which the mice were sacrificed, and the brains were fixed with an aldehyde mixture. Electron microscopy was used to see that indeed the high MW compound penetrates RMP-7-treated mice brains better (Sanovich, et al., 1995). Another potential way for therapeutics to cross the BBB at sites where metastases occur is through administration of tumor necrosis factor (TNF) or lymphotoxin, which specifically interacts with TNF receptor 1. Expression of this receptor is both in mice models and in humans associated with expression on endothelial cells at sites of metastasis. Maximal permeabilization effects were noted 6 h post administration (Connell, et al., 2013).

A third way to enhance BBB permeability is by eliminating multidrug efflux systems that are involved in the limited brain entry. Transporters of the ABC family, such as ABCB1, have proven to be responsible for this. Tariquidar and elacridar are molecules designed to inhibit these transporters (van Tellingen, et al., 2015).

A transformation of water-soluble molecules into more hydrophobic compounds has also proven valuable for trespassing the BBB. A popular strategy to locally and reversibly disturb the BBBs integrity is by an intravenous administration of microbubbles together with the therapeutic to be delivered. After this, focused ultrasound waves are applied to the tumor area, which make the microbubbles exert mechanical forces on the blood vessels from within. Thereby, the tight junctions are opened locally, and the therapeutic compound can pass through (Fan, et al., 2017) (Dasgupta, et al., 2016).

Alternative strategies in overcoming the BBB consist of (radio)surgery and direct intracranial injection of drugs into the brain or tumor area (van Tellingen, et al., 2015). Surgical removal of the brain tumor is often followed by radiation therapy to reduce chances of the tumor to re-emerge. External whole brain radiation therapy or stereotactic radiation can be exerted as therapy options on their own as well (Berghoff & Preusser, 2018) (Aizer & Lee, 2018).

2.6. Brain tumor targeting with nanobodies

2.6.1. HER2-specific nanobodies

In 2011, Ilse Vaneycken and colleagues identified a HER2-specific nanobody that scored well on *in vitro* affinity, selectivity and kinetic studies. The nanobody can effectively be labeled with ^{99m}Tc, a diagnostic isotope used in SPECT imaging studies. *In vivo* studies in mice show high tumor uptake, quick blood clearance and good tumor-to-background ratios as well as low liver uptake. The latter is an important criterion since accumulation in the liver is unwanted because breast cancers often metastasize to the liver. Based on these tests, one specific nanobody (2Rs15d) was chosen out of 42 binders as an *in vivo* tracer for cancers with HER2-overexpression (Vaneycken, et al., 2011a).

The same nanobody has been tested as a diagnostic tracer in a phase I clinical trial on 20 HER2$^+$ breast cancer patients, with either primary or secondary tumors, who were administered different doses of ^{68}Ga-2Rs15d. PET scans were used to visualize the distribution. It was shown that at 1 h post injection already 90 % of the radiotracer was eliminated from the blood and good tumor-to-background ratios were found, including at metastatic sites. A non-specific uptake was seen in the kidneys, in the intestines, in the liver and to a lesser extent in the central bone and the lungs. These results warranted further assessment in a phase II clinical trial, which is currently ongoing (Keyaerts, et al., 2016) (Vrije Universiteit Brussel, 2015).

An important observation during the phase I clinical trial was the accumulation of ^{68}Ga-2Rs15d in a lesion located in the brain (**figure 2.10**) (Unpublished data). Unfortunately, no biopsy of the lesion was performed to confirm its HER2 status.
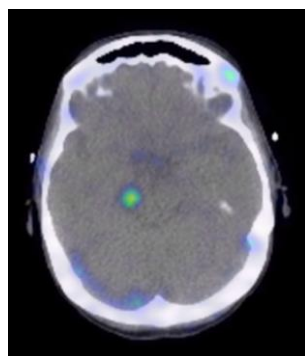

Figure 2.10: Uptake of ^{68}Ga-2Rs15d in the brain of a patient in a phase I clinical trial.

2.6.2. EGFR-specific nanobodies

Several EGFR-specific nanobodies have been developed for preclinical imaging purposes. Both Huang and Gainkam report about wt EGFR-targeting nanobodies labeled with [99mTc] for SPECT imaging (Huang, et al., 2008) (Gainkam, et al., 2008). A quick nanobody distribution over tumor tissue, liver and kidneys is observed by Gainkam and colleagues. At 24 h post injection (p.i.) of the tracers, still nearly 60% of the activity present at 1 h p.i. is observed in the cancerous lesions, which indicates a prolonged nanobody retention in the tumor (Gainkam, et al., 2008). The results of Huang and co-workers indicate that the nanobody can distinguish EGFR-overexpressing cells from cells with lower expression levels (Huang, et al., 2008). Therefore, nanobodies are convenient tracer molecules for RIT. Of course, liver and kidney toxicity are not to be neglected when envisaging these kinds of approaches.

These results indicate that anti-EGFR nanobodies are suitable as tumor-targeting tools for targeted imaging in mice bearing a peripheral xenograft. The studies however do not comprise glioblastoma lesions or any lesions within the head or brain, and therefore no information about the nanobodies' potential to trespass the BBB is provided. Another problem is created since in mice bearing a human $EGFR^+$ xenograft tumor, the tumor is the only site expressing human EGFR (hEGFR). This makes it an unrealistic model for human diseases, as many cells within the human body express this receptor and off-target binding will most probably be higher (Huang, et al., 2008) (Gainkam, et al., 2008).

A recombinant construct that encodes an anti-EGFR nanobody coupled to two affibodies recognizing HER2 has been tested in a preclinical *in vivo* experiment. Such a multi-receptor targeting molecule can be useful to enhance the selectivity for tumor cells in $HER2^+/EGFR^+$ cancers, a phenotype that is observed in many breast cancers. The construct was expressed by *E. coli* cells and linked to adriamycin, a chemotherapeutic. This fusion has great anti-cancer effects on tumors overexpressing both receptors, as it evokes a stronger reduction in tumor growth compared to other therapeutics, such as cetuximab or trastuzumab (Ding, et al., 2015).

Anti-EGFRvIII nanobodies have been reported by Omidfar and co-workers. These reports however do not make a convincing distinction between EGFRvIII binders and wt EGFR binders, as binding to the native form of EGFRvIII and not to native form of wt EGFR is never ascertained. No characterized lead compound is reported, and no further research data have been published since 2009 (Omidfar, et al., 2004) (Omidfar, et al., 2009).

2.6.3. Applications of nanobodies in cerebral tumors

It has been shown that monovalent nanobodies that are administered intravenously can trespass the BBB and reach the brain, though these levels remain very low. Brain penetration is better in situations where an inflammation of the brain is present, compared to biodistribution to healthy brain cells (Caljon, et al., 2012). Other reports state that nanobodies with a basic isoelectric point and a specificity for a cerebral target can spontaneously reach this target *in vivo* in mice when injected in a tail vein. Seconds after administration, the nanobody is present in vessels branching the injection vessel. This signal in the blood disappears after 20 minutes, in line with the short half-life of nanobodies in the blood. Shortly after administration a diffuse signal in the brain parenchyma is measured, which reduces to only target visualization after 30 min for extracellular targets and after 2 h for intracellular targets. Both these signals are still present after 4h, indicating long-term presence of nanobodies at the target site. If no target molecules in the brain are present, no brain retention of the nanobody is observed (Li, et al., 2016).

Nanobodies targeting insulin-like growth factor-binding protein 7 (IGFBP7), a marker that is specific for the GBM-associated vessels, can be labeled with a near-infrared dye and injected intravenously for optical imaging of GBM *in vivo*. The fluorescent signal is specifically present in tumor vessels and therefore these labeled nanobodies can visually delineate intracranial tumors (**figure 2.11**) (Iqbal, et al., 2010).
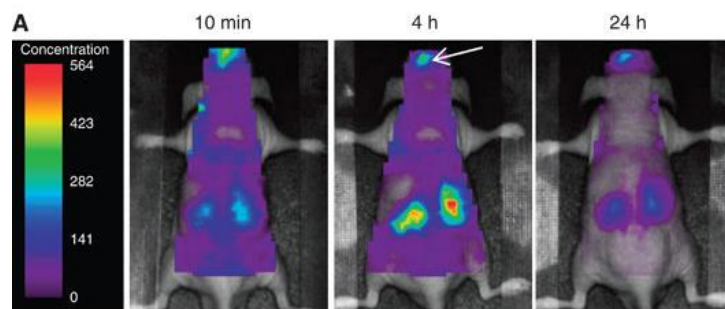
Figure 2.11: Results of in vivo optical imaging studies with near-infrared labeled anti-IGFBP7 nanobodies in mice bearing EGFTvIII$^+$ tumors. Representation of scans at different time points post injection of the nanobody tracer. Figure adapted from (Iqbal, et al., 2010).

Taken together the above studies, labeling of cerebral antigen-specific nanobodies for noninvasive imaging or therapeutic purposes might prove to be useful in future brain cancer diagnostics and treatment.

3. Aims

This master thesis has three main aims, covering three important points in the validation process of a nanobody to prove its value in a preclinical setting.

The first aim is to identify, generate and characterize a nanobody with a desired specificity. This nanobody will be retrieved from the lymphocytes of an antigen-challenged alpaca, and will therefore have the affinity of an *in vivo* matured antibody. The nanobody is aimed to target EGFRvIII, a mutant transmembrane receptor often observed in GBM tissue, and never in healthy tissue. This makes it an ideal target for (radio-)immune therapies and renders the generation of an exclusively EGFRvIII-binding nanobody extremely valuable, both from a scientific and an economic point of view.

A second aim is to validate nanobodies in a GBM context, more specifically in a model of brain tumors with EGFR overexpression in nude mice. To do this, human EGFR-expressing rat glioma cells will be intracranially implanted in nude mice, through a delicate operation procedure. When a brain tumor is established, an EGFR-specific nanobody will be radiolabeled and administered intravenously, and its brain tumor-targeting potential will be validated *in vivo*.

A third objective involves the comparison of the clinically approved HER2-targeting antibody trastuzumab with a nanobody targeting the same tumor-associated antigen in a preclinical model of breast cancer brain metastasis. This nanobody has already been developed at the In Vivo Cellular and Molecular Imaging (ICMI) and Cellular and Molecular Immunology (CMIM) laboratories and is currently in clinical trials for the diagnosis of breast cancer. Both will be compared in terms of tumor accumulation and tumor-to-background image contrast.

4. Materials and methods

4.1. Materials

4.1.1. Buffers and reagents

Table 4.1: Composition and source of the buffers and reagents used.

Buffer/medium/reagent	Composition	Source
0,2 M NH$_4$OAc	0.2 M NH$_4$OAc Add a tip of Chelex 100 sodium form to remove chelate metal ions Remove chelex with a Millex 32 mm syringe filter before use	Sigma Aldrich Sigma Aldrich Merck
1M TRIS-HCl	1 M TRIS pH adjusted to 8.0 with HCl	Sigma Aldrich Merck
Alkaline phosphatase (AP) blot buffer	100 mM Trizma base 50 mM MgCl$_2$.6H$_2$O 100 mM NaCl pH adjusted to 9.5 Filtered: 0.22 μm GyroDisc filter Stored at 4°C	Sigma Aldrich Duchefa Biochemie Fisher Scientific Orange Scientific
Alkaline phosphatase substrate	2 mg/ml 4-nitrophenyl phosphate disodium salt hexahydrate in AP blot buffer	Sigma Aldrich
Carbonate buffer	48 mM NaHCO$_3$ 2 mM Na$_2$CO$_3$ 150 mM NaCl pH adjusted to 8.5 Add a tip of Chelex 100 sodium form to remove chelate metal ions Remove chelex with a Millex 32 mm syringe filter before use	VWR International VWR International Sigma Aldrich Sigma Aldrich Merck
Hepes Buffered Saline	10 mM Hepes 150 mM NaCl 3.4 M EDTA disodium dehydrate 0.005 % (v/v) Tween20 pH adjusted to 7.4	Sigma Aldrich Fisher Scientific Duchefa Biochemie Sigma Aldrich
Ketamine/medetomidine	0.75 ml Ketamine 1 ml Medetor (1 mg/ml) 3.25 ml 0.9% (m/v) NaCl	Ecuphar Virbac Sigma Aldrich
Luciferin	30 % (m/v) Beetle luciferin, potassium salt in 0.9 % NaCl	Promega B. Braun

MACS buffer	2 % (v/v) FCS in PBS 1 mM EDTA	PAN-Biotech Duchefa biochemie
Phosphate buffered saline (PBS)	137 mM NaCl 2.7 mM KCl 10 mM Na_2HPO_4 1.8 mM KH_2PO_4	Fisher Scientific Merck Merck Merck
Tris-EDTA-sucrose (TES) buffer	20 % (v/v) 1 M TRIS-HCl (pH 8.0) 0.1 % (v/v) 0,5 M EDTA disodium dehydrate 0.5 M sucrose	 Duchefa Biochemie Duchefa Biochemie
TPA buffer	500 mM NaCl 23 mM Trizma base pH adjusted to 7.5	Fisher Scientific Sigma Aldrich

B. Braun, Diegem, Belgium; Duchefa Biochemie, Haarlem, The Netherlands; Ecuphar, Oostkamp, Belgium; Fischer Scientific, Loughborough, UK; Merck, Darmstadt, Germany; Orange Scientific, Braine l'Alleud, Belgium; PAN-biotech, Aidenbach, Germany; Promega, Madison, Wisconsin, USA; Sigma Aldrich, St. Louis, Missouri, USA; Virbac, Carros, France; VWR International, Radnor, Pennsylvania, USA.

Dilutions were prepared in Millli-Q® H_2O obtained from the Milli-Q® Integral Water Purification System from Merck, Darmstadt, Germany.

4.1.2. Recombinant proteins

Table 4.2: Overview of the recombinant proteins used during experiments.

Protein	Concentration	Source
hEGFR	2.6 mg/ml	U-Protein Express
hEGFRvIII	1.89 mg/ml	U-Protein Express

U-Protein Express, Utrecht, The Netherlands

Recombinant proteins were produced in and purified from transiently transfected mammalian cells, and therefore carry mammalian post-translational modifications.

4.1.3. Antibodies and nanobodies

Table 4.3: Overview of the antibodies and nanobodies used during experiments.

Antibody/nanobody	Concentration	Source
Anti-EGFR Nb7C12	1 mg/ml	Produced by the ICMI lab
Anti-EGFR-PE labeled IgG1 Ab	1 mg/ml	BD Biosciences
Anti-HER2 Nb2Rs15d	1 mg/ml	Produced by the ICMI lab
Anti-mouse IgG1-PE labeled IgG1 Ab	1 mg/ml	BD Biosciences

Anti-paraprotein (5T2) Nb R3b23 (negative control)	1 mg/ml	Produced by the ICMI lab
Anti-β-Lactamase-subunit 10 Nb BCII10 (negative control)	1 mg/ml	Produced by the ICMI lab
Goat-anti-mouse- IgG1 alkaline phosphatase coupled IgG1 Ab	1 mg/ml	Sigma Aldrich
Herceptin® (trastuzumab)	18.302 mg/ml	Hoffmann-La Roche
Anti-HER2 Nb2Rs15d coupled to IRDye800	20 mM	Produced by the ICMI lab
Anti-EGFRvIII IgG1 Ab L8A4	1 mg/ml	Absolute Antibody
Mouse-anti-hemagglutinin IgG1 Ab	1 mg/ml	Sigma Aldrich
Mouse anti-His IgG1 Ab	1 mg/ml	Thermo Fisher
Anti-mouse-HRP labeled IgG1 Ab	1 mg/ml	Sigma Aldrich

Absolute Antibody, Oxford, UK; BD Biosciences, Franklin Lakes, New Jersey, USA; Hoffmann-La Roche, Bazel, Switzerland; Sigma Aldrich, St. Louis, Missouri, USA; Thermo Scientific, Waltham, Massachusetts, USA.

References of the produced nanobodies: Nb7C12 (Gainkam, et al., 2008), Nb 2Rs15d (Vaneycken, et al., 2011a), Nb2Rs15d-IRDye800 (Debie, et al., 2017), NbR3b23 (Lemaire, et al., 2013), NbBCII10 (Conrath, et al., 2001).

4.1.4. Cells

Table 4.4: Overview of the bacterial cells used during experiments.

Cells	Genotype	Source
E. coli TG1	K12, supE, thi-1 *Δ(lac-proAB), Δ(mcrB-hsdSM)5*, $(r_K^- m_K^-)$	Sigma Aldrich
E. coli WK6	K12, *Δ(lac-proAB)*, *galE*, StrA/F', *laclq*, lacZΔM15, *proAB*⁺	ATCC

ATCC, Manassas, Virginia, USA ; Sigma Aldrich, St. Louis, Missouri, USA.

Following mammalian cells were grown in T75 cell culture flasks (Greiner Bio One, Kremsmünster, Austria) at 37°C and 5 % CO_2 (**table 4.5**). Cells were split when they reached ± 85% confluence. To do so, the cells were washed with DPBS (Thermo Scientific, Waltham, Massachusetts, USA) and detached with TrypLE (Thermo Scientific, Waltham, Massachusetts, USA), after which the appropriate cell culture medium was added in a three-fold excess to neutralize the TrypLE solution.

Table 4.5: Overview of the mammalian cell lines used during experiments, and the medium in which they were grown. With 'supplemented' is meant 10% (v/v) Fetal Bovine Serum (FBS), 2 mM L-Glutamine, 1% (v/v) PenStrep, 1% (v/v) Non-essential amino acids and 1 mM sodium pyruvate, all from Thermo Scientific (Waltham, Massachusetts, USA). Abbreviations: FLuc: firefly luciferase, GFP: green fluorescent protein, hEGFR: human epidermal growth factor receptor, hEGFRvIII: human epidermal growth factor receptor variant III, HER2: human epidermal growth factor receptor 2.

Cell type	Properties	Growth medium	Source
Chinese Hamster ovary (CHO)	/	Supplemented RPMI	ATCC
hEGFR$^+$ F98 rat glioma	GFP$^+$ FLuc$^+$ hEGFR$^+$	Supplemented DMEM	ATCC
hEGFR$^+$ F98 rat glioma	hEGFR$^+$	Supplemented DMEM	ATCC
hEGFRvIII$^+$ F98 rat glioma	GFP$^+$ FLuc$^+$ hEGFRvIII$^+$	Supplemented DMEM	ATCC
hEGFRvIII$^+$ F98 rat glioma	hEGFRvIII$^+$	Supplemented DMEM	ATCC
MDA-MB-231Br human breast cancer	HER2$^+$ GFP$^+$ FLuc$^+$	Supplemented DMEM	Kindly provided by Brunilde Gril (NIH/NCI)
SKOV3 human ovarian cancer	FLuc$^+$ HER2$^+$	Supplemented DMEM	ATCC

ATCC, Manassas, Virginia, USA.

Underlined proteins were transfected into the cell lines and non-underlined proteins are expressed by the cell line endogenously.

Dulbecco's Modified Eagle Medium (DMEM) and Roswell Park Memorial Institute (RPMI) 1640 medium were obtained from Thermo Scientific (Waltham, Massachusetts, USA).

All FLuc and GFP transductions were performed at the Laboratory for Molecular and Cellular Therapy (LMCT) lab at the Vrije Universiteit Brussel (VUB).

4.1.5. Radiometals

Table 4.6: overview of the radio metals used during experiments.

Radio metal	Source
$^{111}InCl_3$	Mallinckrodt Pharmaceuticals
$^{177}Lu\ Cl_3$	Isotopen Technologien Muenchen
$^{99m}TcO_4^-$	Commercially available $^{99}Mo/^{99m}Tc$ IBA generator, available at UZ Brussel, Nuclear Medicine Department

Isotopen Technologien Muenchen, Garching bei München, Germany; Mallinckrodt Pharmaceuticals, Surrey, UK.

4.2. Methods

4.2.1. Selection of EGFRvIII-specific nanobodies

4.2.1.1. *In vitro* nanobody selection from an immune library

Since EGFRvIII is a tumor-exclusive receptor variant that is never found in healthy tissue, it is an extremely interesting target for therapy. However, since the wild-type EGF receptor is expressed by various healthy tissue types, an immune protein is wanted that can discriminate the mutant from the wt receptor, and only binds to EGFRvIII.

To generate and select these binders, a camelid immune library was constructed. Immunization of an alpaca with both the EGFRvIII unique peptide stretch in a keyhole limpet hemocyanin hapten-carrier system and the complete extracellular part of the EGFRvIII protein was performed according to standard protocols (Vincke, et al., 2012). In short and as displayed in **figure 4.1**, the mRNA from the blood lymphocytes of this immunized animal was reverse transcribed into cDNA of which the VHH genes were amplified using nested polymerase chain reaction (PCR) with VHH-flanking primers. Using this genetic material, a library of pMECS vectors that contain the VHH genes with a hemagglutinin (HA) tag and a hexahistidin (His) tag in combination with the gene III phage coat protein, was readily prepared in *E. coli* TG1 cells. Phage production was induced in these bacteria using M13K07 helper phages (Thermo Scientific, Waltham, Massachusetts, USA) and the phages were isolated from the cells and stored at -80°C for later use. These steps had already been performed and the phage library was kindly provided by CMIM co-workers.

This immune VHH library was submitted to four rounds of panning, as described in the detailed protocol written by Vincke and co-workers (**figure 4.1**) (Vincke, et al., 2012). Because a VHH was desired that binds to the variant receptor and not to the wt EGFR, the protocol was slightly adjusted to obtain a competitive setting. Briefly, both the EGFRvIII (10 µg) and wt EGFR (100 µg) protein were coated on F96 maxisorp nunc-immuno plates (Thermo scientific, Waltham, Massachusetts, USA) in a 0.1 M NaHCO$_3$ (Merck, Darmstadt, Germany) coating buffer, pH 8.2. A negative selection was performed for binding to the wild-type protein and a positive selection for binding to EGFRvIII, in both orders.
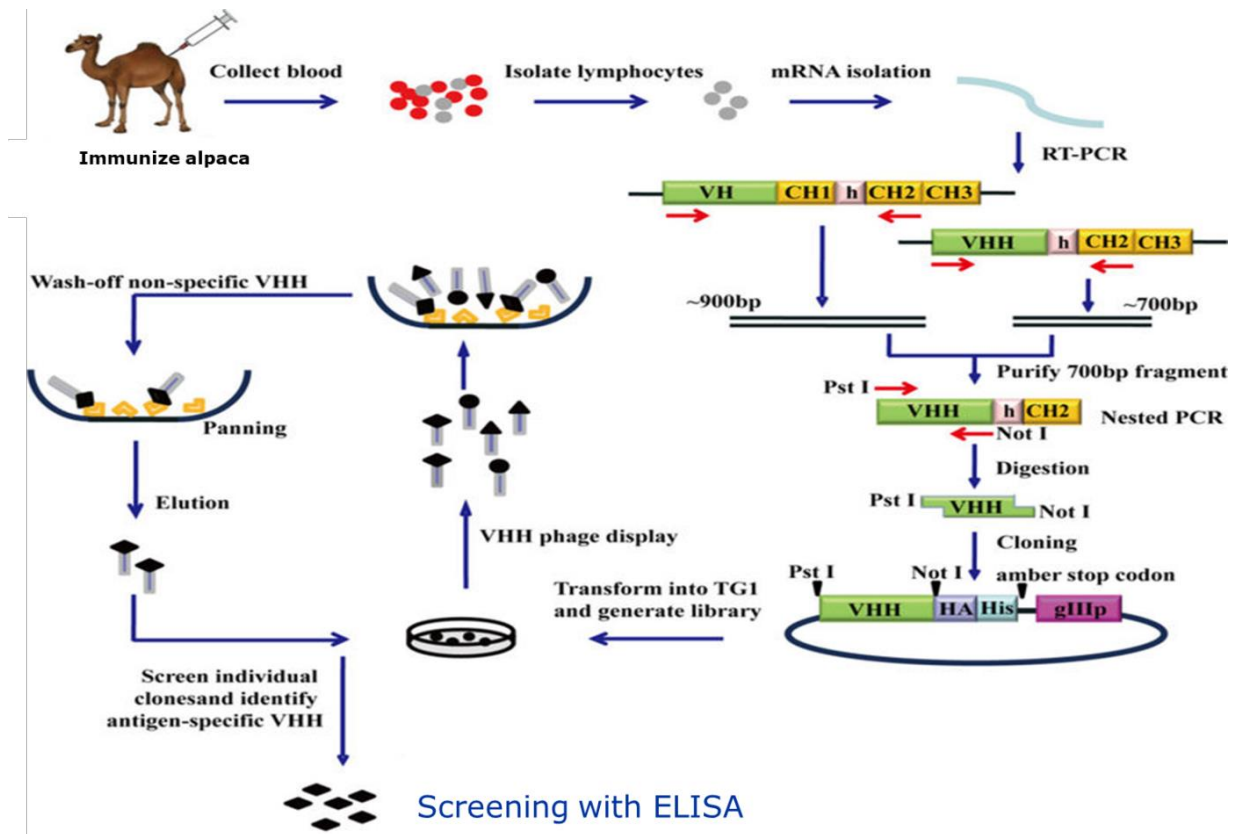
Figure 4.1: Schematic representation of the construction of a VHH phage display library and biopanning to generate antigen-specific VHHs. *First, a camelid is immunized with the appropriate antigen and 5-7 weeks later, peripheral blood, containing matured B-lymphocytes equipped with a B-cell receptor that has a high affinity for the antigen, is collected from the animal. The lymphocytes are isolated from the blood, after which the expressed mRNA is gathered and reverse transcribed into cDNA. From this cDNA pool, the VHH fragments are amplified in a nested PCR using VHH-flanking primers. These fragments are digested with the appropriate restriction enzymes (PstI, NotI or XbaI) and cloned into a pMECS vector, such that a construct of the following build-up is obtained: VHH fragment – Hemagglutinin (HA) tag – His-tag – Amber stop codon – GeneIII from the M13 filamentous phage – stop codon. These so-called phagemids are transformed into E. coli cells, and using a helper phage (M13KO7) the phages are produced. These phages each carry one VHH-geneIII protein on average on their surface, amongst other functional geneIII molecules, expressed from the M13KO7 helper phage. Phages are then selected via their ability to attach themselves to an antigen-coated well (biopanning), and the phages that are capable of this are used to re-infect E. coli bacteria. From this bacterium batch, phages can again be obtained in the same way, and these will be enriched for VHHs capable of recognizing the antigen. Multiple rounds of enrichment are usually needed to generate a binder with sufficient affinity. The selected VHHs can be expressed from the plasmid in E. coli cells and be tested for their ability to bind the antigen in an enzyme-linked immunosorbent assay (ELISA). Figure adapted from (Zhu, et al., 2014).*

The blocking buffers used during panning were Pierce Protein Free T2 Blocking Buffer (Thermo Scientific, Waltham, Massachusetts, USA) in round one, 0.1 % (m/v) casein (Merck, Darmstadt, Germany) in PBS in round two, 2% (m/v) milk powder (Nestlé, Vevey, Switserland) in PBS in round three and again Pierce Protein Free T2 Blocking Buffer (Thermo Scientific, Waltham, Massachusetts, USA) in round four. After discarding the unbound phages, more stringent washing conditions were applied as panning rounds progressed: in round 1, the plate was washed 10 times with PBS + 0.05 % (v/v) Tween20 (Sigma Aldrich, St. Louis, Missouri, USA), while this was done 20 times in round 2, 30 times in round 3 and 35 times in round 4.

For the generation of a novel phage stock after each panning rounds, exponentially growing *E. coli* TG1 cells (suppressor strain, su$^+$) were infected, but another part of the phages was used to infect exponentially growing *E. coli* WK6 cells (non-suppressor strain, su$^-$). This was done because su$^+$ cells do not recognize the amber stopcodon as a stop codon, but rather recognizes the UAG stopcodon as a glutamine due to a mutation in the corresponding tRNA molecule. Therefore, the nanobody is expressed in a fusion with geneIII, and since this protein is phage-originated, it is sticky by nature. This stickiness is an unwanted feature in screening experiments. All other steps in the panning experiment were executed as described.

The same published protocol describes the methods used for screening of the VHHs for binding to the antigen via indirect ELISA. The phage-infected cells were cultured, nanobody production was induced with 1 mM IPTG (Isopropyl β-D-1-thiogalactopyranoside, Fisher scientific, Loughborough, UK) and the periplasmic extract was obtained by freeze-thawing. These VHH-containing periplasmic extracts were used in an indirect ELISA to screen them for binding to both the wt EGF receptor and to EGFRvIII. 100 ng of both antigens was coated on F96 maxisorp nunc-immuno plates (Thermo scientific, Waltham, Massachusetts, USA) in a 0,1 M NaHCO$_3$ (Merck, Darmstadt, Germany) coating buffer, pH 8.2. Blocking buffers used during screening differed from the ones used during panning to avoid selection for binders that recognize the blocking agent. Pierce Protein Free T2 Blocking Buffer (Thermo Scientific, Waltham, Massachusetts, USA) was used when 0.1 % (m/v) casein (Merck, Darmstadt, Germany) in PBS or 2% (m/v) milk powder (Nestlé, Vevey, switserland) was used during panning and 0.1 % (m/v) casein (Merck, Darmstadt, Germany) for the rounds in which Pierce Protein Free T2 Blocking Buffer (Thermo Scientific, Waltham, Massachusetts, USA) was used during panning. The set-up of the ELISA is represented in **figure 4.2**.
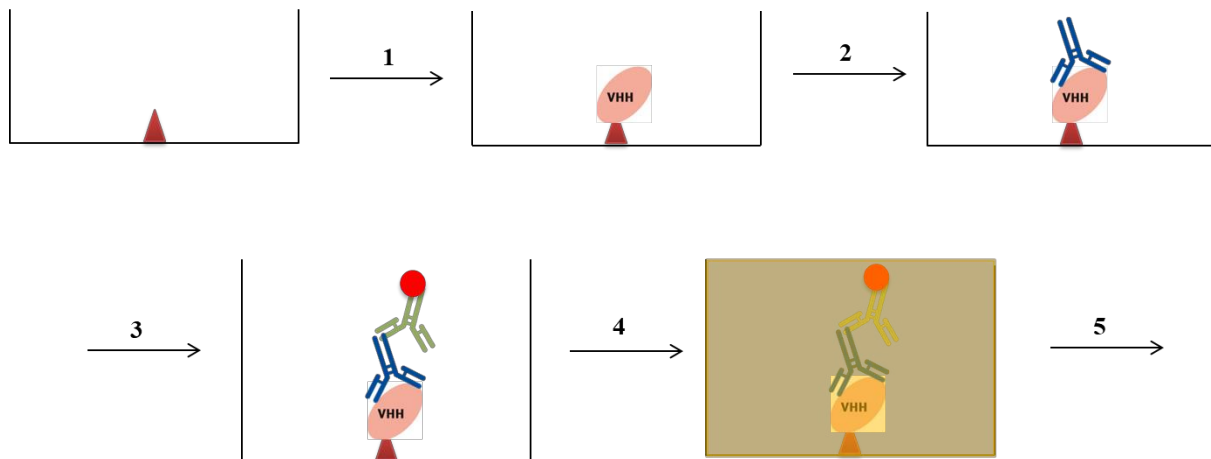
Figure 4.2: Schematic representation of sequential steps in the indirect ELISA. To start, 100 ng of each antigen was coated on F96 maxisorp plates and the plates were blocked. 1) to these plates, the periplasmic extract of one bacterial clone, containing the produced VHHs, was added. 2) to these wells, 50 ng of a mouse anti-HA primary antibody in PBS was added. 3) 50 ng of the secondary antibody, a goat anti-mouse IgG1 antibody coupled to alkaline phosphatase (AP) was added. 4) 200 μg of 4-nitrophenyl phosphate (the AP substrate) in AP blot buffer was added and a color reaction was observed in wells in which the nanobody had stuck to the antigen. 5) This color reaction could be quantified after 10 min of incubation in the dark by measuring the absorption at 405 nm with a VERSA max microplate reader (Molecular Devices, San Jose, California, USA), and thereby the concentration of transformed substrate. This was done at regular time points, up to 2 h after addition of the substrate. In between each step, a washing procedure was performed to discard all unbound proteins. Each generated VHH was tested on three wells: a well coated with EGFRvIII, another with wt EGFR and on an uncoated well with only the blocking agent.

Sequences of the VHHs deemed positive for binding selectively to EGFRvIII were obtained after executing a PCR, as described by Vincke, and sending these samples to the VIB Genetic Service Facility for nucleotide sequencing.

Production and purification of the selected nanobodies was executed according to the same protocol (Vincke, et al., 2012). In summary, a 2 liter bacterial culture of the selected clones was grown, induced for nanobody production and periplasmic extracts were prepared by imposing an osmotic shock to the cells with TES. The His-tagged nanobodies were purified from these bacterial extracts by the sequential steps of Immobilized Metal Affinity Chromatography (IMAC) and Size Exclusion Chromatography (SEC) on a Biorad NGC chromatography system (Hercules, California, USA) with a Superdex 75™ 10/300 GL column (GE Healthcare, Chicago, Illinois, USA).

To confirm the success of nanobody production and purification, a sodium dodecyl sulfate polyacrylamide gel electrophoresis (SDS-PAGE) and a Western Blot analysis were performed. To do so, 7 µg of the nanobody sample in 33 µl of 1.5 % (m/v) DTT reducing buffer (Bio-rad, Hercules, California, USA), diluted 10 times in Laemmli buffer (Bio-rad, Hercules, California, USA) or 7 µg of the nanobody in 33 µl pure Laemmli buffer (Bio-rad, Hercules, California, USA) was prepared, in order to create a reducing and a non-reducing environment for the nanobodies, respectively. Samples that were prepared in a reducing buffer were heated for 4 min at 95°C to obtain complete reduction (Thermomixer Comfort, Eppendorf, Hamburg, Germany). These samples were loaded onto an SDS-PAGE gel (Navex[TM] Wedgewell[TM] 16% Tris-Glycine gel from Thermo Fisher Scientific, Waltham, Massachusetts, USA) adjacent to a prestained protein size marker (PageRuler, Thermo Fisher Scientific, Waltham, Massachusetts, USA) and submerged in Tris/Glycine/SDS running buffer (Bio-rad, Hercules, California, USA). Two exact copies were run on the same gel – one for Coomassie staining and one for western blotting. The gel was placed in an XCell Sure Lock[TM] Mini-Cell Electrophoresis System box (Thermo Fisher Scientific, Waltham, Massachusetts, USA) and it was run for 45 min at 180 V, driven by a ZOOM® Dual Power Supply apparatus (Thermo Fisher Scientific, Waltham, Massachusetts, USA), after which the two identical halves were separated. One part of the gel was submerged in Coomassie blue stain (Bio-rad, Hercules, California, USA) for 45 min and destained with 40 % (v/v) methanol (Merck, Darmstadt, Germany)/10 % (v/v) acetic acid (Merck, Darmstadt, Germany).

The proteins in the part of the gel destined for Western Blotting were transferred to a nitrocellulose membrane (Bio-rad, Hercules, California, USA) in a 1 h transfer electrophoresis driven by the ZOOM® Dual Power Supply (Thermo Fisher Scientific, Waltham, Massachusetts, USA) at 800 mA in transfer buffer: 20 % (v/v) methanol (Merck, Darmstadt, Germany) in Tris/Glycine buffer (Bio-rad, Hercules, California, USA). After the transfer, the membrane was blocked for 2 h with a 2 % (m/v) milk powder (Nestlé, Vevey, Switserland) solution in PBS and the nanobodies were detected with 5 µg of a primary anti-His nanobody and 5 µg of a secondary HRP-coupled anti-mouse antibody in PBS. Antibody incubation required 1 h and a washing step with PBS/Tween20 0.1 % (v/v) (Sigma Aldrich, Saint Louis, Missouri, USA). Visualization of the bands was performed by incubating the membrane for 20 min in the HRP-substrate: 0.05 % (v/v) 4-Chloronaphtol (Thermo Fisher Scientific, Waltham, Massachusetts, USA) + 0.05 % (v/v) H_2O_2 (VWR International, Radnor, Pennsylvania, USA) in 16.7 % (v/v) methanol (Merck, Darmstadt, Germany) in TPA buffer.

4.2.1.2. Nanobody characterization by flow cytometry and surface plasmon resonance

Evaluation of nanobody binding to the cell-expressed target protein was performed by flow cytometry, both with the crude periplasmic extract containing the VHHs as with purified nanobodies.

To do so, hEGFRvIII$^+$ and hEGFR$^+$ F98 rat glioma cells and CHO cells (hEGFR$^-$, hEGFRvIII$^-$) were counted using a Neubauer chamber (Marienfeld, Lauda-Königshofen, Germany) after 0.4% Trypan blue (Sigma Aldrich, Saint Louis, Missouri, USA) staining and 2.5 x 10^5 cells were brought in fluorescence-activated cell sorting (FACS) tubes (5 ml polystyrene round bottom tubes, Corning Incorporated, Corning, New York, USA). These cells were incubated with 10 % (v/v) periplasmic extract or 2 µg purified nanobody in 1 ml MACS buffer. Detection of the nanobodies was performed by incubation with 1 µg of a primary antibody and 1 µg of a phycoerythrin (PE)-labeled secondary antibody in MACS buffer. In between each incubation step, the sequential steps of centrifuging the cells at 453 g for 5 min (5810 centrifuge, Eppendorf, Hamburg, Germany), washing them with 1 ml of MACS buffer and centrifuging again under the same conditions were performed. Detection occurred via the same principles as the indirect ELISA (**figure 4.2**), with the difference that the antigen is cell-expressed and the secondary antibody is not linked to an enzyme, but to a fluorescent label, meaning that no substrate needed to be added. In the control experiments in which no nanobodies were used, all antibodies were used in a concentration of 1 µg/1 ml of MACS buffer.

The presence of fluorescently labeled and unlabeled cell populations in each tube was detected by fluorescence measurements at 578 nm after excitation at 496 nm (BD FACS Canto^{TM} II Fow Cytometer, Becton Dickinson Biosciences, Franklin Lakes, New Jersey, USA). Data were analyzed with the FlowJo software (Treestar, Ashland, Oregon, USA).

The affinity of the generated nanobodies for the recombinant EGFRvIII protein was determined by surface plasmon resonance analysis on a Biacore T200 apparatus (GE Healthcare, Chicago, Illinois, USA). To do so, 10 µg/ml of the recombinant EGFRvIII protein in 10 mM sodium acetate (VWR International, Radnor, Pennsylvania, USA) at pH 5.5 was fixed on a 100 mM N-hydroxysuccinimide (GE Healthcare, Chicago, Illinois, USA) and 400 nM 1-ethyl-3-(3-dimethylaminopropyl) carbodiimide hydrochloride (GE Healthcare, Chicago, Illinois, USA)-activated CM5 sensor chip (Biacore, Uppsala, Sweden). Sites onto which no

antigen was coupled were blocked with 1 M NaOH (Merck, Darmstadt, Germany) at pH 8.5. Protein coupling was aimed to terminate at 1000 response units.

The purified nanobodies were brought over the chip at 25°C in a concentration range that varied from 125 nM to 0.48 nM, in a twofold dilution series in hepes buffered saline. Binding was allowed for 180 s and dissociation for 300 s, after which two regeneration cycles were performed with 0,05 M glycine (sigma Aldrich, Saint Louis, Missouri, USA)/1 M NaCl (Fisher Chemicals, Hampton, New Hampshire, USA) at pH 2.5. Data analysis and determination of association (k_a), dissociation (k_d) and equilibrium constants (K_D) were performed by curve fitting with the Biacore T200 2.0. Control Software (GE Healthcare, Chicago, Illinois, USA). The equilibrium constants (K_D) were calculated as the ratio of k_d/k_a.

4.2.2. *In vivo* brain tumor models

All animal experiments were reviewed and approved by the Ethical Committee for use of Laboratory Animals of the Vrije Universiteit Brussel.

4.2.2.1. Operation procedure for intracranial tumor implantation

To create an *in vivo* model of a brain tumor, cancer cells ($hEGFR^+$ $FLuc^+$ GFP^+ F98 rat glioma cells or $HER2^+$ $FLuc^+$ GFP^+ MDA-MB-231Br human breast cancer cells) were introduced in naive female athymic nude mice (nu/nu). To do so, the cells were counted with a Neubauer chamber (Marienfeld, Lauda-Königshofen, Germany) after 0.4% Trypan blue staining (Sigma Aldrich, Saint Louis, Missouri, USA) and brought to a concentration of 50×10^6 cells/ml in DMEM cell medium without supplements (Thermo Scientific, Waltham, Massachusetts, USA). Per mouse, 5 µl of the suspension, containing 250.000 cells, was used for intracranial inoculation.

Mice were anaesthetized in an induction box to which 5% vetflurane (1000 mg/g, Virbac, Carros, France) was supplied continuously (Isoflurane Vaporizer, Vet-tech Solutions, Congleton, UK). For the assessment of the anesthesia, the toe pinch reflex was tested, and the breathing frequency was monitored visually. Further anesthesia was achieved with lower concentration of vetflurane (1000 mg/g, Virbac, Carros, France), administered directly to the mice's mouth via a nose cone. Pain relief was achieved with a subcutaneous injection of 0.05 mg/kg bodyweight Vetergesic (Ceva Santé Animale, Barcelona, Spain).

The head was fixated in a stereotactic frame (Just for Mouse™ Stereotaxic Instrument, Stoelting Co., Wooddale, Illinois, USA, **Figure 4.3**) and Emla gel (25 mg/25 mg

lidocaine/prilocaine, AstraZeneca, Cambridge, UK) was applied to the top of the head, after which the area was disinfected with Isobetadine dermicum, 10% (Meda-Pharma, Brussels, Belgium).

The tumor-implantation technique was based on methods described by Assi and co-workers (Assi, et al., 2012). In short, a 1 cm incision was made on top of the head, revealing the skull. The microdrill (omnidrill 35, World Precision Instruments, Sarasota, Florida, USA) was positioned on top of the bregma, the junction point of sagittal and coronal skull sutures (**figure 4.4**), and was displaced 2 mm posteriorly and 2 mm laterally to the right, at which position a hole was drilled into the skull.
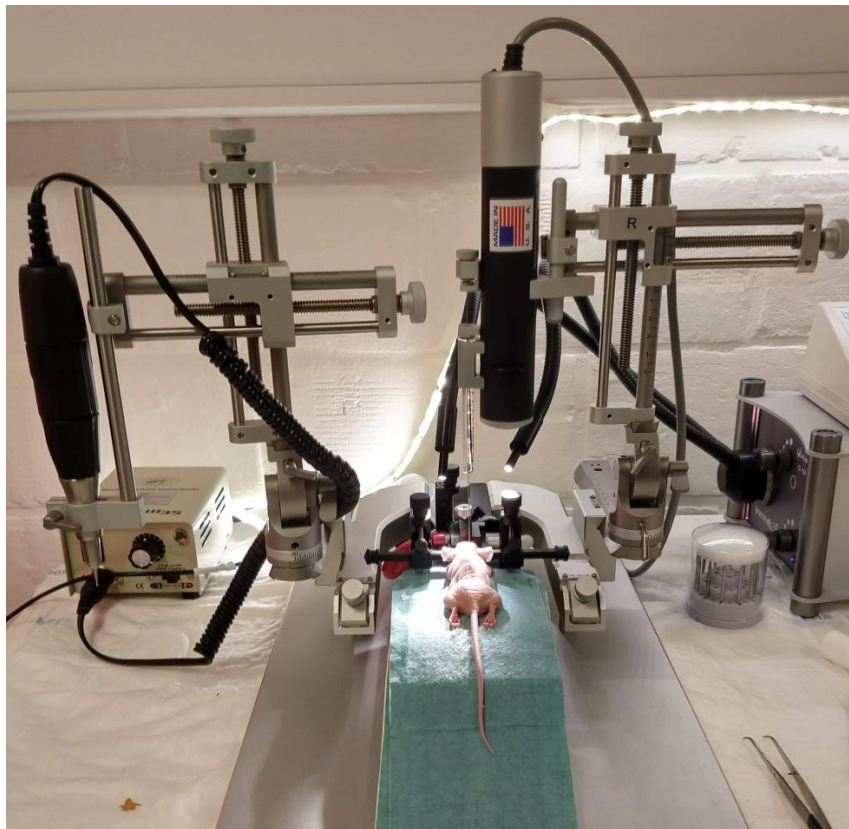

Figure 4.3: Stereotactic frame in which mice were fixated and anaesthetized during the intracranial operation procedure. *A microdrill (omnidrill 35, World Precision Instruments, Sarasota, Florida, USA) is provided on the left-hand side, with which a hole can be drilled into the skull. On the right-hand side, an automated injection system (Micro4TM Microsyringe pump controller, World Precision Instruments, Sarasota, Florida, USA) is implemented to inoculate tumor cells into the brain at a controlled flow rate.*
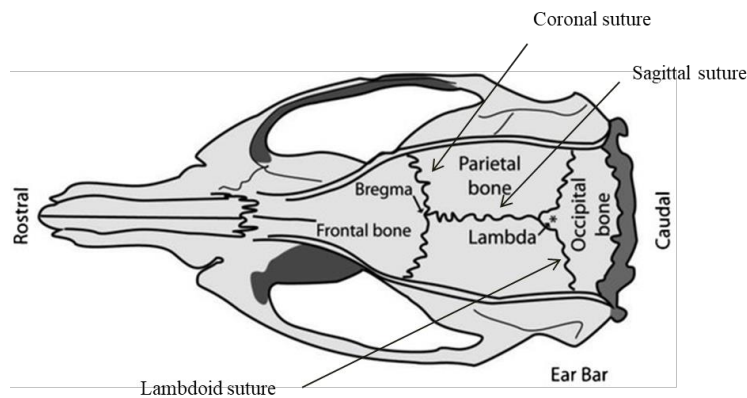
Figure 4.4: Schematic representation of the skull and its different bone subparts. The bregma and the lambda are junction points of the frontal and parietal bone (coronal suture) and the parietal and occipital bone (Lambdoid suture), respectively. Both are located on the sagittal suture. Figure adapted from (Assi, et al., 2012).

The needle tip of the 10 µl Hamilton syringe (Model 1701, Hamilton Co., Reno, Nevada, USA) was positioned above the microhole and slowly lowered 2.5 mm into the brain, brought back up 0.5 mm and used to inoculate 5 µl of the cell suspension in the brain over a period of 10 min, using the automatized syringe controller (Micro4^{TM} Microsyringe pump controller, World Precision Instruments, Sarasota, Florida, USA).

After inoculation, the microhole in the skull was sealed with bone wax (B. Braun, Diegem, Belgium), the skin was sutured (Ethicon*II, 5-0 Polyamid 6, Somerville, New Jersey, USA), and terramycine + polymixine B 30 mg/g + 10000 IU/g antibiotic cream (Pfizer, New York, New York, USA) was applied to the wound. During and up to 1h after surgery, placing a heating lamp in proximity of the mice prevented hypothermia.

4.2.2.2. Tumor growth follow-up with bioluminescent imaging

To visualize growth of FLuc^{+} tumor cells, bioluminescence imaging (BLI) was performed, as described by Badr (Badr, 2014). To do so, 150 mg/kg bodyweight of 30 % (m/v) Beetle luciferin potassium salt (Promega, Madison, Wisconsin, USA) in 0.9 % NaCl (B.Braun, Diegem, Belgium) was injected intraperitoneally (IP). Ten minutes after injection, mice were anesthetized with 5% vetflurane (1000 mg/g, Virbac, Carros, France) in an induction chamber and further anesthesia was maintained by inhalation of 3.5% vetflurane (1000 mg/g, Virbac, Carros, France) through a nose cone. *In vivo*, when cells take up the luciferin substrate, it is

oxidized into oxyluciferin by the luciferase enzyme, a reaction by which light is emitted. This light can be detected and quantified by a charge-coupled device (CCD) and localized on an anatomical level with the Biospace Photon Imager (Biospace lab, Nesles la Vallée, France). The captured signal over a predetermined area in the head region was quantified with the M3 vision software.

4.2.3. Radioactive labeling of immune proteins for *in vitro* and *in vivo* characterization

4.2.3.1. Labeling of immune proteins with ^{111}In or with [177]Lu

Coupling of an immune protein to DTPA

In order to radiolabel a nanobody or antibody with ^{111}In or ^{177}Lu for diagnostic purposes, it needs to be coupled to a DTPA bifunctional chelator (**figure 4.5**). To do so, the antibodies or nanobodies were buffer-exchanged to carbonate buffer (pH 8.5) using PD-10 columns (GE Healthcare, Chicago, Illinois, USA). Concentrations of the eluted fractions were determined with a Nanodrop 2000 device (Thermo Fisher, Waltham, Massachusetts, USA) and the most concentrated fractions were pooled. To this, a 20% molar excess of the p-SCN-Bn-CHX-A"-DTPA chelator (Macrocyclics, Plano, Texas, USA) was added and a nucleophilic addition of the amine groups on the lysine residue side chains to the isothiocyanate group of the chelator was allowed. This results in the conjugation of both molecules by the formation of a thiourea-bond. After 2 h of incubation the pH was lowered to 7.0 to stop the reaction.
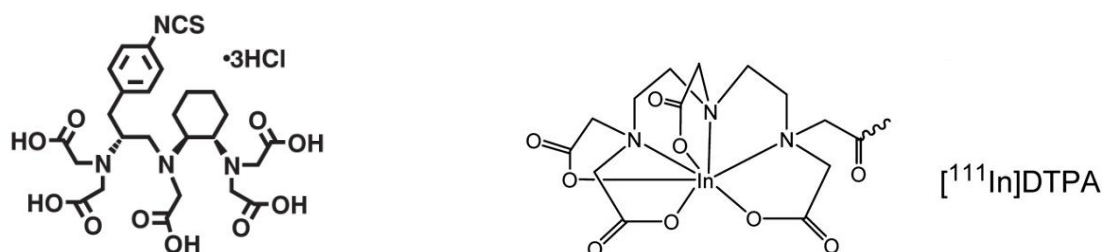

Figure 4.5: left: *[(R)-2-Amino-3-(4-isothiocyanatophenyl)propyl]-trans-(S,S)-cyclohexane-1,2-diamine-pentaacetic acid (p-SCN-Bn-CHX-A"-DTPA) bifunctional chelator used for the coupling of nanobodies and antibodies with ^{111}In and [177]Lu.* ***Right:*** *Structure of an ^{111}In-labeled DTPA chelator. Figures retrieved from (Macrocyclics, 2018) and (Jain, et al., 2007).*

This solution was concentrated using a vivaspin-2 (Sartorius, Göttingen, Germany) in a Sepatech Megafuge 1.0 centrifuge (Heraeus, Hanau, Germany), after which it was submitted to SEC on a Biorad NGC chromatography system (Hercules, California, USA with a GE Healthcare Superdex 75^{TM} 10/300 GL column). Fractions were collected when the absorption at 280 nm was over 100 mAU, pooled and the purified product was brought to a concentration of 1 mg/ml.

Radiolabeling of DTPA-conjugated nanobodies and antibodies with ^{111}In or ^{177}Lu

To radiolabel DTPA-conjugated immune proteins with ^{111}In or ^{177}Lu, they were brought together with 0.2 M NH$_4$OAc buffer (pH = 5.0) and ^{111}InCl$_3$ or ^{177}Lu in proportions shown in **table 4.7**. These methods have been described by (Massa, et al., 2014).

Table 4.7: Composition of reaction mixtures to generate ^{111}In- or ^{177}Lu- radiolabeled immune proteins in different experiments.

Experiment	V$_{buffer}$ (μl)	m$_{DTPA-protein}$ (μg)	V^{111}InCl$_3$ (μl)	Total activity (mCi)
In vitro binding assay α-HER2 Nb	250	10	250	0.23
In vivo imaging α-EGFR Nb	170	50	480	4.88
In vivo imaging α-HER2 Nb	170	50	480	4.58
In vivo imaging α-HER2 Nb - confirmation experiment	250	50	400	6.63
In vivo imaging α-HER2 Ab	220	50	230	5.11

Experiment	V$_{buffer}$ (μl)	m$_{DTPA-protein}$ (μg)	V^{177}Lu (μl)	Total activity (mCi)
In vitro binding assay α-EGFR Nb	200	50	1	0.83

The reaction mixture was put at 50°C for 30 min (Thermomixer Comfort, Eppendorf, Hamburg, Germany), after which the pH was adjusted to 4.0-5.0, if necessary. For antibodies, the sample was not heated but the reaction was allowed at room temperature.

To evaluate the radiochemical purity, an instant Thin Layer Chromatography (iTLC) quality control was performed by transferring a droplet of the reaction mixture to an iTLC-strip (iTLC SG, Pall, Belgium) and submerging one end of the strip in 0.1 M sodium citrate (Sigma Aldrich, Saint Louis, Missouri, USA), pH 5.0 to allow upward

migration of the free radionuclide. The radiochemical purity is calculated as the ratio of the activity of the non-migrated nano- or antibody and of the total measured activity in both parts of the strip. All activities were measured with a Dose Calibrator (Comecer, Joure, The Netherlands).

Further purification was performed on a small-scale NAP-5 chromatography column (Supradex™ G-25 DNA Grade, GE Healthcare, Chicago, Illinois, USA), with PBS/Tween 0.1 % (v/v) Tween20 (Sigma Aldrich, St. Louis, Missouri, USA) as the eluent. In a final step, the radiotracer was filtered through a 0.22 µm filter (Merck, Darmstadt, Germany) to remove aggregates.

4.2.3.2. Labeling of His-tagged nanobodies with ^{99m}Tc

Nanobodies carrying a C-terminal hexahistidine tag can be labeled with ^{99m}Tc according to a standard protocol (Xavier, et al., 2012).

A commercial kit was used (CRS kit for tricarbonyl, Center for Radiopharmaceutical Sciences, Villigen, Switserland), to which 150 mCi ^{99m}TcO$_4^-$ (Eluted from ^{99}Mo-based generator, IBA RadioPharma Solutions) was added and the formation of $[^{99m}Tc(H_2O)_3(CO)_3]^+$ was allowed for 20 min at 100°C and pH 11.0. Thereafter, the pH was lowered to 7.4 and 50 μg of His-tagged protein was added. Imidazole groups of the His-tag could then capture the $[^{99m}Tc(H_2O)_3(CO)_3]^+$ molecule during a 90 min reaction at 50°C (pH 7.4) (**figure 4.6**).

The purification and filtration of ^{99m}Tc-labeled nanobodies was similar to the procedure described for the radiolabeling of DTPA-coupled nanobodies with ^{111}In or ^{177}Lu. To determine the radiochemical purity, the iTLC strip was submerged in 100 % acetone (VWR International, Radnor, Pennsylvania, USA) instead of 0.1 M sodium citrate to allow migration of the free radio-isotope.
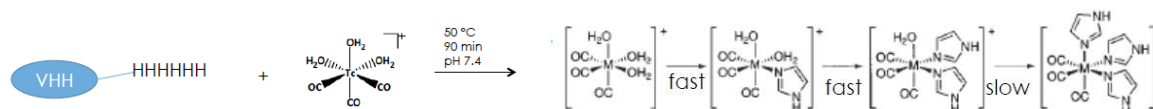

Figure 4.6: Representation of the conjugation chemistry of a $[99mTc(H_2O)_3(CO)_3]^+$ molecule with the imidazole groups of a His-tagged protein.

4.2.3.3. *In vitro* cell binding assay

To test whether a radiolabeled immune protein binds to cells expressing the targeted protein, *in vitro* cell binding assays were performed. To do so, the cells were plated out at a concentration of 2.5×10^5 cells per well on CELLSTAR 24 well plates (Greiner Bio One, Kremsmünster, Austria). These plates were incubated overnight at 37°C and 5 % CO_2. To these cells, the radiolabeled nanobody was added in different concentrations in supplemented growth medium. After 1 h of incubation at 4°C, the medium was removed, and its activity was counted in the γ-counter (CobraII^{TM} auto-gamma, Packard, Global Medical Instrumentation, Ramsey, New Jersey, USA). The cells were washed with cold PBS, and 0.5 ml of 1 M NaOH (Merck, Darmstadt, Germany) was added to lyse the cells. After 10 min, these cell lysates were brought to weighing counting tubes (Aptaca, Canelli, Italy) and the activity was counted in the γ-counter.

4.2.3.4. *In vivo* SPECT/CT imaging and *ex vivo* biodistribution

To visualize the *in vivo* distribution of the radiolabeled immune proteins in tumor-bearing animals, SPECT/CT scans (MiLabs VECTor, University Medical Centre Utrecht, the Netherlands) were performed after intravenous administration of the radiotracer. For each mouse ± 0.5 – 1 mCi (contained in 100 - 150 µl) of the radiolabeled immune protein was aliquoted in Microfine U-100 insulin syringes (Becton Dickinson, Franklin Lakes, New Jersey, USA) for IV injection.

Activities of both every full syringe and every syringe after injection were measured (Dose Calibrator, Comecer, Joure, The Netherlands). One syringe for activity quantification was emptied in a volumetric flask containing 500 ml of H_2O to prepare four 0.5 ml standards in weighing tubes (VWR chemicals, Radnor, Pennsylvania, USA).

Animal anesthesia was achieved by an intraperitoneal injection of 50 µl/mg body weight of the ketamine/medetomidine solution, 50 min after the intravenous injection of the radiolabeled construct. After 10 min, the mice were placed in the SPECT/CT scanner (MiLabs VECTor, University Medical Centre Utrecht, the Netherlands) and they underwent a short full-body SPECT scan of 5 min, combined with a 30 min brain-focused SPECT scan, followed by a whole-body CT scan. These retrieved images could be superposed to visualize the activity distribution *in vivo* in 3D with the AMIDE Medical Image Data Examiner software (**figure 4.7**).

To quantify the amount of radioactivity delivered to individual organs, mice were sacrificed after the scan and dissected to isolate the organs in weighing tubes (VWR chemicals, Radnor, Pennsylvania, USA). These, together with the four standards were put in a γ-counting device (CobraII^{TM} auto-gamma, Packard, Global Medical Instrumentation, Ramsey, New Jersey, USA) to measure the present activity. The radioactivity delivered to each organ, relative to the organ weight and normalized for radioactive decay, could then be calculated. For nanobody tracers, these steps are undertaken immediately after the SPECT/CT scan, while for antibody tracers, a SPECT/CT image was taken 1 h p.i. – after which the mice were awakened from the anesthesia with an intraperitoneal injection of 100 µl / 10 g body weight Antisedan® (Atipamezole hydrochloride, Zoetis, New Jersey, USA) - and 3 days p.i, after which mice were sacrificed and the *ex vivo* quantification was carried out (**figure 4.7**). This scheme was used because antibodies circulate much longer in blood and take much longer to distribute *in vivo* compared to nanobodies.
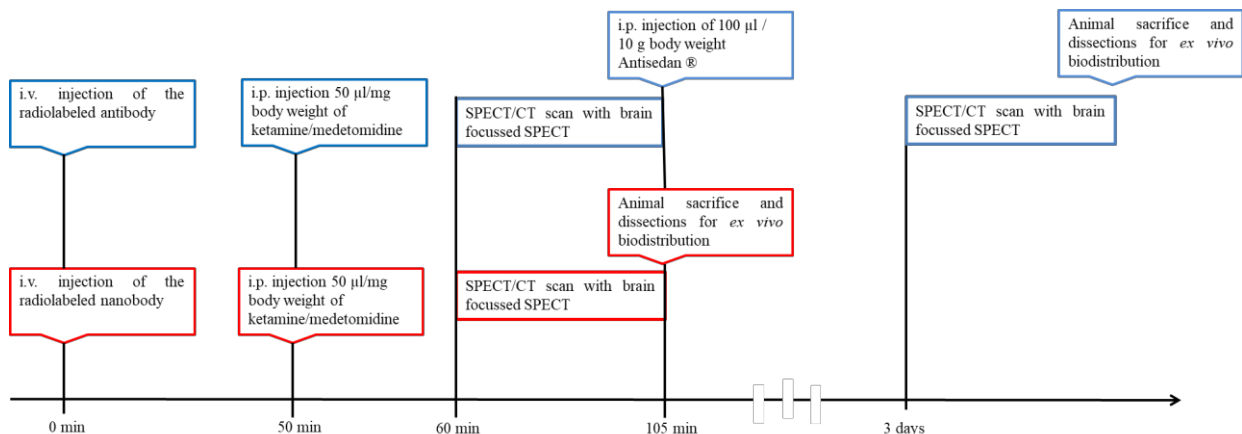

Figure 4.7: Time table for the acquisition of SPECT/CT images and ex vivo biodistribution for antibodies (upper, blue) and nanobodies (lower, red).

4.2.4. Different strategies to isolate tumor tissue from brain tissue

Brain tumor tissue is visually very hard to distinguish from healthy brain tissue. Therefore, strategies were developed to isolate these tissue types from one another.

4.2.4.1. Tumor localization based on GFP signal

Fluorescence imaging (FLI) with the Biospace Photon Imager (Biospace lab, Nesles la Vallée, France) could be used on isolated brains to localize GFP$^+$ tumor tissue and GFP$^-$ healthy tissue within the brain. Presence of GFP was measured at an excitation wavelength of 488 nm and an emission wavelength of 510 nm (filter cut off = 505-540 nm). Based on a full-brain image, this gave a rough idea about tumor localization.

4.2.4.2. Tumor dissections based on GFP signal

The same FLI-based method as described above could be used in an iterative way: the isolated brains were cut into smaller pieces, and FLI-positive parts were regarded as tumor parts and were isolated. Presence of GFP was measured at an excitation wavelength of 488 nm and an emission wavelength of 510 nm (filter cut off = 505-540 nm).

4.2.4.3. Real-time image-guided dissections

Optical imaging and nuclear imaging were combined when 2 nmol of a fluorescently labeled nanobody (anti-HER2 nanobody 2Rs15d labeled with the near infrared dye IRdye800, provided by the ICMI lab) was administered intravenously, 1 h post injection of the radiotracer, just prior to the initiation of the SPECT/CT scan. The presence of this dye could be visualized with fluorescence imaging equipment. Overlap in the presence of GFP-positive tumor cells and distribution of the IRDye800-labeled construct could be visualized with FLI (excitation wavelength = 774 nm, emission wavelength = 789 nm; filter cut off = 780–815 nm for IRDye800 and excitation wavelength = 488 nm, emission wavelength = 510 nm, filter cut off = 505-540 nm for GFP). During dissections, mice and their isolated brains were placed under the Fluobeam800 (Fluoptics, Grenoble, France), in order to visualize IRDye800-Nb accumulation in real-time throughout the body and the brain. Dissections of the brain were performed based on the real-time presence of fluorescent signal in order to attain a more accurate separation between tumor tissue and heathy brain tissue.

5. Results and Discussion

5.1. Selection of EGFRvIII-specific nanobodies

The expression of EGFRvIII is always tumor-exclusive and is frequently observed in GBM lesions in the brain, making this mutant receptor an attractive target for immune therapy and targeted imaging. The generation of an EGFRvIII-specific binder that does not recognize the wt EGF receptor was envisaged and attempted in this part of the master thesis project. This was done via the immunization of an alpaca with the targeted antigen, the generation of an immune VHH library and enrichment for specific binders via phage display in a competitive panning set-up and selection through ELISA.

A total of 956 clones were picked after four rounds of competitive panning and their periplasmic extracts were tested in an indirect ELISA. Of these, 59 revealed an EGFRvIII-specific binding activity - defined as VHHs of which the binding signal on EGFRvIII was two-fold higher than that of background and that of wt EGFR. In a confirmatory ELISA, 22 Nbs were selected that showed a ratio of binding to the coated EGFRvIII protein over binding to the uncoated well (background) of more than two (**figure 5.1**). This criterion was less strict to ensure that all possible EGFRvIII-binders were selected.

These 22 selected VHHs from ELISA were sequenced, and despite the great differences in ELISA signals, only two different sequences were retrieved (displayed in **figure 5.2**). This is possible, however, since the ELISA was performed with crude periplasmic extracts, and nanobody production rates might differ in between different clones. Remarkably, only one amino acid differs between the two obtained sequences, which lies in the CDR3 region. In 72.7 % (16/22) of the sequences, a glutamate is present at this position, and in all other cases (6/22), this residue is replaced by a lysine. This first sequence was observed from the second panning round on, and occurred more frequently in later panning rounds. The second sequence was only seen in round four. Two nanobodies (Nb3 and Nb10) were selected as representatives for each sequence (**figure 5.2**). These were readily expressed by *E. coli* WK6 cells (su⁻) since these cell types were infected during panning, and therefore the VHHs were not expressed in combination with the phage coat protein GeneIII, but did carry a His- and a HA-tag.
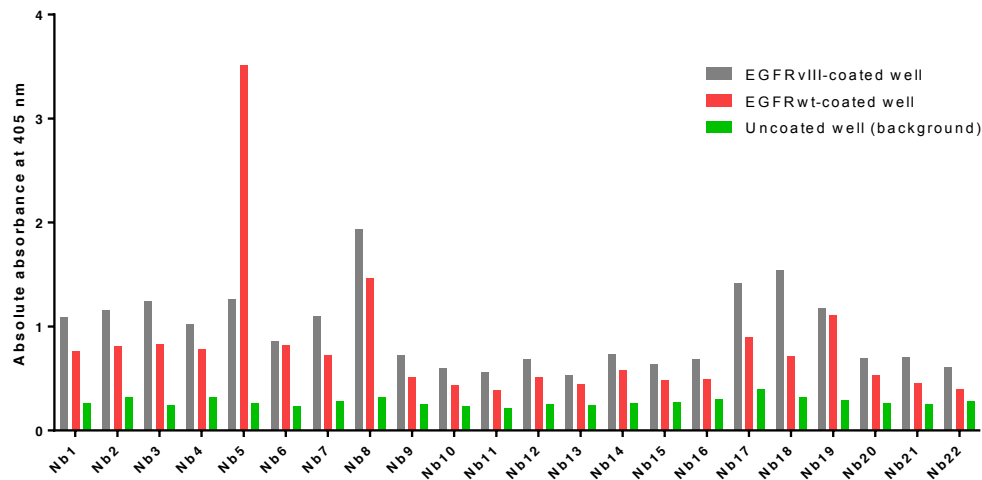
Figure 5.1: Results of the selected VHHs from the confirmatory ELISA experiment. *Absolute numbers of absorbance at 405 nm - as a measure of the concentration of converted AP substrate - obtained with the VERSA max microplate reader (Molecular Devices, San Jose, California, USA). Color legend: binding of the nanobodies to hEGFRvIII-coated wells is shown in grey, to wt hEGFR-coated wells in red and to uncoated wells (background) in green. All displayed ELISA results were obtained 2 h post addition of the AP substrate.*

Figure 5.2: Amino acid sequences of the two VHHs that were retrieved from the 22 clones that were deemed EGFRvIII-specific binders, based on ELISA results. *The four framework regions are written in blue, complementary determining region 1 (CDR1) is indicated in yellow, CDR2 in purple and CDR3 in green. The amino acid residue that differs between the two sequences is marked in red. Cysteine residues are underlined. Residue numbering is according to the IMGT numbering.*

In order to test the binding of the selected nanobodies to cell-expressed antigen, the periplasmic extracts of 10 ml cultures of the *E. coli* WK6 clones bearing the Nb3 and Nb10 pMECS plasmid were analyzed via flow cytometry on hEGFRvIII$^+$ F98 cells, hEGFR$^+$ F98 cells and on hEGFRvIII$^-$hEGFR$^-$ CHO cells. No binding to hEGFRvIII, nor to wt hEGFR was observed, while controls confirmed the correct expression of hEGFR and hEGFRvIII by the used cell types (**figure 5.3**).

A third control confirmed that the hEGFR-specific Nb7C12-His binds to both hEGFRvIII and wt hEGFR-expressing cells, as was expected. This nanobody has an affinity of 21.1 nM for wt hEGFR and 19.2 nM for hEGFRvIII, as determined by SPR during this master thesis. All fittings were performed with a one-to-one binding with drift and RI2 model. This control ensured that there is no problem with the replacement of antibodies by nanobodies in the protocol.

Since these flow cytometry results were obtained from the periplasmic extract of 10 ml bacterial cultures, obtained by freeze-thawing, many contaminants and possibly low nanobody concentrations were present in the used samples. Therefore, nanobody binding to the variant receptor was not yet to be excluded by these results, but rather nanobody production and purification was needed to re-asses the binding potential of the selected VHHs.

Nanobody production was therefore induced in 2 liter bacterial cultures, after which the periplasmic extract was obtained by an osmotic shock, leading to less contaminants. These periplasmic extracts were then submitted to IMAC. Production yields were 3.151 mg/l for Nb3 and 5.539 mg/l for Nb10, as determined by the Nanodrop 2000 apparatus (Thermo Fisher, Waltham, Massachusetts, USA), that measures absorbance at 280 nm, at which wavelength the aromatic residues in the polypeptide chain absorb[1].

---

[1] Nb3 has an estimated extinction coefficient at 280 nm (ε_{280}) of 29130 M^{-1}cm^{-1} and an estimated molecular weight of 16,009 kDa. Nb 10 is estimated to have the same extinction coefficient at 280 nm (ε_{280} = 29130 M^{-1}cm^{-1}) but a slightly different molecular weight: 16,007 kDa. These values were determined by the online ProtParam tool (ExPASy) and entered in the Nanodrop2000 software in order to determine the protein concentration as accurately as possible.
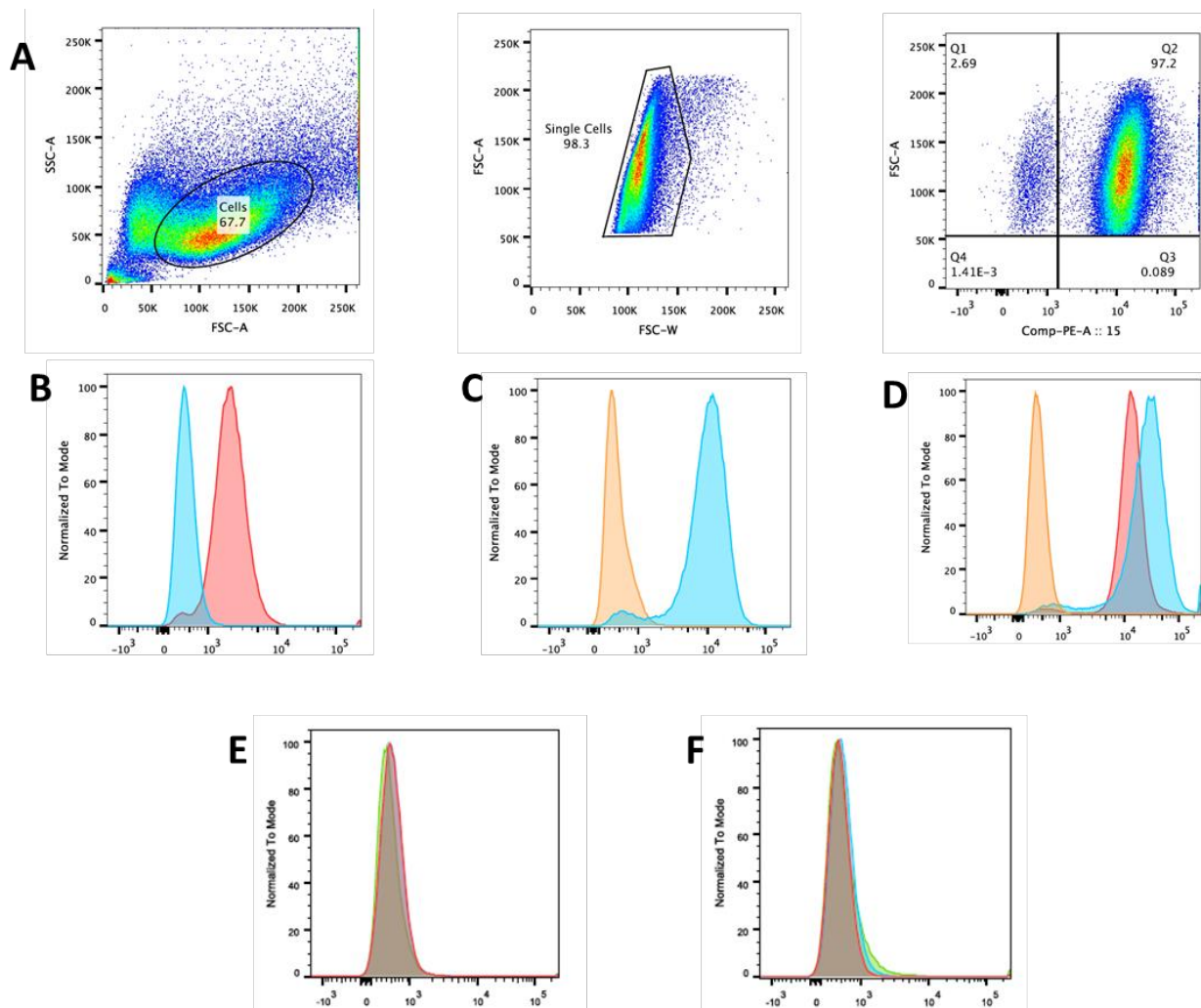
Figure 5.3: Results from the flow cytometry experiment, executed with the periplasmic extract of 10 ml of Nb3 and Nb10-expressing cultures. A) Gating strategy: single cells were selected after gating for the cells to avoid both doublets and debris. This single cell population is considered, and cell count is shown as a function of fluorescence. In this way, both a positive (fluorescently labeled, with a rightwards shift) and an unlabeled negative population at the left are viewed. B) Positive control: confirmation that F98 hEGFRvIII$^+$ cells express the variant receptor and that F98 wt hEGFR$^+$ cells don't, since the hEGFRvIII-specific antibody binds only to hEGFRvIII-expressing F98 cells (red) and not to wt hEGFR$^+$ F98 cells (blue). C) Positive control that F98 wt hEGFR$^+$ cells express the wt hEGFR receptor because an anti-EGFR Ab binds (blue) and does not bind to CHO cells (orange). D) Positive control to confirm that the anti-hEGFR Nb7C12 binds the hEGFR and hEGFRvIII receptor on F98 cells (blue and red respectively) and does not bind CHO cells (orange). E) Flow cytometry results of Nb3 binding to hEGFRvIII$^+$ F98 cells (red), wt hEGFR$^+$ F98 cells (blue) and CHO cells (green). No clear shift in cells with a fluorescent intensity is observed, indicating that the nanobody does not bind to either of the receptor types. F) Flow cytometry results of Nb10 binding to hEGFRvIII$^+$ F98 cells (red), wt hEGFR$^+$ F98 cells (blue) and CHO cells (green). No clear shift in cells with a fluorescent intensity is observed, indicating that the nanobody does not bind to either of the receptor types.

After IMAC, the purified nanobodies were freed from remaining contaminants and imidazole with SEC. The chromatogram of Nb3, showing the elution of the IMAC-purified nanobody from the SEC column is shown in **figure 5.4**. The Nb10 chromatogram was very similar (data not shown). It was concluded that both nanobodies were produced in a sufficiently large amount and could successfully be purified by IMAC. After SEC, the nanobodies were retrieved in PBS.

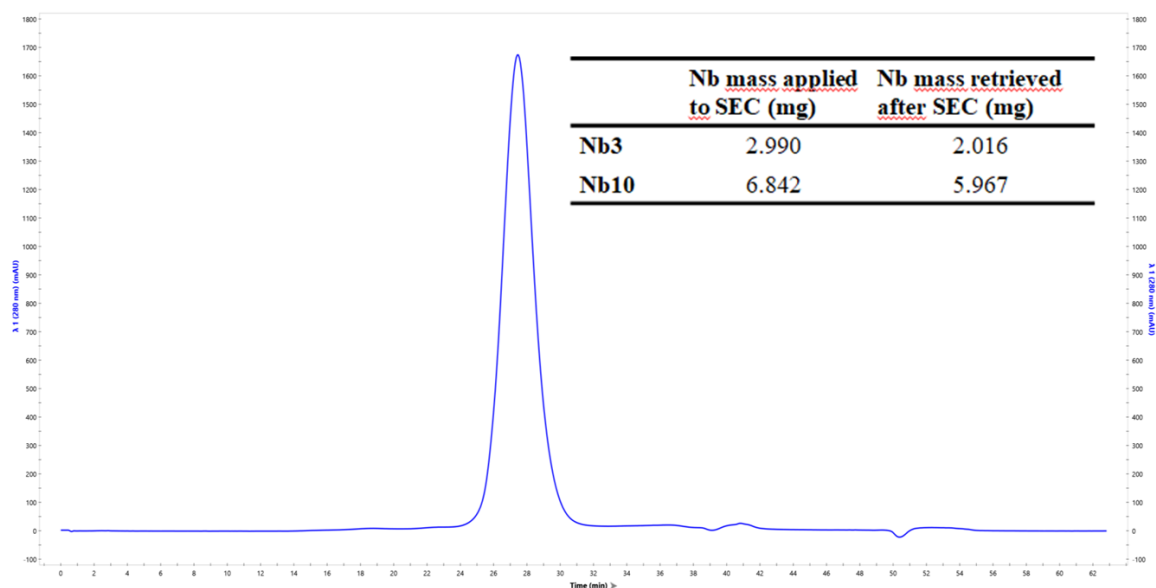|	Nb mass applied to SEC (mg)	Nb mass retrieved after SEC (mg)
Nb3	2.990	2.016
Nb10	6.842	5.967

Figure 5.4: Chromatogram of Nb3 purification with size exclusion chromatography after IMAC. The chromatogram shows the absorbance at 280 nm at the point where the sample leaves the column over time, and only one elution peak is observed. This indicates that little or no protein contaminants were present in the sample after IMAC. Masses of protein applied to SEC and nanobody masses retrieved after SEC are displayed on the figure. The little difference in mass before and after SEC indicates that the IMAC purification was successful and little contaminants remained after it.

In order to confirm the nanobodies' presence in the purified samples, an SDS-PAGE and a Western Blot were performed. The data obtained from these verification tests showed that nanobodies were present in both samples and that they contained the expected His-tag. However, a band of a higher molecular weight was observed in the reduced Nb3 sample, which was not seen in Nb10. This compound also contained a His-tag, and was therefore a nanobody derivate (**figure 5.5**).

To determine the cause of the extra band that was seen in the reducing conditions with Nb3 on the SDS-PAGE and the Western Blot analysis, the nanobodies were submitted to a confirmatory SDS-PAGE experiment in all possible conditions. Both nanobodies were tested in a freshly prepared reducing solution and in a non-reducing solution, and both after heating for 4 min at 95°C and without heating. It was observed that Nb3 shows split bands in the reducing solution, both in the heated and in the non-heated sample, while Nb10 does not show this behavior, nor does Nb3 in the non-reducing conditions (data not shown).
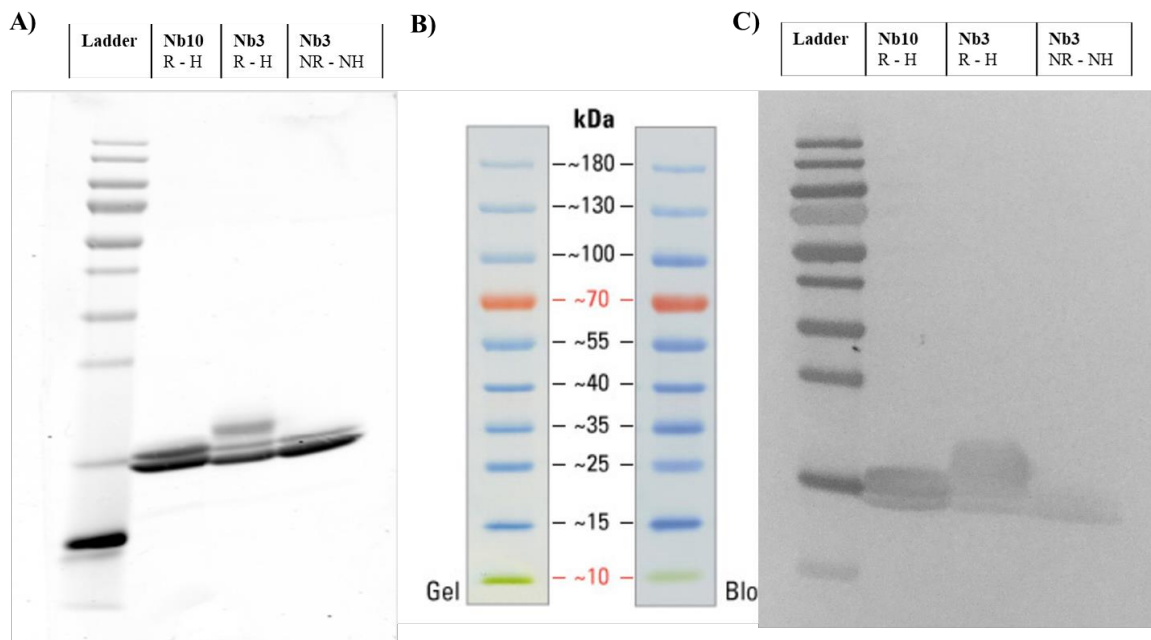

Figure 5.5: Results obtained from the SDS-PAGE gel (A) and the Western Blot (C). A) *Nb10 showed one band at 15 kDa in the reducing solution, and one above. This was assumed to be a reduced form of the nanobody, or the result of protein deamination. For Nb3, the same pattern was observed, but a product of a higher MW compared to the nanobody was also observed in the reducing conditions, while this was not present in the non-reducing conditions. Possibly, this is a second reduced form of the nanobody, that is not present in the reduced Nb10 sample. This indicates that potentially the reduction the nanobodies was incomplete. In the non-reduced Nb3 sample, two bands were observed, possibly due to spontaneous reduction or deamination.* ***B)*** *molecular mass ladder in kDa.* ***C)*** *results of the western blot: all molecules observed on the SDS-PAGE gel were positive for a His-tag, and therefore consisted of (or contained) the nanobody. Abbreviations: R: reducing conditions, NR: non-reducing conditions, H: heated, NH: non-heated.*

Multiple explanations for this behavior on the SDS-PAGE are possible. A first option in an effect of N-terminal protein deamination. This is possible when the N-terminal residue of the protein is a glutamine - as is the case for both nanobodies-, that loses its amine group to form cyclic pyro-glutamic acid (Dick Jr., et al., 2007). This causes the loss of an amine and of a positive charge, possibly leading to a different migration on the gel. Another possibility is an incomplete disulfide bridge reduction. A reduction of a disulfide bond would lead to a higher molecular weight band on the SDS-PAGE. Since in these nanobodies, two disulfide bridges are formed - one between the framework one and framework three region, and another between the framework two and CDR3 region – referred to as an interloop disulfide bridge in literature, **figure 2.7** (Muyldermans, 2001) (Saerens, et al., 2008) -, two reductions need to occur to obtain a fully reduced protein. Possibly, this reduction occurred not or only partial in Nb10, resulting in less bands of a higher MW. This can occur due to an inadequate reducing environment. Effects of charges on correct the formation of disulfide bonds (see below) also potentially influence the proteins' behavior on SDS-PAGE.

To confirm that no contaminants were present in the Nb3 sample and that the higher MW band was a consequence of the reducing conditions, the purified nanobody was again subjected to SEC, both in PBS and in the reducing buffer (100 µg nanobody in 100 µl Laemmli buffer with DTT, sample was heated to 95°c for 4 min). PBS was the running buffer through the column in both cases. The nanobody in PBS showed a single elution peak after about 19.7 min, as expected. This showed that no aggregates were formed in the purified sample and that no other components were present. However, the nanobody in the reducing buffer showed a different pattern on SEC. There was a strong peak after about 14.8 minutes, and a much weaker peak at the expected 19.7 minutes, indicating the formation of aggregates (**figure 5.6**). This would be possible if the reducing agent caused a reduction of the interloop disulfide bridge, and a separation between the reducing agent (DTT) and the protein happened on the column, leading again to oxidation. If this oxidation occurs intermolecularly instead of intramolecularly, a homodimerization of nanobodies takes place, and dimers would elute from the column first, as is seen on the SEC chromatogram. This is possible since the cysteine residues of the interloop disulfide bridge are surrounded by many negatively-charged residues (**figure 5.2**), creating repulsion in between the two residues. This might obstruct the re-oxidation of the intramolecular disulfide bridge.
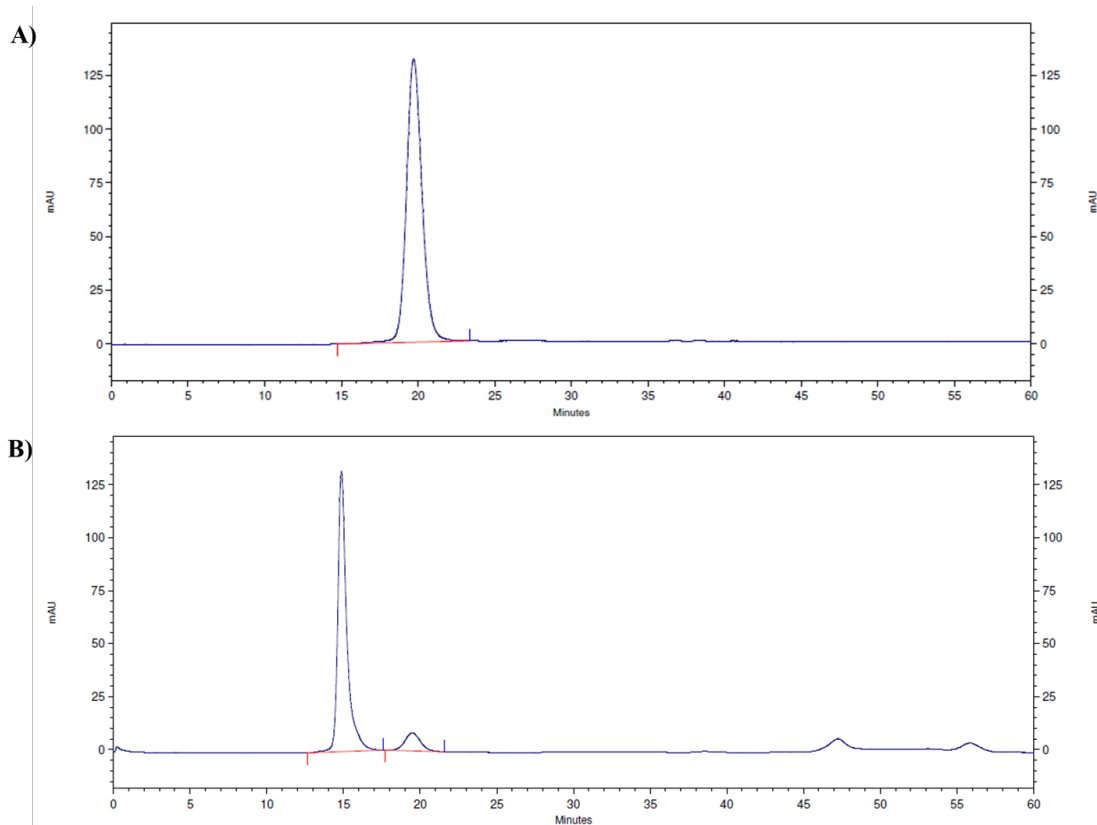
Figure 5.6: Chromatograms of Nb3 purification after elution from the HPLC-column. *Chromatogram A shows the elution of Nb3 in PBS and chromatogram B shows the elution of the same nanobody in the reducing buffer used in the SDS-PAGE and Western Blot analyses.*

A complex interplay of influences of side-chain charges on the formation of disulfide bridges in 3D, incomplete disulfide bridge reduction and deamination is thought to occur during SDS-PAGE and SEC. Defining exactly which influences play a role in this, falls outside the scope of this master's thesis, since the main goal was to identify EGFRvIII-specific binders. Altogether, the results show that the production and purification of the nanobodies was successful, and that the products obtained were indeed carrying the expected His-tag. This allowed to repeat flow cytometry with a purified product.

To explain the flow cytometry results obtained with the periplasmic extract, the experiment was repeated using purified proteins instead of crude periplasmic extract. It was observed in this repeated flow cytometry experiment that the purified nanobodies do not bind to the cell-expressed hEGFRvIII or hEGFR protein (data not shown). This means that either the nanobodies do not bind to the transmembrane form of the protein or they bind with a very low affinity.

61

To verify whether binding to the protein occurs or no binding at all is seen, affinities were determined via SPR. Hence, the protein was covalently coupled to the microchip, and coupling was terminated at 1576.3 response units. Different concentrations of the nanobodies were flown over covalently-coupled hEGFRvIII protein on a sensor chip. **Figure 5.7** shows that no binding of Nb3 to the recombinant protein was observed, while under the same conditions, binding of the anti-hEGFRvIII antibody showed binding with a steady state affinity of 3.6 nM (and no binding to the wt receptor). SPR results of Nb10 binding delivered the same pattern. No association-, dissociation or equilibrium constants could be fitted for either of the selected nanobodies.
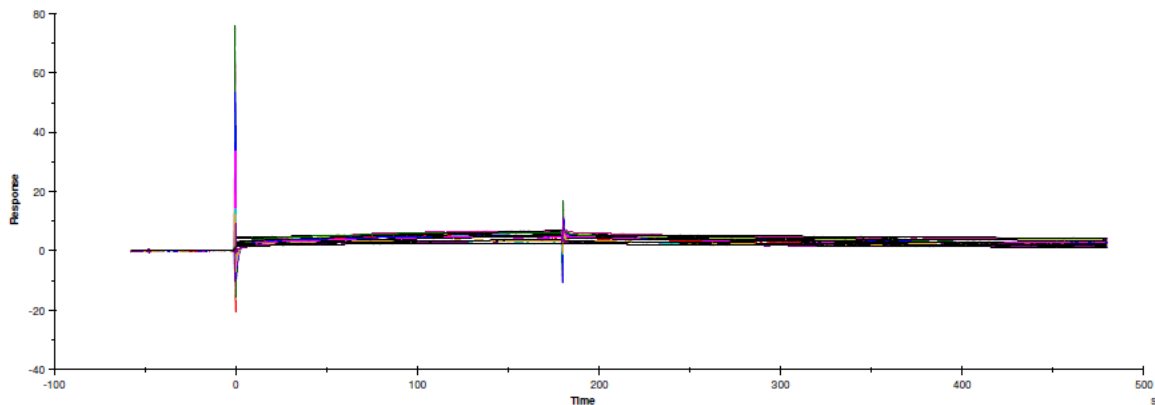

Figure 5.7: SPR results from Nb3 binding to recombinant hEGFRvIII. *No binding of the nanobody to the antigen is observed. It was concluded that the selected nanobodies are not capable of recognizing the biologically relevant antigen conformation.*

Since the VHH sequences of Nb3 and Nb10 were highly selected in the ELISA experiments - and blocking agents were altered during panning and screening rounds - chances are that the coating of the recombinant antigen on the ELISA affected the conformation of the protein. It is also possible that the immobilization of the antigen on plastic caused denaturation of the protein.

Because binding of the EGFRvIII-specific antibody was previously observed in a similar ELISA set-up, the option of an altered conformation was not considered before. Antibody molecules are however less sensitive to conformational differences (De Genst, et al., 2006),

and antibody binding might still succeed, despite conformational changes in the antigen or antigen denaturation upon passive immobilization. The same antigen-coating procedure is used for panning and for selection in ELISA. Because of that, binders might be enriched (panning) and selected (ELISA) that recognize an unnatural protein conformation or the denatured form of the antigen. This explains why no binders to the native antigen were retrieved.

An option to avoid this problem and to confirm this theory consists in a biopanning on hEGFRvIII^{+} cells or on recombinant EGFRvIII protein in solution. These approaches have been successfully developed, and could potentially be useful in the discovery of EGFRvIII-specific nanobodies. Panning on cells has several drawbacks, as many thousands of membrane-associated proteins are expressed on any cell surface, possibly in much larger amounts compared to the antigen. Also, phages naturally have high chances of adsorbing on cell membranes non-specifically (Jones, et al., 2016). Therefore, a biopanning and screening on recombinant protein in solution is considered a more feasible approach.

In parallel with this master thesis project, a first attempt has been made to perform a biopanning on biotinylated antigen in solution, followed by the conventional ELISA screening protocol. So far, these attempts have been without success. Possibly, the conformation of the targeted epitope is constitutively altered in the plastic-coated hEGFRvIII protein, and a protocol to do the screening on cell-expressed protein or protein in solution is needed as well. This is for example possible if the antigen is not coated via passive immobilization, but rather the biotinylated form of the antigen is applied to a streptavidin coated surface, as described by Verma and co-workers (Verma, et al., 2018). The clearly observed binding of the anti-EGFR Nb7C12 to the recombinant EGFR protein and anti-EGFRvIII Ab L8A1 to the recombinant EGFRvIII protein in SPR proves that the recombinant proteins are at least in part correctly folded, and can be used in such a circumstance.

A way around the drawbacks of a panning on cells, lies in the use of bacterial display. In an approach developed by Fleetwood and colleagues, the VHH library is expressed by *Staphylococcus carnosus* bacteria, and these are incubated with the fluorescently labeled antigen and a differently labeled reporter protein, that reports nanobody expression on the cell. Cells containing the sequence of a VHH that binds the antigen, will therefore be positive for both fluorophores and can be selected for via FACS and used in a next round (Fleetwood, et al., 2013). In another approach, described by Jens De Vos, a co-expression of GFP with the

target antigen on cells is used. The VHH library is expressed upon phages via standard phage display, and these phages are added to a mixture of the GFP-antigen-positive cells in an excess of antigen-GFP-negative cells. Cells that express the antigen can be isolated via FACS, based on the GFP signal, and the phages eluted from them can be taken to a next panning round (De Vos, 2014).

Because many unsuccessful attempts in the generation of an EGFRvIII-specific nanobody have been made, the possibility that the mutant-unique peptide stretch is not antigenic to alpacas needs to be considered. The existance of an EGFRvIII-specific antibody does not exclude this option, since classical antibodies target different epitopes compared to HCAbs (De Genst, et al., 2006), and are retrieved from other animals. The ELISA results however indicate that indeed the targeted epitope is antigenic, and that HCAbs are evoked specifically towards the variant receptor. These binders however do not recognize the epitope in its native form, but rather an unnatural conformation. Possibly, the immunized animal did not respond to this particular epitope in its native form, while it is antigenic. A novel immunization of another animal might therefore be warranted if further improvements in the biopanning and/or screening protocol remain unsuccessful.

5.2. *In vivo* brain tumor models

To validate the brain tumor-targeting potential of existing nanobodies in an *in vivo* model of brain cancer, mice were inoculated intracranially with cancer cells. Even with a very standardized operation procedure for the inoculations, a very heterogeneous tumor progression was observed in every group of inoculated mice. **Figure 5.8** shows the typical heterogeneous evolution in animal weight and tumor growth, with often occurring metastasis to the spinal cord. This heterogeneity was seen in both F98 hEGFR$^+$ tumor inoculated mice as in HER2$^+$ MDA-MB-231Br inoculated animals. A 100 % inoculation success rate was observed, since all inoculated animals developed a brain tumor.

The process of tumor development required an optimized time of 14 to 17 days in between the inoculation of the tumor cells and the imaging experiment. This time is needed to allow an adequate recovery of the brain and the BBB after inoculation, nesting of the cells and development of a full-fledged brain tumor. Since the used cell lines showed a very heterogeneous pattern of tumor development, the experimental planning was often jeopardized.
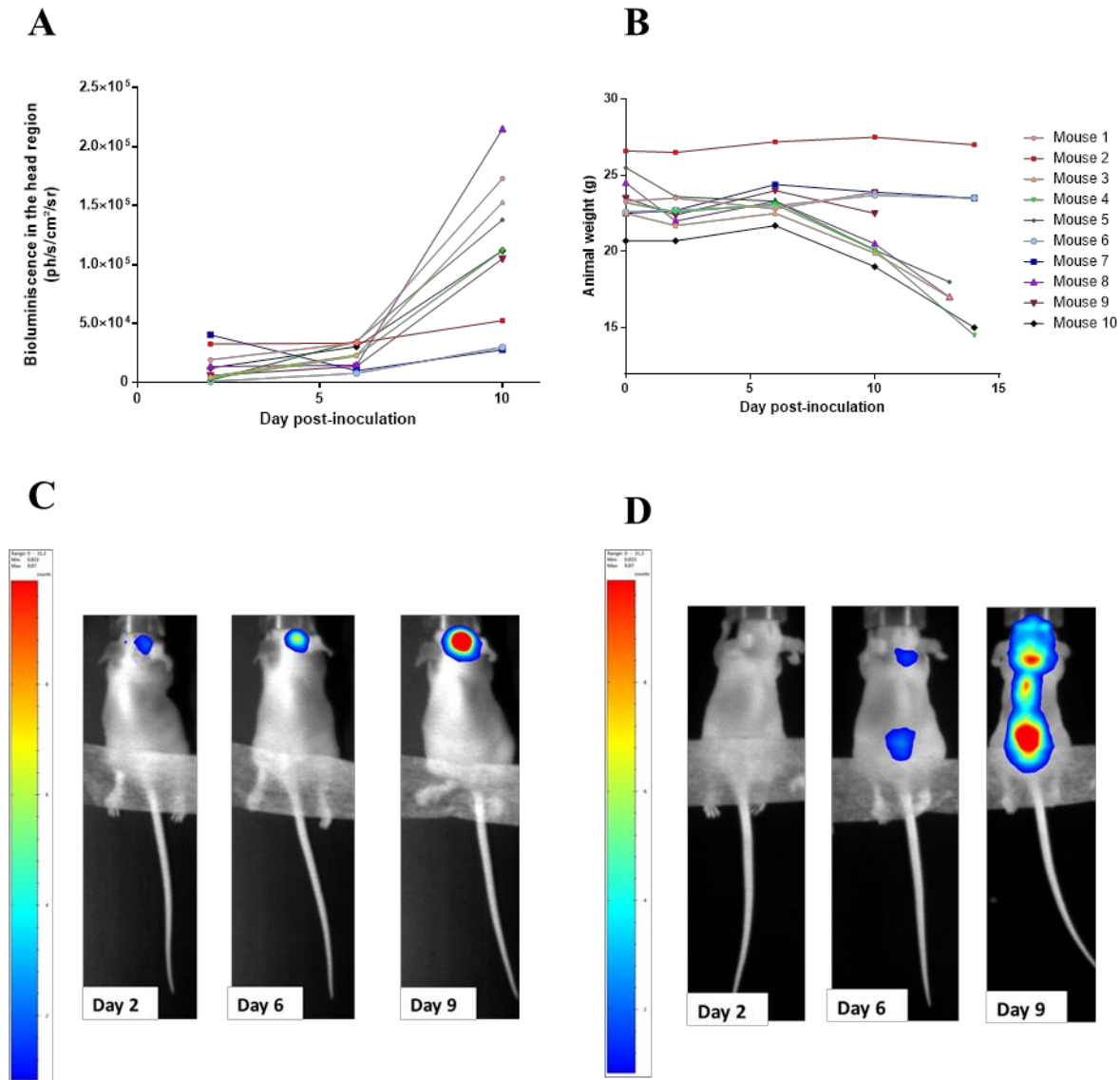
Figure 5.8: Typical animal weight and tumor growth follow-up pattern of brain tumor-inoculated mice. A: *Quantified BLI results expressed in captured photons per second per area of the head per steradian. This head area (region of interest, ROI) was the area over which photons were captured and was equalized over the different animals. Quantification was performed with the M3 vision software (Biospace Lab, Nesles-la-Vallée, France).* ***B:*** *Animal weight follow-up after inoculation. In many inoculated animals, a sudden and rapid weight loss in the days after inoculation was observed. Since animal experiments are legally bound to ethical boundaries and predetermined humane endpoints always need to be respected, not all animals were suited to participate in the eventual experiment.* ***C:*** *BLI images over time after Fluc$^+$ brain tumor inoculation of a mouse that developed a localized brain tumor.* ***D:*** *Typical pattern of evolution over time of mice that developed a brain tumor with metastasis to the spinal cord. Mice that show spinal cord metastasis (mice 3, 4, 5, 8, 9, 10 in B) generally show earlier weight loss and health decline compared to mice with a localized tumor. BLI Images were taken at 2 days, 6 days and 9 days after tumor inoculation and were visualized with the M3 vision software (Biospace Lab, Nesles-la-Vallée, France).*

When a drastic health decline occurred due to an unexpectedly fast tumor progression, the execution of experiments was hampered. This is because animal experiments are legally bound to predetermined ethical restrictions.

A 20 % weight loss or any animal-restricting neurological symptoms were in these cases considered as humane endpoints, at which animals could no longer take part in experiments. Since weight loss and health decline appeared so sudden in many animals, no anticipation could be undertaken in an appropriate time frame, and mice were sometimes lost. Practical restrictions – concerning the availability of radioactive materials with workable activities and the availability of the SPECT/CT scanner -, did not allow undertaking the experiments at time points dictated by the animals' conditions. Undertaking the imaging experiments animal by animal would however in great part cover the problem of heterogeneity. A shortening of the time in between tumor inoculation and targeting imaging would have the effect that some mice do not show a sufficiently developed tumor.

In one experiment, 200,000 instead of 250,000 tumor cells were inoculated, and this showed the evolution of only brain-localized tumors without metastasis. A great heterogeneity and drastic changes in the evolution of animal weight were however still observed. In the same group, not all animals had developed a tumor that was equally clear on BLI images in the two weeks' time frame, indicating that the inoculation of fewer tumor cells is not ideal. Ethical guidelines also restrict the inoculation of more animals in order to select and use a sufficiently large group showing the same type of evolution.

5.3. *In vivo* targeted nuclear imaging of hEGFR$^+$ brain tumors

Since no EGFRvIII-specific nanobody could be identified as a part of this master thesis, we refocused on the potential of nanobodies to target glioma cells in an *in vivo* brain tumor context. Hence, hEGFR$^+$ F98 rat glioma cells were inoculated intracranially in nude mice, and targeting was envisaged with the anti-EGFR nanobody 7C12 that recognizes wt hEGFR and hEGFRvIII with similar affinities, as determined by SPR (see above). The used cells were confirmed positive for the expression of wt hEGFR by flow cytometry (**figure 5.3**).

A first attempt in the targeted imaging of these brain tumors was made with a ^{99m}Tc-labeled His-tagged Nb7C12. However, the animals' condition was evolving in a very heterogeneous

and sudden way, due to the aggressive nature of the glioma cell line. Therefore, the experiment with ^{99m}Tc needed to be antedated. This however is not evident, since this isotope is not always readily available and has a half-life of only 6 h. Therefore, a very limited amount of activity was available to conduct the experiment. Both the anti-EGFR nanobody and the control nanobody had a radiochemical purity of over 99 % when injected. Because of the limited activity available however - 257 ± 17 µCi per mouse could be injected on average, while an injected activity of 0.5 - 1 mCi is envisaged -, no difference in tumor uptake was seen for the anti-EGFR nanobody compared to the non-targeting control nanobody on the SPECT/CT scans (**figure 5.9**). Both groups only showed uptake of the radioactive nanobody in the kidneys, which is expected since it is the route of nanobody clearance from the body (Krüwel, et al., 2016).
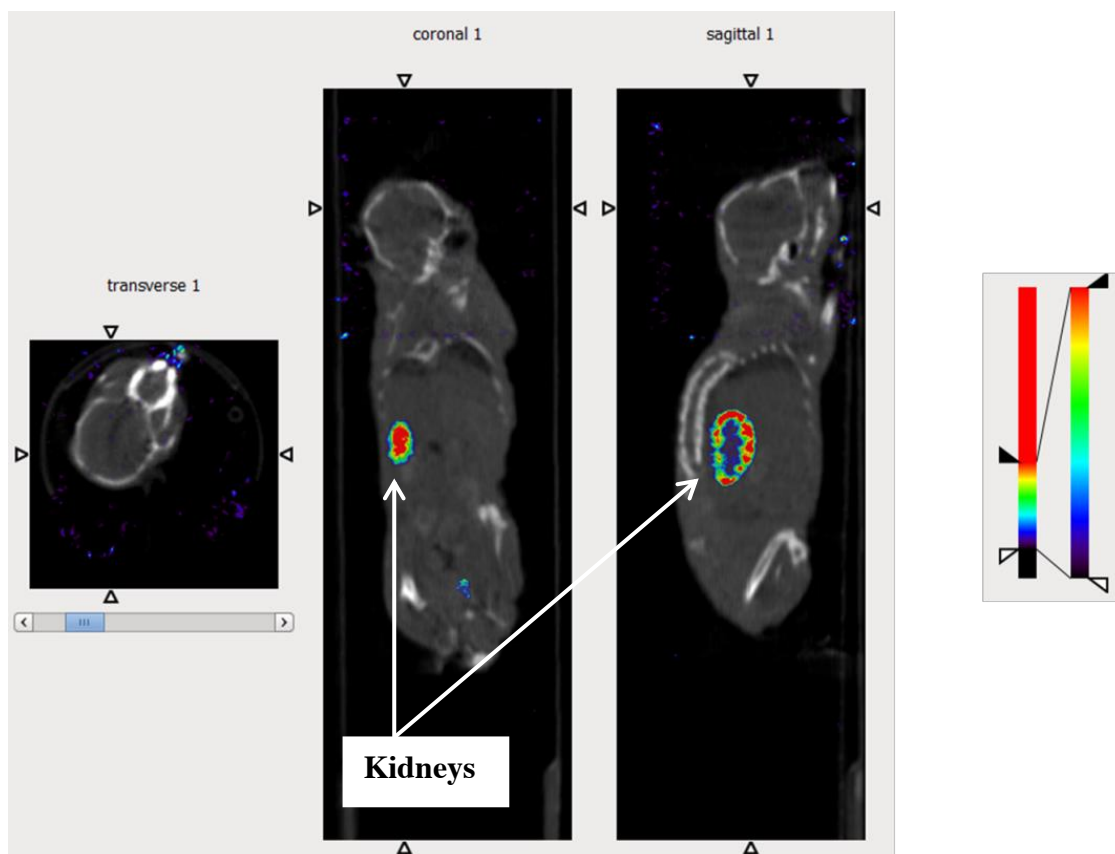

Figure 5.9: Transverse, coronal, and sagittal views of pinhole SPECT (brain-focused SPECT overlapped with full body SPECT) combined with micro-CT images of a F98 hEGFR$^+$ tumor-inoculated mouse, imaged 1 h after injection with ^{99m}Tc-labeled anti-hEGFR nanobody. No uptake of the radiotracer in the brain or in the tumor was observed, but this was potentially due to the limited amount of activity that was administered. The high uptake in the kidneys is expected since the kidneys are the route of nanobody clearance.

Ex vivo biodistribution results also did not indicate tumor-specific uptake, since uptake of the targeting nanobody and the control nanobody in the brain as well as in the tumor were very comparable (**figure 5.10**). Tumor uptake was significantly higher than uptake in healthy brain tissue for both nanobodies (values are shown in **figure 5.10**). This indicates a general BBB leakiness in the tumor area, or an influence of nanobody presence in the blood, which is possible since tumor tissue is highly perfused. In this case, the elevated uptake in the tumors would be an effect from bloodpool activity.
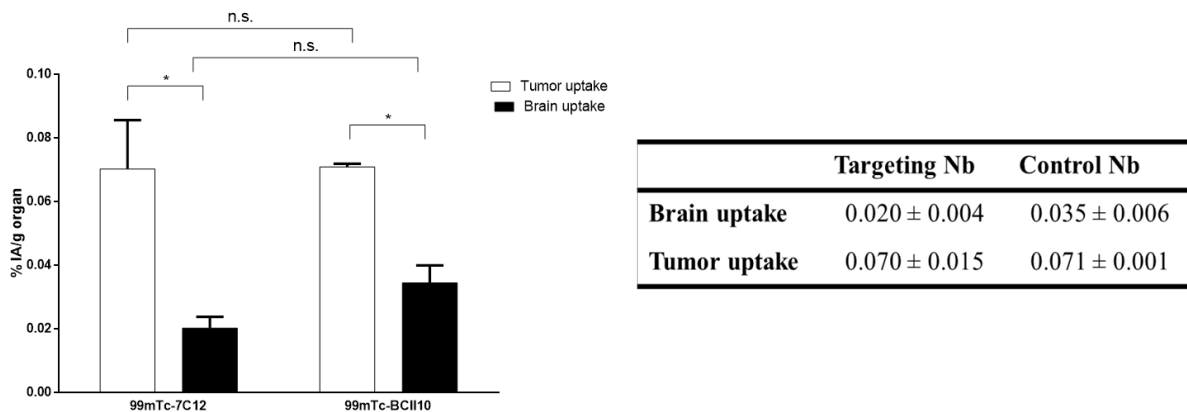

	Targeting Nb	Control Nb
Brain uptake	0.020 ± 0.004	0.035 ± 0.006
Tumor uptake	0.070 ± 0.015	0.071 ± 0.001

Figure 5.10: Ex vivo biodistribution results of the F98 hEGFR⁺ tumor inoculated mice, 1 h ***p.i. with the anti-EGFR Nb7C12-His-*** ^{99m}***Tc and the negative control NbBCI10-His-*** ^{99m}***Tc.*** *Mean values with SEM of the percentages of injected activity per gram organ are displayed in the brain as well as in the tumor. No significant difference in uptake of the targeting nanobody compared to the control nanobody was observed in the brain, nor in the tumor. A significant increase is however noticed in tumor uptake in general compared to brain uptake. This indicates leakiness of the BBB in the tumor region or nanobody presence in the tumor associated vascular system. Significant differences were determined for tumor and brain tissue by a two-tailed unpaired t-test and are marked by * (p≤0.05).*

Because tumor uptake was approximately the same with the targeting nanobody as with the control nanobody, no EGFR-specific targeting was observed. Since it was unclear if this was due to the limited injected activity or the incapability of the nanobody to track down the tumor lesions *in vivo*, the experiment was repeated with a radionuclide with a longer half-life. The half-life of ^{111}In is over 67 h, allowing a more flexible experimental planning when considering the animals' progression. Therefore, this SPECT radioisotope was used in a repeated experiment.

To radiolabel the anti-EGFR nanobody and the non-targeting nanobody with ^{111}In, they must first be conjugated to the DTPA bifunctional chelator. Therefore, an excess of the chelator was added to the immune protein and the reaction was allowed to proceed. The coupled protein was separated from the chelator using SEC. Elution of this nanobody from the SEC column showed that first the largest compound (the DTPA-labeled nanobody) eluted from the column, followed by unreacted DTPA and other possible contaminants (**figure 5.11**). All nanobodies that were conjugated to DTPA showed a similar elution profile from SEC.
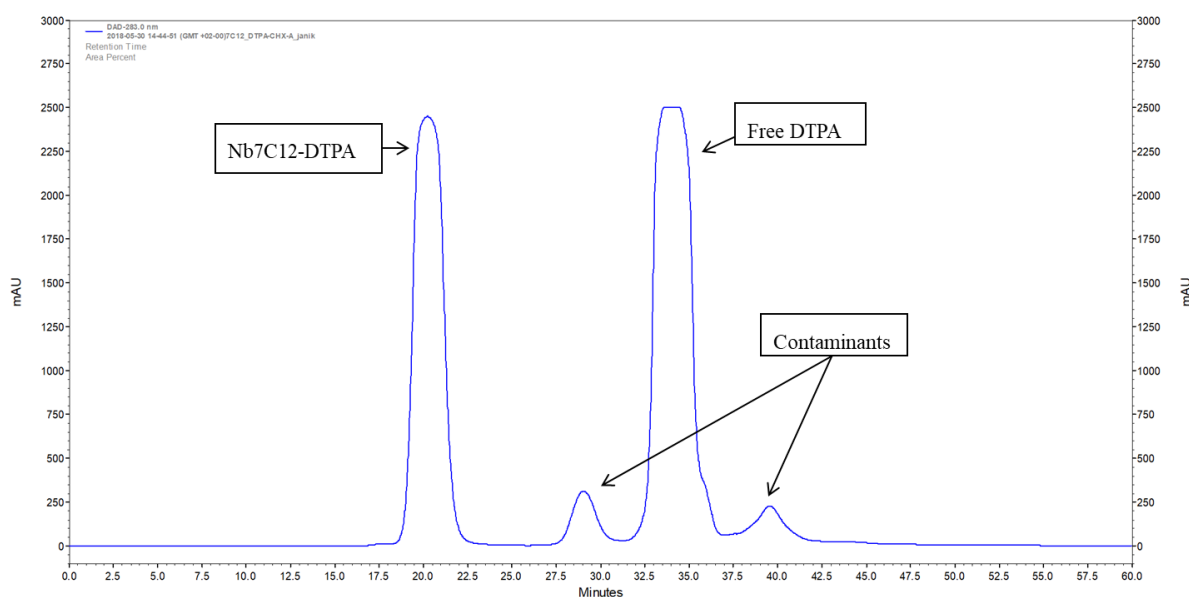

Figure 5.11: Chromatogram of the SEC column elution of the nanobody-DTPA construct and the present reagents and contaminants. *It was observed that the Nb7C12-DTPA elution peak on the chromatogram is clearly distinguished from the free DTPA peak and the contaminant peaks. Therefore, the chelator-conjugated nanobody was retrieved in a pure form after SEC. Displayed is the absorbance at 280 nm as measured at the end of the chromatography column, over time.*

After the radiolabeling procedure with ^{111}In, radiochemical purities of both the DTPA-conjugated targeting nanobody and the control nanobody were 100 %, indicating that the labeling with ^{111}In was very efficient. Although the injected activities were higher in these mice compared to the previous experiment (0.386 ± 0.030 µCi injected activity per mouse, which is acceptable since it is an energetically higher and a longer-lived isotope, meaning that limited decay will occur during the experiment and), no uptake of the targeting nanobody was seen in the brain tumor on the SPECT/CT scans with brain-focused SPECT. Uptake in the

spinal cord was also not observed in mice that showed metastasis to this area based on BLI imaging (**figure 5.12**).
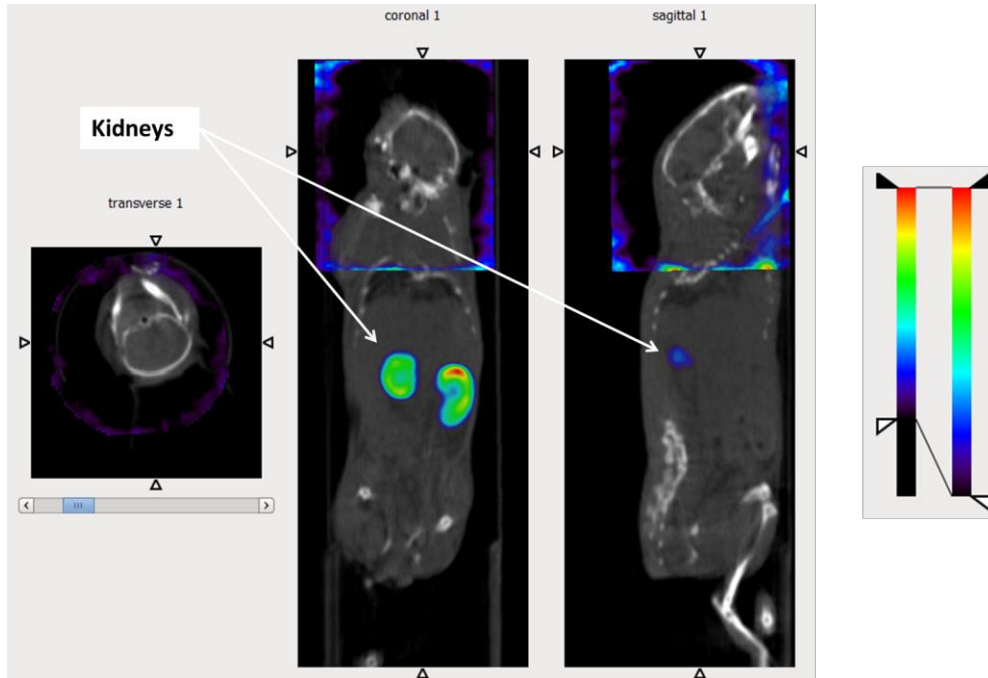

Figure 5.12: Transverse, coronal, and sagittal views of pinhole SPECT combined with micro-CT images of a mouse bearing a F98 hEGFR$^+$ brain tumor, taken 1 h post injection of the anti-EGFR Nb7C12-DTPA-^{111}In. No uptake in the brain or tumor region is observed, indicating that the tracer is not suited for tracing F98 tumors expressing the targeted receptor in vivo. Signal in the kidneys is high since this is the route of clearance from the body for nanobodies.

Ex vivo biodistribution data did show that tumor-uptake was significantly higher than uptake in the brain for the anti-EGFR nanobody (tumor: 0.114 ± 0.020 % IA/g organ, brain: 0.021 ± 0.003 % IA/g organ, $p = 0.002$) and the control nanobody (tumor: 0.028 ± 0.002 % IA/g organ, brain: 0.014 ± 0.002 % IA/g organ, $p = 0.007$). This was determined by a two-tailed unpaired t-test (**figure 5.13**).

Tumor uptake with the hEGFR-targeting nanobody (Nb) (0.114 ± 0.020 % IA/g organ) was also significantly higher compared to the tumor uptake of the negative control nanobody (0.028 ± 0.002 % IA/g organ, $p = 0.020$), which was not the case for healthy brain tissue (0.021 ± 0.003 % IA/g organ for the targeting nanobody and 0.014 ± 0.002 % IA/g organ for the negative control nanobody, $p = 0,200$). The latter indicates that targeting hEGFR$^+$ brain

tumors with Nb7C12-DTPA-^{111}In is possible, but the results remain somewhat inconclusive due to the very low amounts of activity taken up, and the realizing that the tumor uptake was too low to be visualized on the SPECT/CT scans with a brain-focused SPECT.
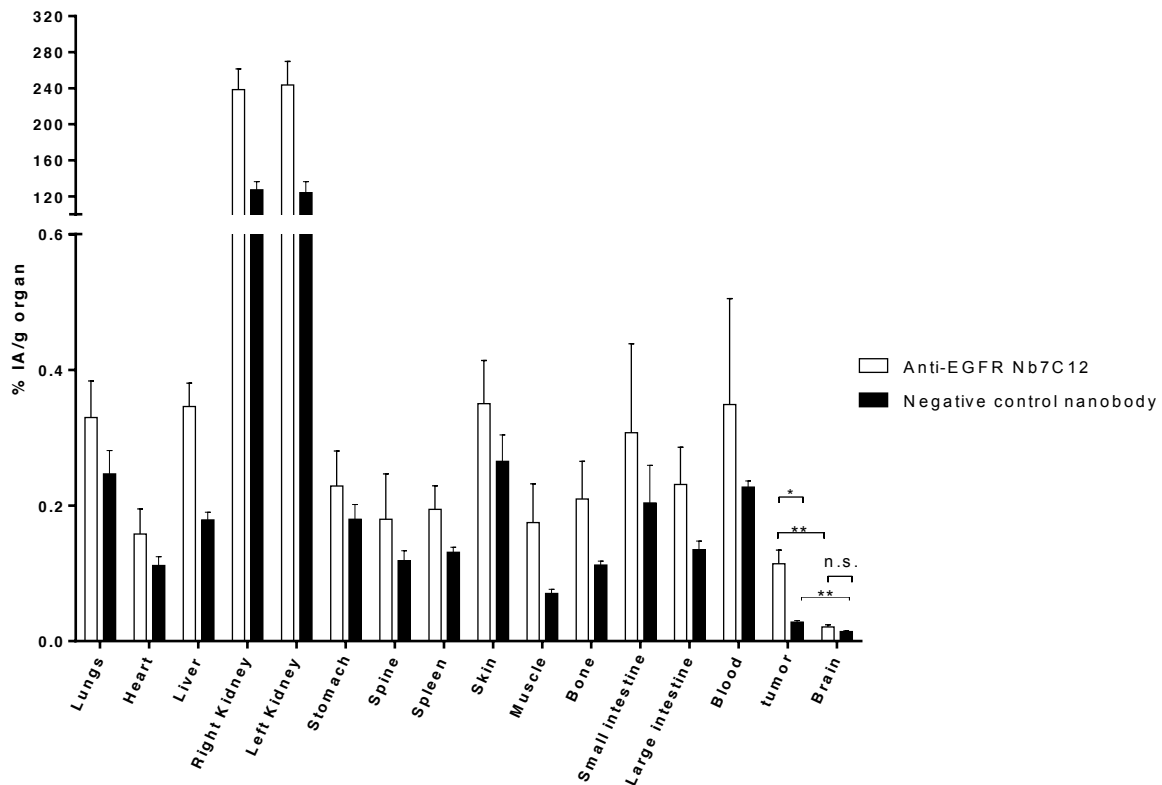

Figure 5.13: Ex vivo biodistribution results of the hEGFR+ F98 tumor inoculated mice, 1 h p.i. with the anti-hEGFR Nb 7C12-DTPA- [111]In and the negative control Nb R3b23-DTPA-[111]In. *Mean values with SEM of the percentages of injected activity per gram organ are displayed per isolated organ. Uptake in the kidneys is notably high, as expected since nanobodies are cleared via the kidneys. A significant difference in uptake of the targeting nanobody versus the control nanobody was observed in the tumor, indicating specific targeting to some extent. Of note, however, the uptake of the targeting nanobody is higher in every organ that was examined. Significant differences were determined for both groups in brain and tumor tissue by a two-tailed unpaired t-test and are marked by * (p≤0.05) and ** (p≤0.01).*

Therefore, even if there is targeting to some extent, it is not biologically relevant. Also, **figure 5.13** shows that Nb7C12-uptake is elevated compared to uptake of the control nanobody in every organ that was analyzed, and that the uptake in the tumor is the lowest of all organs,

except the brain. These observations, together with the observation that tumors were not visible on the SPECT/CT scans, indicate that brain tumor targeting is not sufficiently specific and/or the nanobody cannot reach its targeted antigen sufficiently *in vivo*.

Since the *in vivo* uptake of this radiolabeled nanobody in tumors was much lower than expected, experiments were conducted to assess whether the different labeling strategy had affected the affinity of the nanobody for the targeted receptor. Both an SPR assay and an *in vitro* binding assay were performed to answer this question.

The SPR assay was performed both with the Nb7C12-His and Nb7C12-Notag-DTPA on immobilized recombinant hEGFRvIII protein. The binding of Nb7C12-His to the hEGFRvIII protein showed an affinity of 19.2 nM, while this affinity dropped to 748 nM for the Nb7C12-notag-DTPA protein (**figure 5.14**).

k_a (M^{-1}s^{-1})	7.54×10^{5}
k_d (s^{-1})	1.45×10^{-2}
K_D (nM)	19.2
Chi²	1.60

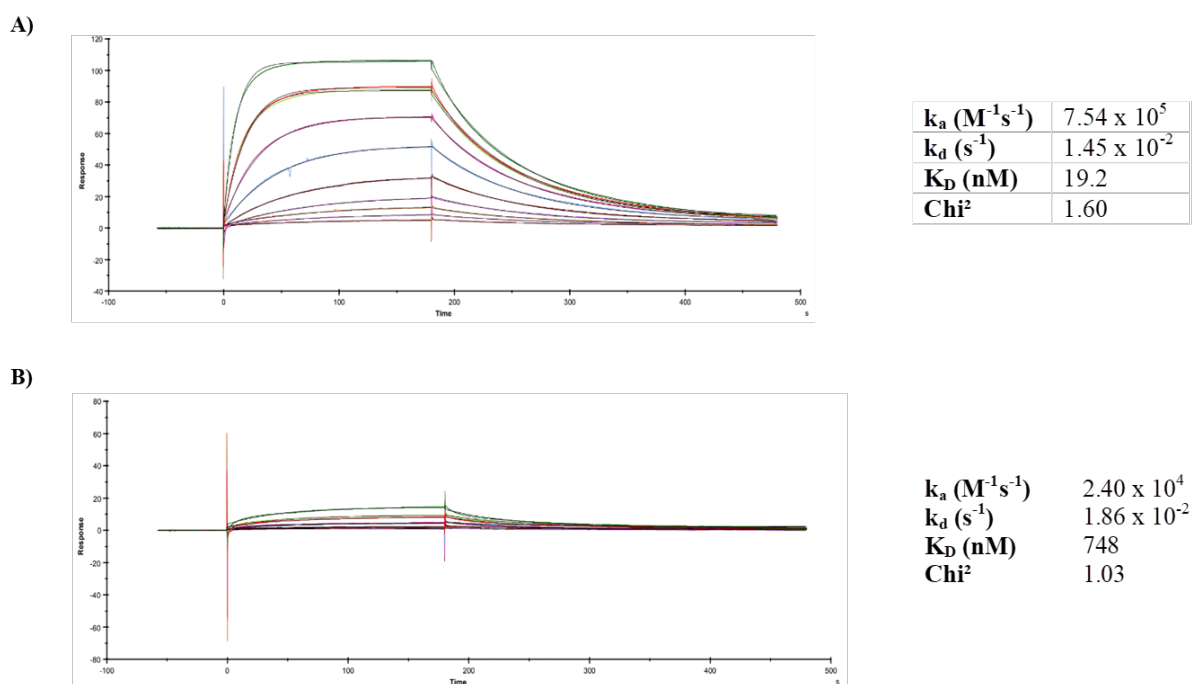|	
k_a (M^{-1}s^{-1})	2.40×10^{4}
k_d (s^{-1})	1.86×10^{-2}
K_D (nM)	748
Chi²	1.03

Figure 5.14: Surface plasmon resonance results of (A) Nb7C12-His and (B) Nb7C12-notag-DTPA binding to recombinant hEGFRvIII. Fitting and parameter calculation was performed with a one-to-one binding model with drift and RI2. The k_a, k_d and K_D values are shown in the insert.

This drastic drop in affinity explained the non-potential of the nanobody to bind its target *in vivo* in the current experiments. An *in vitro* cell binding assay of Nb7C12-notag-DTPA labeled with ^{177}Lu on hEGFR$^+$ F98 cells and hEGFR$^-$ CHO cells confirmed the very weak binding. The radiolabeling was performed with ^{177}Lu, which uses the same chemistry as ^{111}In labeling of DTPA-coupled compounds. It was observed that the radiolabeled nanobody binds less to hEGFR$^+$ F98 cells than to hEGFR$^-$ CHO cells, at all tested concentrations (**table 5.1**). These results confirm that the radiolabeling strategy of this nanobody abolished its potential to target the hEGFR protein.

Table 5.1: Percentages with standard deviation of cell-bound activity of Nb7C12-DTPA-^{177}Lu to hEGFR$^+$ F98 cells and hEGFR$^-$ CHO cells, at different nanobody concentrations. The radiolabeled nanobody was found to bind even less to hEGFR-expressing F98 cells than to hEGFR-negative CHO cells, at concentrations up until 500 nM. All cell-bound activity remained under 1 % of the total measured activities, indicating that no binding of the radiolabeled nanobody occurs to either of the cell lines, at any concentration.

	10 nM	50 nM	100 nM	500 nM
Binding to hEGFR$^-$ CHO cells	0.62 ± 0.19	0.41 ± 0.10	0.53 ± 0.30	0.35 ± 0.03
Binding to hEGFR$^+$ F98 cells	0.34 ± 0.14	0.27 ± 0.01	0.28 ± 0.08	0.17 ± 0.01

The Nb7C12 sequence contains 4 lysine residues: one in the framework two region and three in the framework three region, following the classical IMGT alignment (Gainkam, et al., 2008). Therefore, no issues in loss of affinity were expected due to the coupling of DTPA to the lysine residues of the protein.

A possible explanation of the loss of affinity due to the coupling of DTPA to the immune protein, lies in how Nb7C12 binds the hEGFR antigen. This was determined by Schmitz and co-workers (Schmitz, et al., 2013). They discovered an unusual folding of the CDR3 region of Nb7D12 upon antigen binding. The CDR variable region bends over the framework region, in a way that the antigen recognizing paratope is not protruding, as is sometimes observed, but rather forms a flat surface. Possibly, coupling of DTPA to the lysines in the framework is structurally impeding the proper loop bending over the framework region.

From these experiments, no firm conclusions could be drawn regarding the brain tumor-targeting potential of nanobodies in a glioma context. Experiments should be repeated with a DTPA-independent radiolabeling strategy to evaluate the nanobody's *in vivo* potential. The hypothesis that a nanobody with sufficient *in vivo* affinity can reach its intracerebral target antigen still stands, since uptake of a radiolabeled nanobody in the brain was observed in a phase I clinical trial, as described above (**figure 2.10**).

5.4. Comparison of HER2-specific antibodies and nanobodies as tracers in *in vivo* targeted nuclear imaging

A third important goal in this master thesis project was the comparison of antibodies and nanobodies as tracers for targeted nuclear imaging in the context of brain tumors. To compare these different entities, a model of HER2$^+$ breast cancer brain metastasis – a medically very important phenomenon -, was considered. An intracranial injection of HER2$^+$ cancer cells (MDA-MB-231 triple negative human breast cancer cell line with transfected HER2 receptor) in nude mice led to brain tumor development. These animals were imaged with SPECT/CT after injection of radiolabeled nanobodies - the existing anti-HER2 Nb2Rs15d, that is currently in phase II clinical trials as a novel radiodiagnostic compound for breast cancer (Vrije Universiteit Brussel, 2015) - and the radiolabeled anti-HER2 antibody trastuzumab, a clinically approved compound that blocks functioning of the HER2 receptor (Food and Drug Administration, 2012). This nanobody is well-characterized and many preliminary data are available describing its *in vivo* behavior. In this thesis, it is now envisaged to evaluate its potency in brain tumors and to compare it with that of the approved antibody. All imaging experiments were conducted with the ^{111}In radioisotope, which required a conjugation of the immune proteins to the DTPA bifunctional chelator.

DTPA coupling of nanobodies were successful and showed a similar elution profile from SEC as shown in **figure 5.11**. The chromatogram of SEC elution from the antibody-DTPA construct showed fewer impurities, as was expected since this is a patient-approved, commercially available product (Herceptin$^®$) (**figure 5.15**).

After radiolabeling the DTPA-coupled immune proteins, the radiochemical purities of the Nb2Rs15d-DTPA-^{111}In constructs were over 98 % in every conducted experiment. For the trastuzumab-DTPA-^{111}In construct, the radiochemical purity of the final sample was 92.2 %,

indicating that this radiolabeling is less efficient to some extent. This is lower than the standard minimal radioactive purity of 95 %. The lower radiochemical purity might partly influence the activity's biodistribution, since free ^{111}In or ^{111}in-DTPA accumulates in the urinary tract. Therefore, radioactive uptake in organs related to the urinary excretion system might be slightly higher than expected (Vallabhajosula, et al., 2010).

To confirm the suitability of the HER2-transfected MDA-MB-231Br cell line to be targeted with HER2-specific tracers, this cell line was tested in an *in vitro* binding assay with Nb2Rs15d-DTPA-^{111}In. Two other cell lines were tested as controls: the HER2$^-$ CHO cell line and the naturally HER2-expressing SKOV3 cell line.
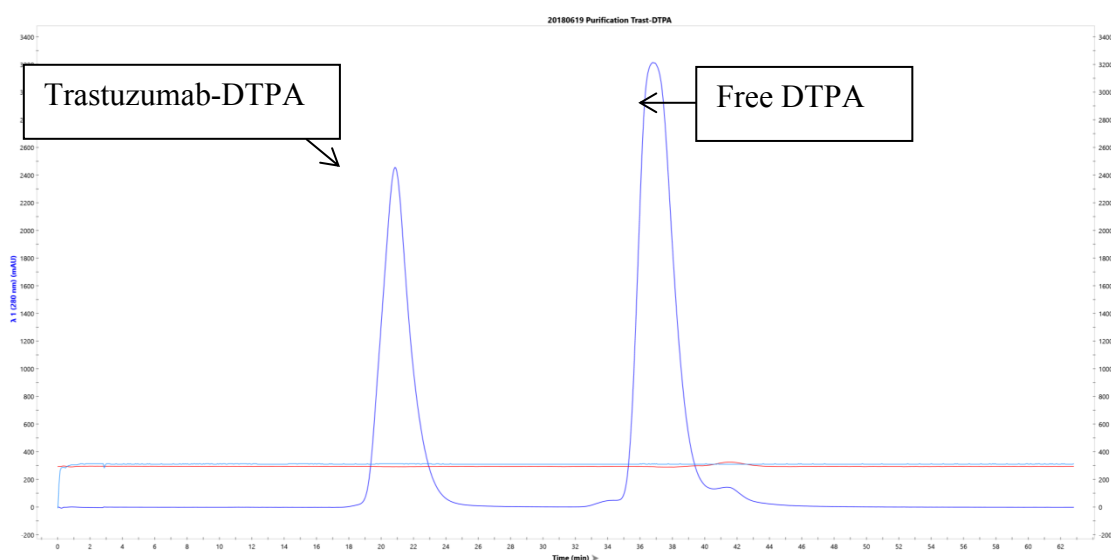

Figure 5.15: Chromatogram of elution of trastuzumab-DTPA from the SEC column. Two peaks were observed. In the first peak, the antibody-DTPA conjugate was eluted from the column, and in a second peak, the free chelator left the column. No other contaminants were observed to be present.

The *in vitro* cell binding assay revealed that the percentages of the relative cell-bound radioactivity at 100 nM of the radiotracer were 20.65 ± 0.54 % in case of incubation with HER2$^+$ MDA-MB-321 cell line, compared to 10.08 ± 0.13 % when incubated with HER2$^+$ SKOV3 and 1.69 ± 0.23 % with HER2$^-$ CHO cells. The trend of a higher HER2 expression in MDA-MB-231Br cells compared to SKOV3 cells and CHO cells was observed at all tested
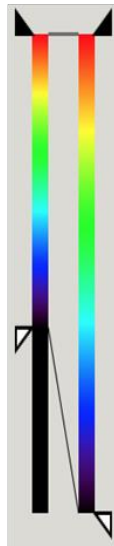
Brain tumor

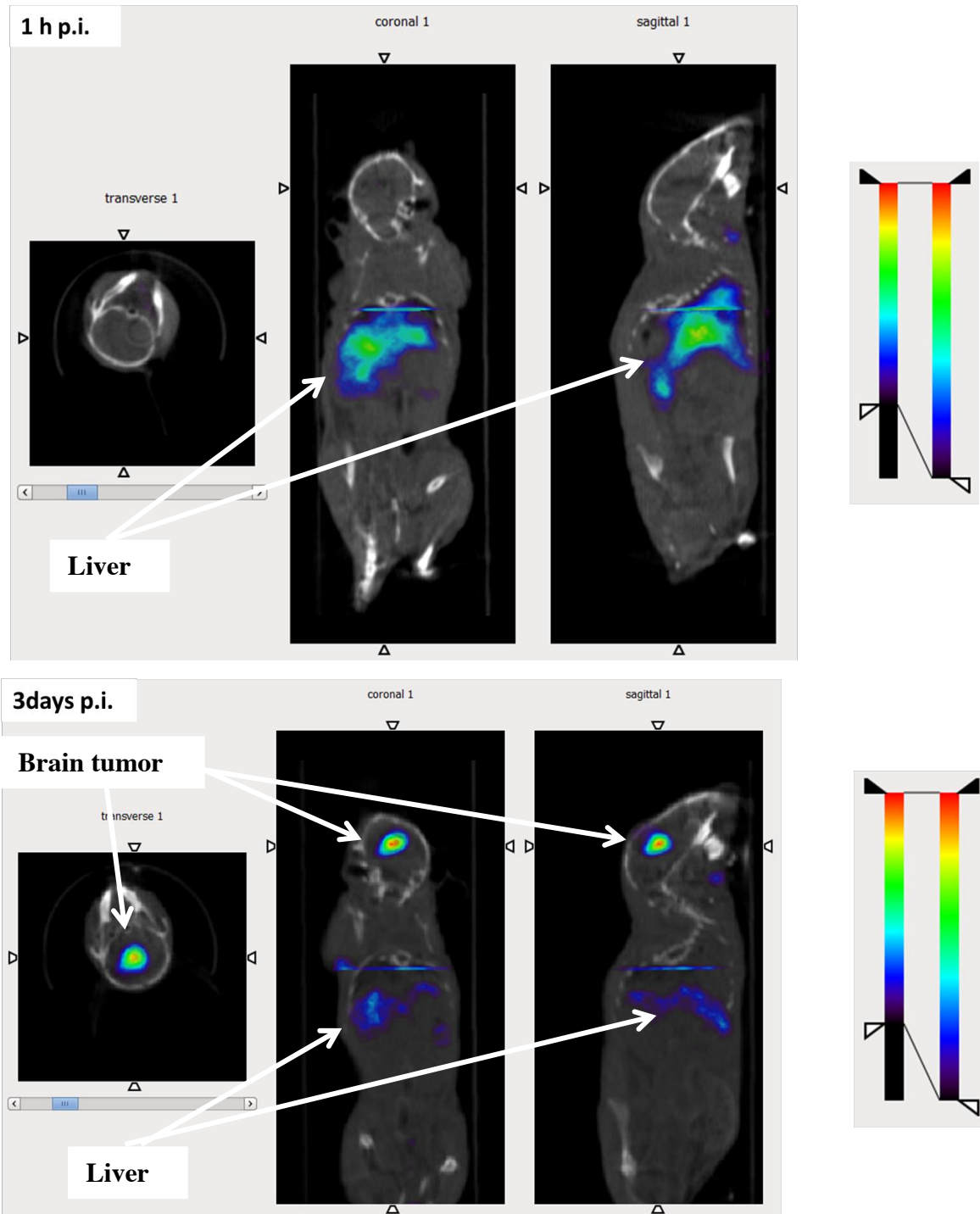**Kidneys**

transverse 1
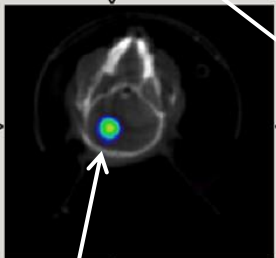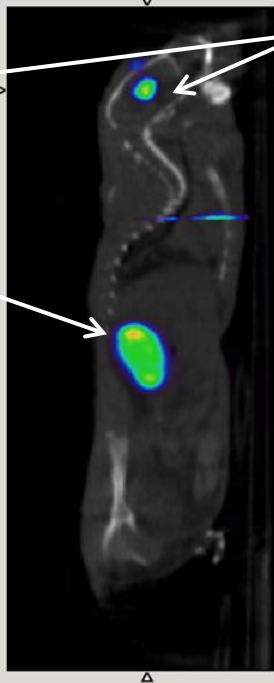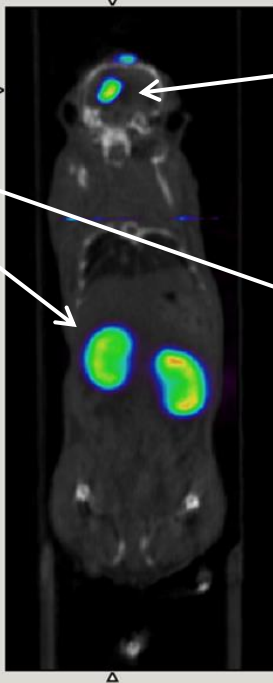
Brain tumor

Figure 5.17: Transverse, coronal, and sagittal views of pinhole SPECT scans (whole body and brain-focused) combined with whole body micro-CT images of a nude mouse bearing a HER2+ brain tumor, taken 1 h (upper) and 3 days (lower) post injection of trastuzumab-DTPA-111In. *At 1 h p.i. of the radiotracer, no brain tumor targeting was observed as only the uptake in the liver was high enough to be visible on the combined scans. The time point of 3 days p.i. did show a clear accumulation of the radiotracer in the tumor area and revealed a great tumor-to background contrast.*

On the SPECT/CT scans at 1 h p.i. of the trastuzumab-DTPA-^{111}In compound, no intracranial tumor targeting was observed, as was expected since distribution of antibodies is known to be very slow. No uptake in the kidneys is observed either since this is not the route of clearance for antibodies. In case of the radiolabeled nanobodies, high uptake in the kidneys was seen after 1 h. The antibody showed high liver accumulation at 1 h p.i.. This is because the compound resides in the blood for a long time and the liver is a highly-perfused organ. Also, certain IgG-specific receptors are highly expressed by hepatocytes, and therefore liver retention of the radiolabeled antibody is seen. These receptors include the neonatal Fc receptor (FcRn), the binding of which protects IgGs from lysosomal degradation, and other Fcγ-receptors (Vriesendorp & Vriesendorp, 2003). To some extent, binding of the Fc-associated glycans to lectins on hepatocytes contributes as well to the liver retention of the antibody (Gorovits & Krinos-Fiorotti, 2013).

SPECT/CT images gathered 3 days post injection of trastuzumab-DTPA-^{111}In, did show high tumor uptake and a much lower signal in the liver compared to 1 h p.i. (**figure 5.17**). This indicates that the antibody is appropriate to track tumor lesions within the brain in a HER2$^+$ MDA-MB-231Br model of BCBM, 3 days post injection. These results were unexpected since (unpublished) data gathered at the ICMI lab did not show this potential of the antibody in an intracranially implanted HER2$^+$ SKOV3 tumor model (**table 5.2**). In these previously-obtained data, only the nanobody could reach its intracranial target, while the antibody did not, assumingly because it was too large.

Table 5.2: Ex vivo biodistribution results previously obtained at the ICMI lab. *Uptake of the radioactive compounds was measured in mice bearing an intracranial HER2$^+$ SKOV3 xenograft tumor. The same procedures as described in this master thesis were followed for the tumor inoculation and the targeted imaging.*

	2Rs15d-His -^{99m}Tc, 1 h p.i.	Trastuzumab- DTPA- ^{111}In, 3 d p.i.
Tumor uptake	2.38 ± 1.8 % IA/g organ	0.75 ± 0,4 % IA/g organ
Tumor/blood ratio	6.4	0.10
Tumor/brain ratio	36.5	0.95

Recently published data suggest that the size of antibodies – such as trastuzumab – is not the (only) cause for inadequate outcomes in HER2$^+$ BCBM therapy, but that the microenvironment in the brain is in part responsible for a downregulation of the therapeutics' effects. It has been shown that trastuzumab does penetrate BCBM lesions in human patients, but cannot execute its function properly because of an over activated PI3K-AKT-mTOR pathway in this area (Kabraji, et al., 2018). Taken together, our current results agree with these published data, namely that the anti-HER2 antibody can reach its brain-localized target in a tumor environment, when sufficient time to distribute is allowed. Since previous research in a SKOV3 model of BCBM showed no uptake of the antibody in the brain tumor lesion, while uptake was observed when using the nanobody, it is thought that cell line invasiveness as well as vascularization of the tumor are important parameters for antibody penetration. In that case, nanobodies might have the advantage of reaching smaller, less developed tumors, which would be an important advantage, both in a diagnostic and a therapeutic context. Also, nanobody-based radiotherapy would circumvent the described problem of the decreased therapeutic efficacy of trastuzumab in the brain.

The obtained *ex vivo* biodistribution results confirmed what was seen on the SPECT/CT images, namely that the uptake of the radiolabeled antibody in the brain tumor (23.180 ± 5.441 % IA/g organ) was much higher compared to the radiolabeled nanobody (0.636 ± 0.214 % IA/g organ). This was statistically confirmed with a two-tailed unpaired t-test with $p < 0.0001$ (**figure 5.18**).

With both tracers, average uptake in the brain is the lowest of all tested organs, while tumor uptake is the highest – except for kidney uptake in the nanobody group. In addition, tumor uptake was significantly higher than brain uptake with both tracers. For the nanobody, tumor uptake was 0.636 ± 0.210 % IA/g organ, while brain uptake was only 0.038 ± 0.006 % IA/g organ ($p = 0.013$). The uptake of trastuzumab in the tumor was 23.180 ± 5.441 % IA/g organ, while brain uptake was 0.756 ± 0.160 % IA/g organ ($p = 0.015$). This indicates a site-specific biodistribution and an effective crossing of the BBB in tumor regions and not in healthy brain tissues. Both the nanobody and the antibody tracer were capable of such in tumor regions, however not to the same extent as previously observed in a HER2$^+$ SKOV3 model of BCBM (**table 5.2**). Tumor-to-brain ratios were 16.7 for the nanobody and 30.7 for the antibody. These data confirm what was seen on the SPECT/CT images and emphasize the potential of both tracers to reach brain-located tumor lesions *in vivo*.
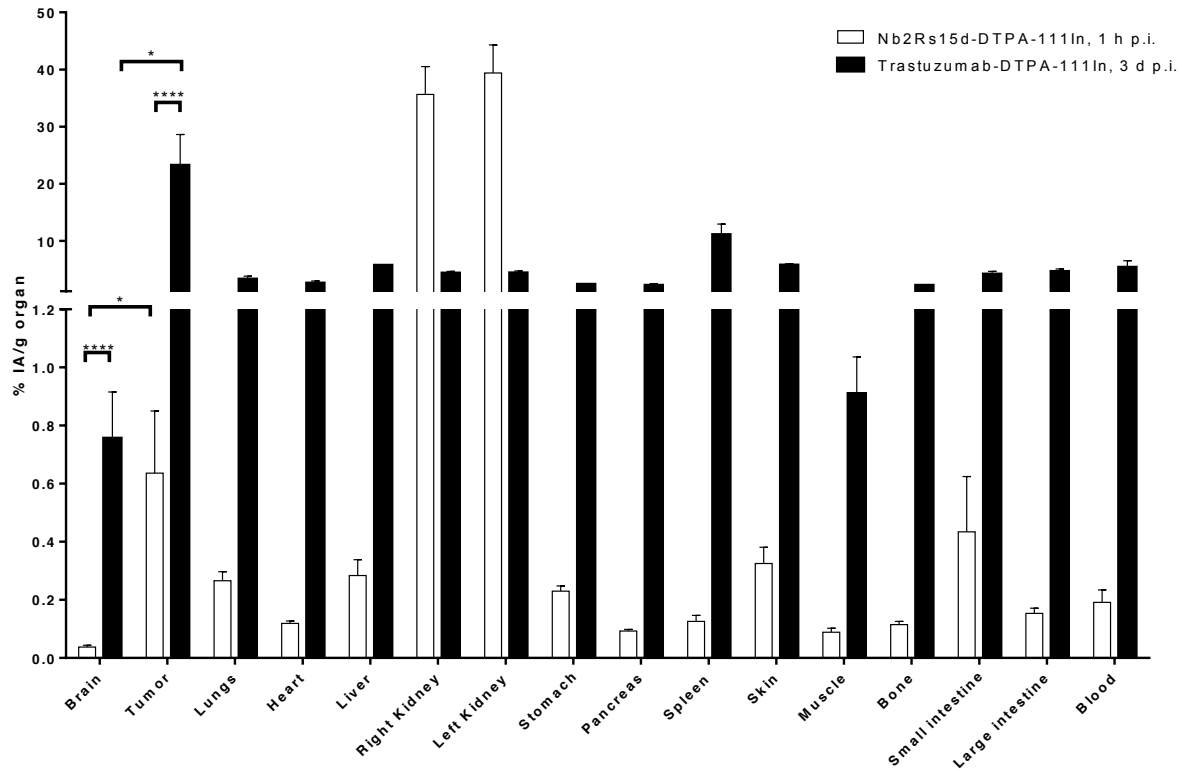
*Figure 5.18: Ex vivo biodistribution results of the targeted imaging experiment with anti-HER2 Nb2Rs15d-DTPA-^{111}In, 1 h p.i. and anti-HER2 antibody trastuzumab-DTPA-^{111}In, 3 days p.i. in mice brearing HER2^{+} MDA-MB-231 brain tumors. Mean values with SEM of the percentages of injected activity per gram organ are displayed. Tumor uptake is significantly higher in tumors targeted with trastuzumab compared to nanobody uptake, as is brain uptake. In both the nanobody as the antibody group, tumor uptake was significantly higher compared brain uptake. Significant differences were determined for both groups in brain and tumor uptake by a two-tailed unpaired t-test and are marked by * (p≤0.05) and **** (p ≤ 0.0001).*

Published data show that the accumulation of trastuzumab in subcutaneous HER2^{+} SKOV3 tumors at 3 days p.i. (22.85 ± 4.24 % IA/g tumor) is higher than Nb2Rs15d uptake at 1 h p.i. (6.50 ± 0.24 % IA/g tumor) (D'Huyvetter, et al., 2014a). These results are in agreement with the data obtained here, namely that the absolute uptake of trastuzumab in HER2^{+} tumors is higher than nanobody uptake, but that this requires a prolonged biodistribution.

Though in absolute values the antibody is a much more potent HER2^{+} brain tumor tracer, it needs much more time to attain this tumor-to-brain contrast compared to the nanobody. This quicker distribution to the target sites is of great importance when performing nuclear imaging or eventually targeted radionuclide therapy. A shorter biodistribution time corresponds to reduced radiation exposure time for healthy tissues, which is a highly valuable feature of

nanobodies in this context. This is however only the case if damage to the kidneys is of acceptable levels.

Question remains as to whether antibodies can target disseminating cells that are further away from the bulk of the brain tumor, at sites where the BBB might be more intact and tumor lesions are not yet full-fledged. It is our hypothesis that nanobodies could be more efficient in targeting these sites compared to antibodies, as was observed in SKOV3 tumors. These SKOV3 tumors were less invasive compared to the MDA-MB-231Br tumors, since a much more moderate and homogenic tumor development and animal evolution were observed. The option that nanobodies can reach their targeted antigens in an earlier stage of tumor development compared to antibodies is still at question as well. Future research at the ICMI lab will focus on the moment in tumor progression at which nanobodies become valuable in targeting the brain tumor compared to antibodies. The hypothesis here is that nanobodies can reach the cancer cells in an earlier stage of tumor development compared to antibodies.

5.5. Improved tumor isolation using GFP-positive cells or image-guided dissections

Brain tumor tissue is hard to distinguish from healthy brain tissue by the naked eye. This has proven to be very challenging in the *ex vivo* animal dissections. However, a correct isolation of tumor tissue from brain tissue is of great importance for the reliability of the *ex vivo* biodistribution results. The uptake of the radiotracer is indeed measured per isolated tissue type, and normalized to the weight of the sample. Therefore, if the tumor tissue is not isolated properly, and healthy brain tissue is excised, this extra weight will lower the quantified uptake in the *ex vivo* biodistribution results. The reverse also applies: any tumor tissue that is categorized as brain tissue will influence the uptake measured in healthy brain. Since these tissue types have such a low mass, small differences in the sample weights can have great effects on the *ex vivo* biodistribution data.

During this master thesis, ways to circumvent this problem were investigated. A first possibility to do this was offered by the use of GFP-positive tumor cells for inoculation. During dissections, this GFP-signal could be used to delineate the tumor tissue within the mice's brains. This was possible by FLI measurements capable of localizing the GFP-signal on images of the brain. **Figure 5.19** shows that this is an effective manner of tumor

localization within isolated brains. In all mice, the location of GFP-positive cells matched with the site of tumor inoculations, with further dissemination in some cases.
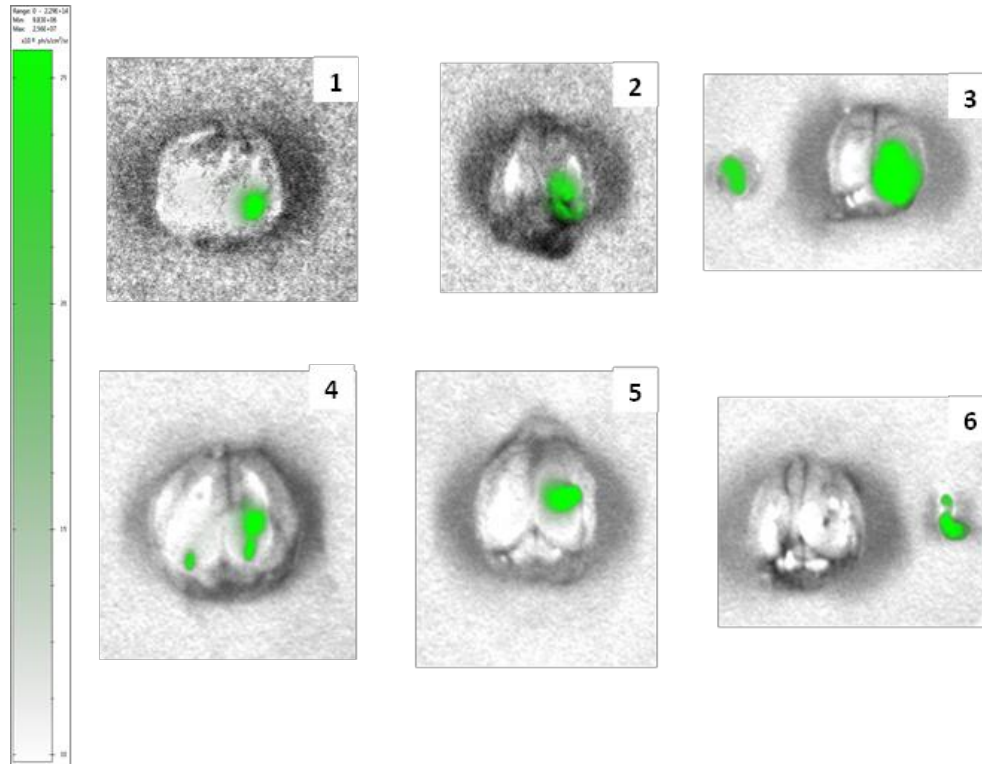

Figure 5.19: FLI images of brains isolated from mice inoculated with an intracranial GFP$^+$ MDA-MB-231Br tumor. A brain tumor is clearly visible in all mice. In mouse three, a subcutaneous tumor part was isolated during dissections, but an intracranial tumor was clearly visible on FLI as well.

When these images were compared with the SPECT/CT scans from the targeted imaging experiment, a correlation was seen in the tumor localization within the brain and the radioactive tracer accumulation *in vivo* (**figure 5.20**).

Since these images only gave a rough idea about tumor localization and the status of tumor cell migration from the site of inoculation, tumor isolation was still not adequate. A first improvement in the tumor isolation was still based on the GFP-signal of tumor cells. Isolated brains were submitted again to FLI measurements to localize the GFP signal, after which dissections were performed to cut the brain into several fragments. These fragments were

submitted again to FLI measurements, and this was done in an iterative way until the point at which the tumors were thought to be isolated (**figure 5.21**).
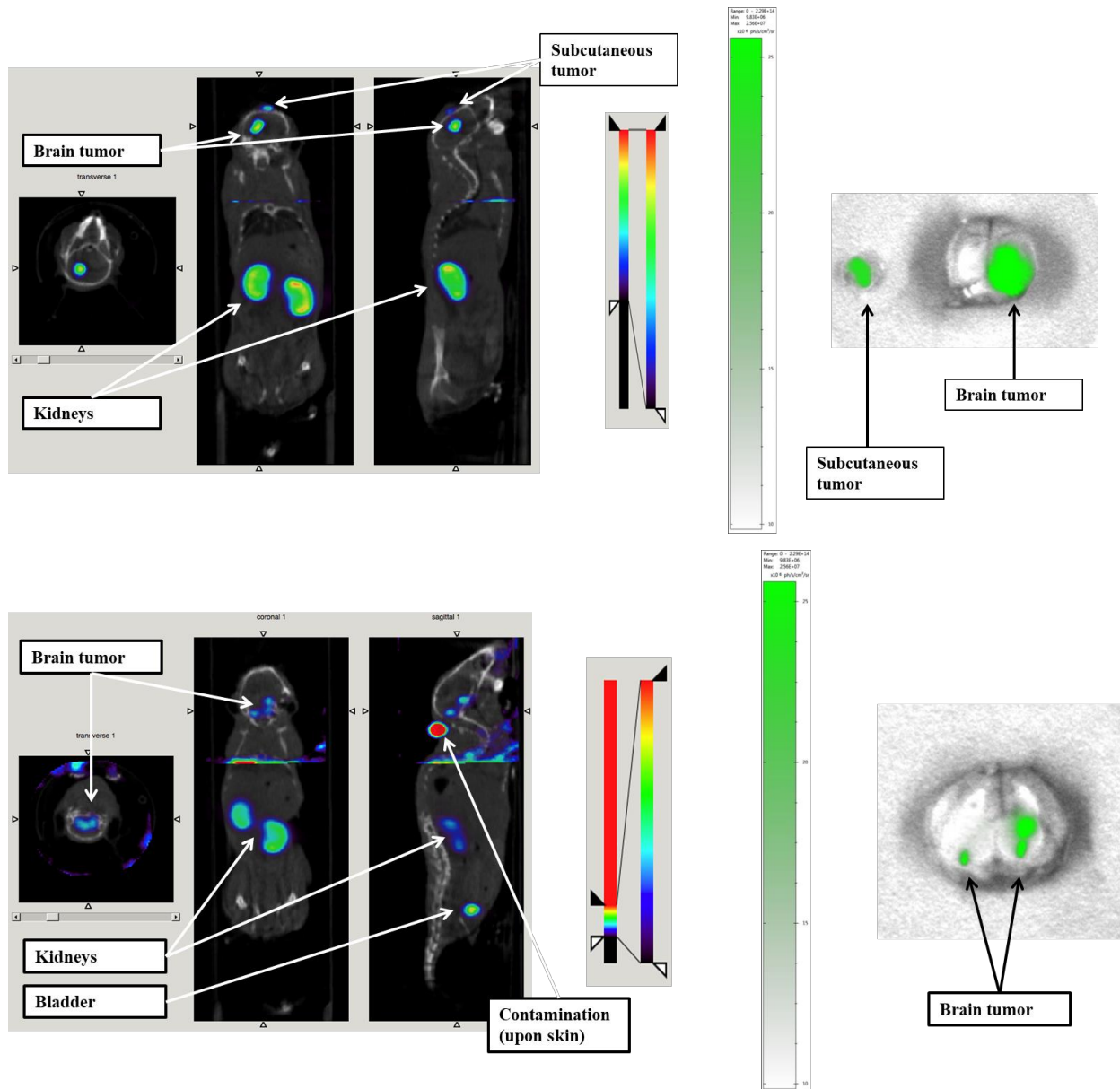

Figure 5.20: Two examples of the correlation between the FLI image of the brain, localizing the brain tumor (right) and the tracer accumulation as observed on SPECT/CT scans with brain-focused SPECT (left). In the upper example, both a subcutaneous and an intracranial brain tumor is observed in FLI, and on the SPECT/CT scan obtained 1 h after injection of the ^{111}In-labeled anti-HER2 Nb2Rs15d Nb. The lower image shows the same overlap in tumor localization as seen on FLI and as tracked down by the radioactively labeled nanobody. In this case, the tumor had disseminated to three subparts, as observed by FLI. These three subparts are visible on the sagittal cross-section of the 3D SPECT/CT scan, indicating that the nanobody was capable of tracking these three disseminated regions.
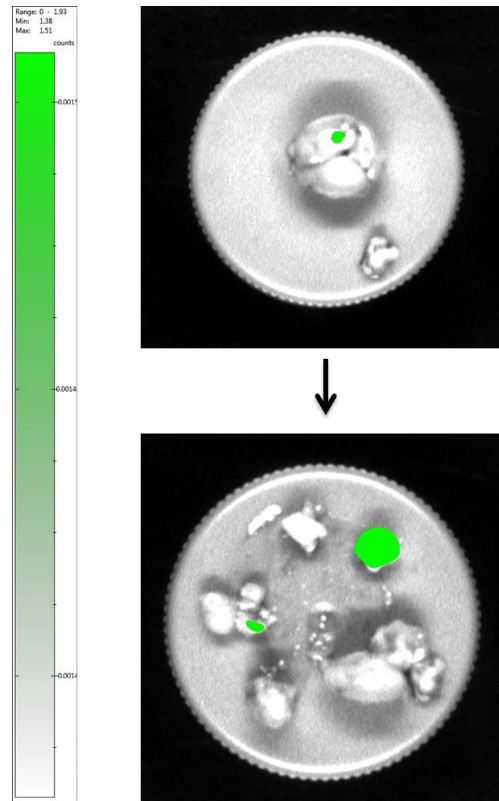
Figure 5.21: FLI images acquired during iterative brain dissections, based on the localization of the GFP-positive brain tumor cells.

Because these images were still sensitive to the scaling in the M3 vision software, this approach allowed isolating a part of the brain that contains the brain tumor, but the edges of this isolated part could still be healthy brain tissue. Also, this technique is based on a GFP-positive cell line, which demanded a cell transduction, and is therefore not applicable for naïve cell lines.

To circumvent the previous disadvantages, the combined use of targeted nuclear imaging and optical imaging was considered. Therefore, mice with an intracranially inoculated GFP$^+$ HER2$^+$ MDA-MB-231Br tumor were first injected with the radiotracer to be tested and after 1 h, right before the initiation of the SPECT/CT scan acquisition, the IRDye800-coupled anti-HER2 nanobody was injected as well. One hour p.i. of the fluorescently labeled nanobody, mice were sacrificed and dissected under real-time optical image guidance.

The isolated brains were first submitted to FLI, in which both the signal of GFP (excitation wavelength = 488 nm, emission wavelength = 510 nm, filter cut off = 505-540 nm) and the signal of IRDye800 (excitation wavelength = 774 nm, emission wavelength = 789 nm; filter cut off = 780–815 nm) were measured. It was observed that there was an overlap in the localization of both signals in the brain, indicating that the fluorescently labeled nanobody could effectively reach its target cells *in vivo* and that the localization of the accumulation of this fluorescent tracer could be used to identify tumor tissue from healthy tissue (**figure 5.22**). This overlap was observed both in the group that was submitted to nuclear imaging with the nanobody tracer (Nb2Rs15d-DTPA-^{111}In) as with the antibody tracer (trastuzumab-DTPA-^{111}In). The latter was to be expected since it was shown by Vaneycken and co-workers that trastuzumab and the nanobody do not compete for HER2 binding (Vaneycken, et al., 2011a). The fact that this overlap was seen when the same nanobody tracer was administered for both optical and for nuclear imaging, proved that the receptor was not saturated by the administration of the radioactive compound.

In order to verify whether the GFP signal could interfere with the IRDye800 channel or vice versa, GFP[+] tumor-bearing mice were subjected to FLI in the IRDye800 channel (excitation wavelength = 774 nm, emission wavelength = 789 nm; filter cut off = 780–815 nm). Non-GFP[+] tumor-bearing mice were injected with the IRDye800-coupled nanobody and imaged within the GFP-channel. There was no interference observed between the channels in either group.

Since the fluorescently labeled nanobody could target all the GFP[+] regions in isolated brains, image-guided dissections using the Fluobeam800 device could be used to isolate the tumor from the brain in a stricter way. This strategy allowed the real-time imaging of the fluorescent compound within the mice and the isolated brains during dissections (**figure 5.23**). The isolated tumor mass was much smaller compared to the experiment in which the GFP-based approach was used alone. Consequently, the obtained *ex vivo* biodistribution results should be more reliable.

In order to validate the effectiveness of this approach, tumor isolation based on the GFP signal of the inoculated tumor cells was compared to isolation by localization of the Nb2Rs15d-IRDye800 using image-guided dissections, in the same model. *Ex vivo* biodistribution results do show an elevated tumor uptake of the radioactive tracer in the group

that underwent the optical imaging-guided dissections (0.797 ± 0.366 % IA/g tumor) compared to the group in which only the GFP signal of the cancer cells was used (0.556 ± 0.282 % IA/g tumor) (**figure 5.24**). This difference was however not confirmed by statistical significance. No difference in brain uptake was observed in between the two groups: 0.037 ± 0.010 % IA/g brain in the Nb-IRDye800-aided group and 0.038 ± 0.008 % IA/g brain in the solely GFP-based dissections.
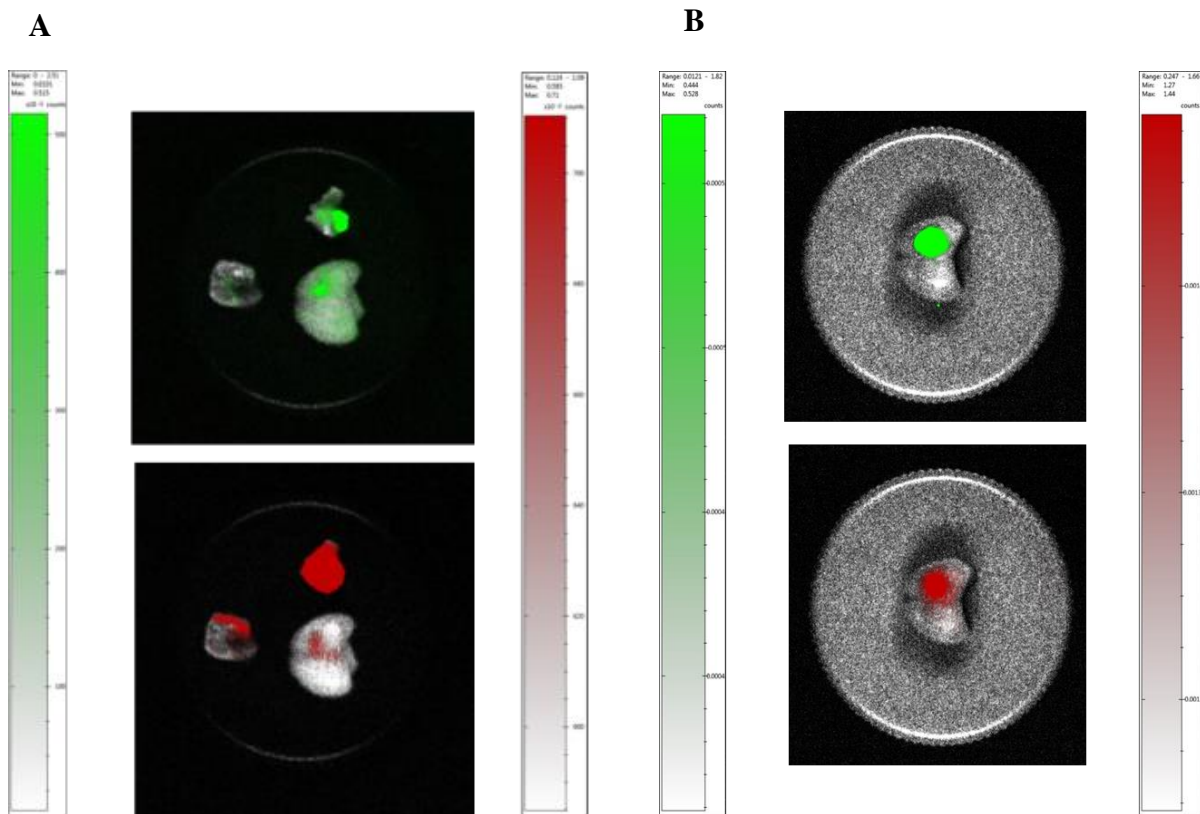
Figure 5.22: FLI images of the brains with an intracranial GFP$^+$ HER2$^+$ MDA-MB-231Br tumor, both for localization of GFP-positive cells (upper, green) as for localization of the IRDye800-coupled nanobody (lower, red). An overlap in tumor location (GFP$^+$ in green) and Nb-2Rs15d-IRDye800 distribution (red) is observed within the brains in both the mice imaged with ^{111}In-DTPA-trastuzumab *(A)* and with ^{111}In-DTPA-Nb2Rs15d *(B)*. Therefore, it is justified to use fluorescent imaging and the localization of IRDye800 for tumor isolation during dissections.

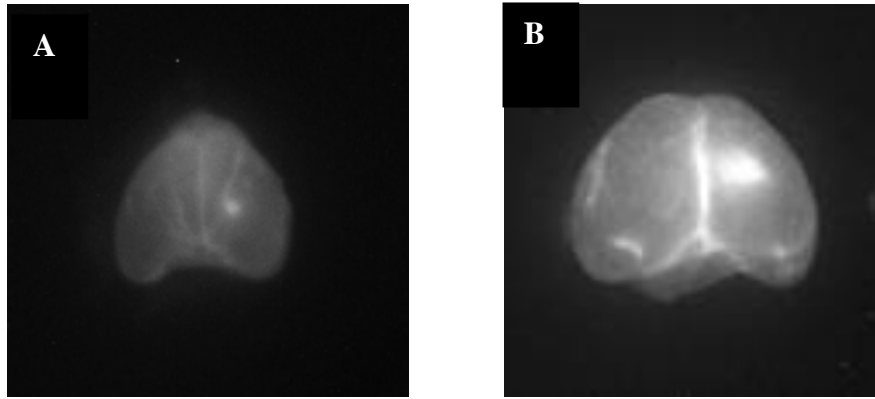***Figure 5.23: Images of isolated mice brains after injection with Nb2Rs15d-IRDye800, acquired with the Fluobeam800 device during dissections.*** *Since in FLI, an overlap in tumor location (GFP$^+$) and Nb-2Rs15d-IRDye800 distribution was observed within the brains of both the mice imaged with Nb2Rs15d-DTPA-^{111}In **(A)** and with trastuzumab-DTPA-^{111}In **(B)**, the images obtained with the Fluobeam800, as shown here, could be used for tumor isolation in real time.*
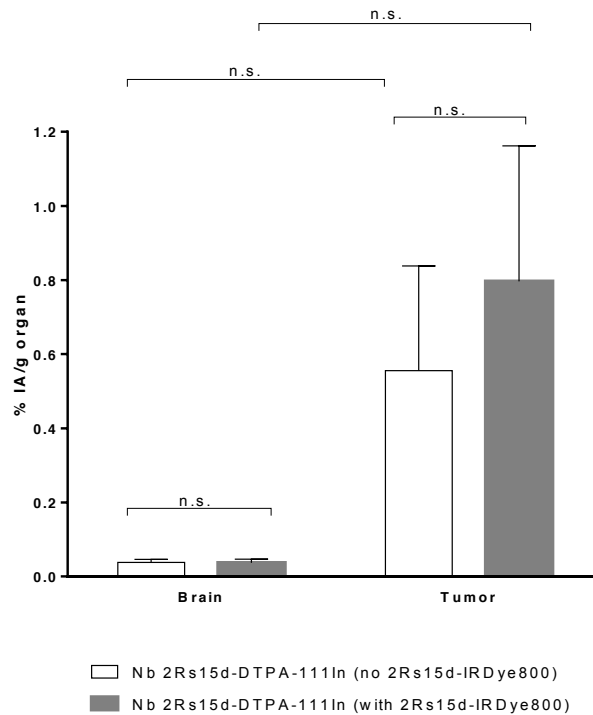
Figure 5.24: Ex vivo biodistribution results of the targeted nuclear imaging experiment with Nb2Rs15d-DTPA-^{111}In in mice brearing HER2$^+$ MDA-MB-231 brain tumors, after tumor isolation aided with (grey) and without (white) targeted fluorescent imaging. *Mean values with SEM of the percentages of injected activity per gram organ are displayed for both the brain and the tumor. No significant differences were observed as determined by a two-tailed unpaired t-test.*

These results are complementary to previously obtained data with this fluorescent tracer, namely that the fluorescently labeled anti-HER2 nanobody can not only target peripheral tumor lesions, as described by Debie and co-workers (Debie, et al., 2018), but also intracranial tumor lesions. Therefore, our data suggest that this fluorescent probe could contribute to the field of image-guided surgery in the case of brain metastases or brain tumors.

6. Conclusion

It was concluded that the generation of EGFRvIII-specific nanobodies via conventional panning and screening methods is difficult and possibly biased due to an altered conformation of the coated antigen in the region of the targeted epitope. This hypothesis is supported since cherry-picked clones, from every panning round, were screened, and all positives in ELISA were identified as only two different VHHs, and these VHHs differed by only one single E to K mutation in their CDR3. This indicates that indeed a strong selection took place for these VHHs during panning and screening. The notion that these binders fail to bind cell-expressed antigen in flow cytometry, or to covalently coupled recombinant antigen in SPR, even though they were highly selected for, let us assume that there is a conformational shift among the antigen coated on plastic and that on the SPR chip or on cells. A biopanning on antigen, either in solution or in the cell-expressed form, might lead to a selection of nanobodies that bind the correct antigen conformation. A screening approach of individual clones that is based on the antigen in the correct form will be important as well. If no binder can be obtained from these amended selection strategies, the possibility that the EGFRvIII-specific epitope in its native form is not antigenic for camelid HCAbs should be considered.

Concerning the radioimmune targeting of the wt hEGF receptor in a preclinical model of glioma, it was concluded that the coupling of DTPA to the nanobody – which is needed to label the proteins with radiometals such as ^{111}In or ^{177}Lu – abolished the targeting potential of the hEGFR-specific nanobody. Since specific targeting of another nanobody – the anti-HER2 Nb2Rs15d, radiolabeled via the same chemistry did show brain tumor-targeting potential in a HER2^{+} MDA-MB-231Br BCBM model, it was discovered that the problem is not caused by the labeling procedure. Rather than that, the problem is thought to be specific for this particular anti-EGFR nanobody and how it recognizes its target antigen, more specifically in the way that the framework region is important for the proper folding of the paratope. The intended proof-of-concept to show the nanobody' potential in a model of glioblastoma was not achieved with the expected results.

The comparison of brain tumor-targeting potential of nanobodies versus antibodies in a HER2^{+} model of BCBM, showed that both tracers could effectively reach their intracranial target. Tumor uptake of the anti-HER2 antibody was significantly higher compared to the nanobody uptake in absolute values, despite the larger size of antibodies. This occurs since

the clearance of the antibodies from the body takes a longer period, and therefore a long-term source of the radiotracers is present. Both tracers however showed a promising tumor-to-organ and tumor-to-brain contrast on the SPECT/CT images. For nanobodies, this contrast was achieved solely 1 h post injection of the radiotracer, while for antibodies no uptake in the tumor was observed at this time point, but rather accumulation in the liver was seen. At 3 days post injection, the contrast was clear and brain tumor targeting was very potent. In these 3 days however, much radiation is delivered to other organs, and therefore the quick distribution of nanobodies is considered favorable, if the damage to the kidneys can be avoided and tumor-uptake in absolute numbers can be raised. Future research will focus on the time points during tumor development at which nanobodies and antibodies start to reach their target site. Also, there will be a focus on the added value of a nanobody-based TRNT approach in the context of brain tumors that have developed resistance to antibody-based systemic therapy.

Important progress was made during this master thesis in the isolation of brain tumor tissue from healthy brain tissue, a scientifically very important aspect in research that is focused on the radio-immune targeting in tissues where the discrimination of tumor from healthy tissue is not possible by naked eye. We have first shown the added value of working with GFP^+ tumor cells, which can be visualized by FLI techniques. In a second step, we have proven the potential of combining a fluorescently labeled tracer with a radioactive tracer for efficient tumor delineation. Accumulation of this fluorescent tracer was shown to overlap with the localization of GFP-positive tumor cells, as determined by FLI. Therefore, tracer presence could be used to visualize the tumor in real-time during dissections with the help of a fluorescence imaging system. These observations are of great scientific importance, as they may improve brain tumor surgery. The obtained data underline that nanobodies might be suited tracers for image-guided surgery in brain tumors. They can also approve the quantitative reliability of *ex vivo* biodistribution data in radio-immune brain cancer research. In summary, additional proof was generated of the potential of nanobodies with different imaging payloads to reach intracranial tumors.

7. Future perspectives

With regards to the generation of an EGFRvIII-specific nanobody, an alternative selection procedure should be developed to identify a specific binder. This will involve preferably cell-based selections or pannings on antigen in solution. It is warranted to recheck the existing immune library of VHHs for the presence of a nanobody capable of recognizing the receptor in its native conformation, unaffected by any possible effects from the coating procedure of recombinant antigen. Since the antigen needs to be coated on a surface for ELISA as well, a protocol that skips this step and allows direct screening for binders to the soluble or cell-expressed antigen will be necessary.

Regarding the targeting of glioma cells *in vivo*, the anti-EGFR nanobody will need to be labeled with a radionuclide that does not require the coupling to DTPA, such as ^{99m}Tc that can be complexed via the His-tag. Careful selection of other chelators that do not disturb the targeting potential of the nanobody, is required to evaluate this nanobody's potential in a context of glioma. Another approach lies in alternative site-specific labeling techniques, such as those mediated by the Sortase reaction (Massa, et al., 2016). Antigen binding assays in SPR will be needed to validate whether there is an effect on affinity from the conjugation of the chelator, and radioactive *in vitro* cell binding assays are necessary to confirm binding to the target cells before *in vivo* experiments can be undertaken. Another strategy is to use other nanobodies, that recognize the antigen in a different way, and would therefore be less prone to the conjugation of a chelator (Schmitz, et al., 2013).

A next step to be taken in the research concerning BCBM is a radiotherapy experiment to compare the potential of nanobodies and antibodies in terms of enhancing survival time and QoL in mice with HER2$^+$ brain tumors. The hypothesis here is that the nanobody reaches the tumor at an earlier stage of development, due to its smaller size. This experiment is intended to take place at the ICMI lab. Since the nanobody shows low absolute uptake in the brain tumor, but a fast clearance from the body and low non-specific binding, a TRNT approach with nanobody-coupled alpha-particles could also prove added value in a trastuzumab-resistant BCBM context (Dekempeneer, et al., 2016). Models to represent such a context will be developed and the alpha-particle-labeled nanobody will be tested for it efficacy in eliminating the brain tumors.

Furthermore, our work points to the importance of identifying which biomarkers may be of interest for image-guided dissections and surgery in a brain context. It will be valuable to develop fluorescently labeled nanobodies for these selected markers.

Summary

In this master thesis, three goals were pursued: the generation of an EGFRvIII-specific nanobody, obtaining a proof-of-concept for the use of nanobodies in a model of GBM and the comparison of an antibody versus a nanobody as a tracer in a model of BCBM with overexpression of HER2.

EGFRvIII-specific binders recognizing native antigen on cells were not obtained. Our data suggest that this is due to a bias for nanobodies associating to an unnatural conformation of the plastic-coated antigen during panning and selection. A different panning and selection approach are therefore warranted - preferably based on a cell-expressed protein or a soluble form of the antigen - and will be attempted in the future.

The nanobody Nb7C12, identified to associate with hEGFR, expressed by cancer cells, failed to reach its target *in vivo* in a preclinical model of GBM. This has been shown to result from the coupling of the nanobody to the chelator DTPA, which is needed for radiolabeling with ^{111}In and ^{177}Lu. The SPR analysis of the nanobody as well as an *in vitro* binding assay proved that coupling of the chelator abolished the antigen targeting potential of the nanobody. Therefore, no proof-of-concept could be obtained that demonstrated the use of nanobodies in this type of cancer.

The commercially available HER2-specific antibody trastuzumab (Herceptin®) showed to be much more potent to deliver its radioactive cargo to HER2^{+} MDA-MB-231Br brain tumor target cells compared to the anti-HER2 nanobody 2Rs15d. Both tracer entities however showed great tumor-to-brain and tumor-to-background contrast and reached their target molecules *in vivo*, as was observed both by *ex vivo* biodistribution and on the SPECT/CT images. The antibody required several days to reach this contrast, while the nanobody only needed one hour. This makes it interesting to use nanobodies as tracers instead of antibodies, because much lower doses of activity are delivered to healthy tissue because of the shorter time to distribute. It remains to be determined whether the activity, delivered by a nanobody, is sufficient to have an anti-tumor effect and whether the uptake in kidneys is a problem when working with nanobodies labeled with therapeutic isotopes.

During the course of this master thesis, the use of real-time image-guided dissections in a brain tumor context was developed. This has proven to be useful when tumor tissue is hardly distinguishable from healthy tissue, making *ex vivo* biodistribution data not quantitatively reliable. Fluorescently labeled tracers are valuable when isolating tumor tissue from healthy brain tissue.

Samenvatting

In deze masterproef werden drie doelen beoogd: het genereren van een EGFRvIII-specifiek nanobody, een *proof-of-concept* studie voor het gebruik van nanobodies in een *in vivo* preklinisch glioblastomamodel en de vergelijking van antilichamen met *nanobodies* als tracermoleculen in een model van hersenmetastasen van borstkanker waarin een overexpressie van HER2 wordt aangetroffen.

Er werden geen EGFRvIII-specifieke binders geïdentificeerd die het antigen herkennen zoals het wordt uitgedrukt door cellen. Onze resultaten suggereren dat dit komt doordat een bias is ingebouwd in de selectieprocedure: er gebeurt een selectie voor binders die een onnatuurlijke conformatie van het antigen herkennen, hetgeen kan optreden door het antigen te immobiliseren op een plastieken drager. Een andere aanpak van *panning* en selectie, gebaseerd op een eiwit dat in zijn natuurlijke vorm tot expressie wordt gebracht door cellen of op het antigen in oplossing, zal nodig zijn en zal in de toekomst worden getest.

Het nanobody gericht tegen humaan EGFR (Nb7C12), dat wordt uitgedrukt door kankercellen, vertoonde niet potentieel om de kankercellen met de correcte antigen-expressie in de hersenen te bereiken. Er werd aangetoond dat dit een gevolg is van de koppeling van de chelator DTPA aan het nanobody, hetgeen nodig is voor het labelen met de radio-isotopen ^{111}In en ^{177}Lu. De SPR-analyse van het DTPA-gekoppelde nanobody evenals een *in vitro* bindingsstudie hebben aangetoond dat de koppeling van de chelator het antigenbindend potentieel van het nanobody vernietigt. Daarom is er tijdens deze masterproef geen *proof-of-concept* gegenereerd over het gebruik van nanobodies in dit type kanker.

Het commercieel verkrijgbare HER2-specifieke antilichaam trastuzumab (Herceptin$^{®}$) vertoonde een sterker potentieel om HER2^{+} MDA-MB-231Br hersentumor-doelwitcellen te bereiken dan het anti-HER2 nanobody 2Rs15d. Beide tracereenheden vertoonden *in vivo* een goed contrast wat betreft opname in de tumor vergeleken met andere organen en vergeleken met hersenopname. Dit werd zowel waargenomen op de SPECT/CT-beelden als in *ex vivo* biodistributiestudies. Antilichamen geven het gewenste contrast pas na enkele dagen, terwijl nanobodies hier slechts één uur tijd voor nodig hebben. Dat maakt het interessant om nanobodies te gebruiken als tracers, en op die manier de schade aan

gezond weefsel ten gevolge van trage distributie te beperken. Hierbij moet echter nog worden nagegaan of nanobodies die gelabeld zijn met therapeutische isotopen in voldoende mate de hersentumoren bereiken en of het hoge signaal in de nieren een toxiciteitsprobleem vormt.

In de loop van deze masterproef is het gebruik van *real-time* beeldgeleide dissecties ontwikkeld. Dit is nuttig gebleken in gevallen waarin tumorweefsel nauwelijks te onderscheiden is van gezond weefsel, zoals het geval is bij hersentumoren. Daardoor zijn *ex vivo* biodistributiegegevens immers minder kwantitatief betrouwbaar. Er werd aangetoond dat het in deze gevallen toegevoegde waarde geeft om fluorescent gelabelde tracers te gebruiken om te helpen bij het correct isoleren van tumorweefsel.

References

Abbott, N. J. et al., 2010. Structure and function of the blood–brain barrier. *Neurobiology of Disease*, Volume 37, pp. 13-25.

Agarwala, S. S. & Kirkwood, J. M., 2000. Temozolomide, a novel alkylating agent with activity in the central nervous system, may improve the treatment of advanced metastatic melanoma. *The Oncologist*, Volume 5, pp. 144-151.

Aizer, A. A. & Lee, E. Q., 2018. Brain metastases. *Neurologic Clinics*, Volume 36, pp. 557-577.

American Cancer Society, 2015. *Breast cancer facts & figures 2015-2016.*. [Online] Available at: https://www.cancer.org/content/dam/cancer-org/research/cancer-facts-and-statistics/breast-cancer-facts-and-figures/breast-cancer-facts-and-figures-2015-2016.pdf [Accessed 19 August 2018].

An, Z. et al., 2018. Epidermal growth factor receptor and EGFRvIII in glioblastoma: signaling pathways and targeted therapies. *Oncogene*, Volume 37, pp. 1561-1575.

Assi, H., Candolfi, M., Lowenstein, P. R. & Castro, M. G., 2012. Rodent glioma models: intracranial stereotactic allografts and xenografts. *Neuromethods*, Volume 77, pp. 229-243.

Bachelot, T. et al., 2013. Lapatinib plus capecitabine in patients with previously untreated brain metastases from HER2-positive metastatic breast cancer (LANDSCAPE): a single-group phase 2 study. *The Lancet Oncology*, Volume 14, pp. 64-71.

Badr, C. E., 2014. Bioluminescence imaging: basics and practical limitations. *Methods in Molecular Biotechnology*, Volume 1098, pp. 1-18.

Becker, A. et al., 2001. Receptor-targeted optical imaging of tumors with near-infrared fluorescent ligands. *Nature Biotechnology*, Volume 19, pp. 327-331.

Bendell, J. et al., 2003. Central nervous system metastases in women who receive trastuzumab-based therapy for metastatic breast carcinoma. *Cancer*, Volume 15, pp. 2972-2977.

Berghoff, A. S. & Preusser, M., 2018. New developments in brain metastases. *Therapeutic Advances in Neurological Disorders*, Volume 11, pp. 1-14.

Bruce, J. N., Houseplan, E. M. & Kennedy, B., 2009. *Glioblastoma multiforme*, New York, New York, USA: Columbia University College of Physicians and Surgeons.

Bruce, J. N. & Kennedy, B. M., 2017. *Glioblastoma multiforme - prognosis,* Chicago, Illinois, USA: Medscape.

Caljon, G. et al., 2012. Using microdialysis to analyse the passage of monovalent nanobodies through the blood–brain barrier. *Brittish Journal of Pharmacology,* Volume 165, pp. 2341-2353.

Connell, J. et al., 2013. Selective permeabilization of the blood-brain barrier at sites of metastasis. *Journal of the National Cancer Institute,* Volume 105, pp. 1634-1643.

Conrath, K. et al., 2001. Beta-lactamase inhibitors derived from single-domain antibody fragments elicited in the camelidae. *Antimicrobial Agents and Chemotherapy,* Volume 45, pp. 2807-2812.

Dasgupta, A. et al., 2016. Ultrasound-mediated drug delivery to the brain: principles, progress and prospects. *Drug Discovery Today: Technology,* Volume 20, pp. 41-48.

De Genst, E. et al., 2006. Molecular basis for the preferential cleft recognition by dromedary heavy-chain antibodies. *Proceedings of The National Academy of Sciences of the USA,* Volume 103, pp. 4586-4591.

De Vos, J., 2014. Targeting the plaques with camelid cdAbs binding LOX-1. In: *Non-invasive in vivo imaging of atherosclerotic plaques using camelid single-domain antibody fragments as molecular tracers*. Brussels, Belgium: Vrije Universiteit Brussel, pp. 101-121.

De Vos, J., Devoogdt, N., Lahoutte, T. & Muyldermans, S., 2013. Camelid single-domain antibody-fragment engineering for (pre)clinical in vivo molecular imaging applications: adjusting the bullet to its target. *Expert opinion on Biological Therapy,* Volume 13, pp. 1149-1160.

Debie, P. et al., 2017. Effect of dye and conjugation chemistry on the biodistribution profile of near-infrared-labeled nanobodies as tracers for image-guided surgery. *Molecular Pharmaceutics,* Volume 14, pp. 1145-1153.

Debie, P. et al., 2018. Improved debulking of peritoneal tumor implants by near-infrared fluorescent nanobody image guidance in an experimental mouse model. *Molecular Imaging and Biology,* Volume 20, pp. 361-367.

Dekempeneer, Y. et al., 2016. Targeted alpha therapy using short-lived alpha-particles and the promise of nanobodies as targeting vehicle. *Expert Opinion on Biological Therapy,* Volume 16, pp. 1035-1047.

D'Huyvetter, M. et al., 2014a. Targeted radionuclide therapy with a 177Lu-labeled anti-HER2 nanobody. *Theranostics,* Volume 4, pp. 108-720.

D'Huyvetter, M. et al., 2014b. Radiolabeled nanobodies as theranostic tools in targeted radionuclide therapy of cancer. *Expert Opinion on Drug Delivery*, Volume 11, pp. 1939-1954.

Dick Jr., L. W., Kim, C., Qiu, D. & Cheng, K.-C., 2007. Determination of the origin of the N-terminal pyro-glutamate variation in monoclonal antibodies using model peptides. *Biotechnology and Bioengineering*, Volume 97, pp. 544-553.

Dijkers, E. C. et al., 2010. Biodistribution of 89Zr-trastuzumab and PET Imaging of HER2-Positive Lesions in Patients With Metastatic Breast Cancer. *Clinical Pharmacology and Therapeutics*, Volume 87, pp. 586-592.

Ding, L. et al., 2015. Small sized EGFR1 and HER2 specific bifunctional antibody for targeted cancer therapy. *Theranostics*, Volume 5, pp. 378-398.

Dumoulin, M. et al., 2002. Single-domain antibody fragments with high conformational stability. *Protein Science*, Volume 11, p. 500–515.

Fan, C.-H., Lin, C.-Y., Liu, H.-L. & Yeh, C.-K., 2017. Ultrasound targeted CNS gene delivery for Parkinson's disease treatment. *Journal of Controlled Release*, Volume 261, pp. 246-262.

Ferlay, J. et al., 2015. Cancer incidence and mortality worldwide: sources, methods and major patterns in GLOBOCAN 2012. *International journal of Cancer*, Volume 136, p. 359–386.

Fleetwood, F. et al., 2013. Surface display of a single-domain antibody library on Gram-positive bacteria. *Cellular and Molecular Life Sciences*, Volume 70, pp. 1081-1093.

Food and Drug Administration, 2012. *accessdata*. [Online] Available at: https://www.accessdata.fda.gov/drugsatfda_docs/bla/2012/103792orig1s5275.pdf [Accessed 17 8 2018].

Furnari, F. B., Cloughesy, T. F., Cavenee, W. K. & Mischel, P. S., 2015. Heterogeneity of epidermal growth factor receptor signalling networks in glioblastoma. *Nature Reviews Cancer*, Volume 15, pp. 302-310.

Gainkam, L. O. T. et al., 2008. Comparison of the biodistribution and tumor targeting of two 99m Tc-labeled anti-EGFR nanobodies in mice, using pinhole SPECT/Micro-CT. *Journal of Nuclear Medicine*, Volume 49, pp. 788-795.

Gancberg, D. et al., 2002. Comparison of HER-2 status between primary breast cancer and corresponding distant metastatic sites. *Annals of Oncology*, Volume 13, pp. 1036-1043.

Gan, H. K., Cvrljevic, A. N. & Johns, T. G., 2013. The epidermal growth factor receptor variant III (EGFRvIII): where wild things are altered. *The FEBS Journal*, Volume 280, pp. 5350-5370.

Garrett, T. P. et al., 2002. Crystal structure of a truncated epidermal growth factor receptor extracellular domain bound to transforming growth factor α. *Cell*, Volume 110, pp. 763-773.

Gedeon, P. C. et al., 2014. An EGFRvIII-targeted bispecific T-cell engager overcomes limitations of the standard of care for glioblastoma. *Expert Review of Clinical Pharmacology*, Volume 6, pp. 375-386.

Gorovits, B. & Krinos-Fiorotti, C., 2013. Proposed mechanism of off-target toxicity for antibody–drug conjugates driven by mannose receptor uptake. *Cancer Immunology Immunotherapy*, Volume 62, pp. 217-233.

Hamers-Casterman, C. et al., 1993. Naturally occurring antibodies devoid of light chains. *Nature*, Volume 363, p. 446–448.

Han, W. et al., 2006. Hypophosphorylation of residue Y1045 leads to defective downregulation of EGFRvIII. *Cancer Biology and Therapy*, Volume 5, pp. 1361-1368.

Hegi, M. et al., 2005. MGMT gene silencing and benefit from temozolomide in glioblastoma. *The New England journal of Medicine*, Volume 352, pp. 997-1003.

Henriksson, R., Asklund, T. & Poulsen, H. S., 2011. Impact of therapy on quality of life, neurocognitive function and their correlates in gliobastoma multiforme: a review. *Journal of Neuro Oncology*, Volume 104, pp. 639-646.

Hicks, D. G. & Kulkarni, S., 2008. HER2+ breast cancer: review of biologic relevance and optimal use of diagnostic tools. *American Society for Clinical Pathology*, Volume 129, pp. 263-273.

Huang, H. et al., 1997. The enhanced tumorigenic activity of a mutant epidermal growth factor receptor common in human cancers is mediated by threshold levels of constitutive tyrosine phosphorylation and unattenuated signaling. *The Journal of Biological Chemistry*, Volume 272, pp. 2927-2935.

Huang, L. et al., 2008. SPECT imaging with 99mTc-labeled EGFR-specific nanobody for in vivo monitoring of EGFR expression. *Molecular Imaging and Biology*, Volume 10, pp. 167-175.

Huang, P. H., Xu, A. M. & White, F. M., 2009. Oncogenic EGFR signaling networks in glioma. *Science Signaling*, Volume 2, p. re6.

Hussack, G. et al., 2011. Engineered single-domain antibodies with high protease resistance and thermal stability. *PLoS ONE*, Volume 6, p. e28218.

Iqbal, N. & Iqbal, N., 2014. Human epidermal growth factor receptor 2 (HER2) in cancers: overexpression and therapeutic implications. *Molecular Biology International*, Volume 2014, p. e852748.

Iqbal, U. et al., 2010. Molecular imaging of glioblastoma multiforme using anti-insulin-like growth factor-binding protein-7 single-domain antibodies. *British Journal of Cancer*, Volume 103, pp. 1606-1616.

Jain, A. K. et al., 2007. Carbon nanotubes and their toxicity. *Nanotoxicology*, Volume 1, pp. 167-197.

Johnson, D. R. & O'Neill, B. P., 2012. Glioblastoma survival in the United States before and during the temozolomide era. *Journal of Neuro Oncology*, Volume 107, p. 359–364.

Johnson, L. et al., 2015. Rational development and characterization of humanized anti-EGFR variant III chimeric antigen receptor T cells for glioblastoma. *Science Translational Medicine*, Volume 7, p. 275ra22.

Jones, M. L. et al., 2016. Targeting membrane proteins for antibody discovery using phage display. *Nature Scientific Reports*, Volume 6, p. 26240.

Kabraji, S. et al., 2018. Drug resistance in HER2-positive breast cancer brain metastases: blame the barrier or the brain?. *Clinical Cancer Research*, Volume 24, pp. 1795-1804.

Keyaerts, M. et al., 2016. Phase I study of 68Ga-HER2-nanobody for PET/CT assessment of HER2 expression in breast carcinoma. *Journal of Nuclear Medicine*, Volume 57, pp. 27-33.

Kluba, C. A. & Mindt, T. L., 2013. Click-to-chelate: development of technetium and rhenium-tricarbonyl labeled radiopharmaceuticals. *Molecules*, Volume 18, pp. 3206-3226.

Kodack, D. P. et al., 2015. Emerging strategies for treating brain metastases from breast cancer. *Cancer Cell*, Volume 27, pp. 163-175.

Krasniqi, A. et al., 2017. Theranostic radiolabeled anti-CD20 sdAb for targeted radionuclide therapy of non-hodgkin lymphoma. *Molecular Cancer Therapeutics*, Volume 16, pp. 2828-2839.

Krüwel, T. et al., 2016. In vivo detection of small tumour lesions by multi-pinhole SPECT applying a 99mTc-labelled nanobody targeting the Epidermal Growth Factor Receptor. *Scientific Reports*, Volume 6, p. e21834 .

Lal, A. et al., 2002. Mutant epidermal growth factor receptor up-regulates molecular effectors of tumor invasion. *Cancer Research*, Volume 62, pp. 3335-3339.

Lemaire, M. et al., 2013. Imaging and radioimmunotherapy of multiple myeloma with anti-idiotypic Nanobodies. *Leukemia*, Volume 28, pp. 444-447.

Leone, J. P. & Leone, B. A., 2015. Breast cancer brain metastases: the last frontier. *Experimental Hematology & Oncology*, Volume 4.

Li, J. et al., 1997. PTEN, a putative protein tyrosine phosphatase gene mutated in human brain, breast, and prostate cancer. *Science*, Volume 275, pp. 1943-1947.

Li, T. et al., 2016. Camelid single-domain antibodies: a versatile tool for in vivo imaging of extracelluar and intracellular brain targets. *Journal of Controlled Diseases*, Volume 243, pp. 1-10.

Liu, S. & Edwards, D. S., 2001. Synthesis and characterization of two 111In-labeled DTPA-peptide conjugates. *Bioconjugate Chemistry*, Volume 12, pp. 630-634.

Lockman, P. et al., 2010. Heterogeneous blood-tumor barrier permeability determines drug efficacy in experimental brain metastases of breast cancer. *Clinical Cancer Research*, Volume 16, pp. 5664-5678.

Louis, D. N. et al., 2007. The 2007 WHO classification of tumours of the central nervous system. *Acta Neuropathologica*, Volume 114, pp. 97-109.

Luwor, R. et al., 2004. The tumor-specific de2-7 epidermal growth factor receptor (EGFR) promotes cells survival and heterodimerizes with the wild-type EGFR. *Oncogene*, Volume 23, pp. 6095-6104.

Macrocyclics, 2018. *Bifinctional Chelators (BFCs)*. [Online] Available at: https://www.macrocyclics.com/online-catalog/bifunctional-chelators-bfcs/p-scn-bn-chx-a-dtpa/

Malikki, H., 2016. Trial Watch: glioblastoma vaccine therapy disappointment in phase III trial. *Nature Reviews Neurology*, Volume 12, p. 190.

Massa, S. et al., 2016. Sortase A-mediated site-specific labeling of camelid single-domain antibody-fragments: a versatile strategy for multiple molecular imaging modalities. *Contrast Media and Molecular Imaging*, Volume 11, pp. 328-339.

Massa, S. et al., 2014. Site-specific labeling of cysteine-tagged camelid single-domain antibody-fragments for use in molecular imaging. *Bioconjugate Chemistry*, Volume 25, pp. 979-988.

McMurphy, T. et al., 2014. The anti-tumor activity of a neutralizing nanobody targeting leptin receptor in a mouse model of melanoma. *PLoS One*, Volume 28, p. e89895.

Melchers, L. J. et al., 2014. Head and neck squamous cell carcinomas do not express EGFRvIII. *International Journal of Radiation Oncology, Biology, Physics*, Volume 90, pp. 454-462.

Messaoudi, K., Clavreul, A. & Lagarce, F., 2015. Toward an effective strategy in glioblastoma treatment. Part I: resistance mechanisms and strategies to overcome resistance of glioblastoma to temozolomide. *Drug Discovery Today*, Volume 20, pp. 899-905.

Muyldermans, S., 2001. Single domain camel antibodies: current status. *Reviews in Molecular Biotechnology*, Volume 74, pp. 277-304.

Muyldermans, S., 2013. Nanobodies: natural single-domain antibodies. *Annual Review of Biochemistry*, Volume 82, pp. 775-797.

Nagane, M. et al., 1996. A common mutant epidermal growth factor receptor confers enhanced tumorigenicity on human glioblastoma cells by increasing proliferation and reducing apoptosis. *Cancer Research,* Volume 56, pp. 5079-5086.

National Brain Tumor Society, 2018. *Quick Brain Tumor Facts*. [Online] Available at: http://braintumor.org/brain-tumor-information/brain-tumor-facts/ [Accessed 14 8 2018].

National Institute of Biomedical Imaging and Bioengineering, 2016. *Nuclear Medicine*. [Online] Available at: https://www.nibib.nih.gov/science-education/science-topics/nuclear-medicine [Accessed 13 December 2017].

National Institute of Biomedical Imaging and Bioengineering, n.d. *Computed Tomography (CT)*. [Online] Available at: https://www.nibib.nih.gov/science-education/science-topics/computed-tomography-ct [Accessed 13 December 2017].

Neyns, B. et al., 2009. Stratified phase II trial of cetuximab in patients with recurrent high-grade glioma. *Annals of oncology*, pp. 1596-1603.

Niwinska, A., Murawska, M. & Pogoda, K., 2010. Breast cancer brain metastases: differences in survival depending on biological subtype, RPA RTOG prognostic class and systemic treatment after whole-brain radiotherapy (WBRT). *Annals of Oncology*, Volume 21, pp. 294-298.

Ogawa, K. et al., 2008. Treatment and prognosis of brain metastases from breast cancer. *Journal of Neuro-Oncology*, Volume 231-238, p. 86.

Omidfar, K. et al., 2009. Expression of EGFRvIII in thyroid carcinoma: immunohistochemical study by camel antibodies. *Immunological Investigations*, Volume 38, pp. 165-180.

Omidfar, K. et al., 2004. Production of a novel camel single-domain antibody specific for the type III mutant EGFR. *Tumor Biology*, Volume 25, pp. 296-305.

Park, C.-K.et al., 2012. The changes in MGMT promoter methylation status in initial and recurrent glioblastomas. *Translational Oncology*, Volume 5, pp. 393-397.

Percy, D. et al., 2011. In vivo characterization of changing blood-tumor barrier permeability in a mouse model of breast cancer metastasis: a complementary magnetic resonance imaging approach. *Investigative Radiology*, Volume 46, pp. 718-725.

Rösch, F., Herzog, H. & Qaim, S. M., 2017. The beginning and development of the theranostic approach in nuclear medicine, as exemplified by the radionuclide pair 86Y and 90Y. *Radiopharmaceuticals*, Volume 10, p. E56.

Saerens, D., Conrath, K., Govaert, J. & Muyldermans, S., 2008. Disulfide bond introduction for general stabilization of immunoglobulin heavy-chain variable domains. *Journal of Molecular Biology*, Volume 377, pp. 478-488.

Sampson, J. et al., 2010. Immunologic escape after prolonged progression-free survival with epidermal growth factor receptor variant III peptide vaccination in patients with newly diagnosed glioblastoma. *Journal of Clinical Oncology*, Volume 28, pp. 4722-4729.

Sanai, N., Alvarez-Buylla, A. & Berger, M. S., 2005. Neural stem cells and the origin of gliomas. *The New England Journal of Medicine*, Volume 353, pp. 811-822.

Sanovich, E. et al., 1995. Pathway across blood-brain barrier opened by the bradykinin agonist, RMP-7. *Brain Research*, Volume 705, pp. 125-135.

Scarpa, L. et al., 2016. The 68Ga/177Lu theragnostic concept in PSMA targeting of castration-resistant prostate cancer: correlation of SUVmax values and absorbed dose estimates. *European Journal of Medical Molecular Imaging*, Volume 44, pp. 788-800.

Schmitz, K. R. et al., 2013. Structural evaluation of EGFR inhibition mechanisms for nanobodies/VHH domains. *Structure*, Volume 21, pp. 1214-1224.

Serlin, Y., Shelef, I., Knyazer, B. & Friedman, A., 2015. Anatomy and physiology of the blood-brain barrier. *Seminars in Cell & Developmental Biology*, Volume 38, pp. 2-6.

Seshacharyulu, P. et al., 2012. Targeting the EGFR signaling pathway in cancer therapy. *Expert Opinion on Therapeutic Targets*, Volume 16, pp. 15-31.

Shaw, R. J., 2006. Glucose metabolism and cancer. *Current opinion in Cell Biology*, Volume 18, pp. 598-608.

Sherriff, J. et al., 2013. Patterns of relapse in glioblastoma multiforme following concomitant chemotherapy with temozolomide. *The British journal of radiology*, Volume 86, p. 20120414.

Shinojima, N. et al., 2003. Prognostic value of epidermal growth factor receptor in patients with glioblastoma multiforme. *Cancer Research*, Volume 63, pp. 6962-6970.

Siegal, T. et al., 2000. In vivo assessment of the window of barrier opening after osmotic blood–brain barrier disruption in humans. *Journal of Neurosurgery*, Volume 92, pp. 599-605.

Silberstein, E. B., 2012. Radioiodine: the classic theranostic agent. *Seminars in Nuclear Medicine,* Volume 42, pp. 164-170.

Slobbe, P. et al., 2015. A comparative PET imaging study with the reversible and irreversible EGFR tyrosine kinase inhibitors [11C]erlotinib and [18F]afatinib in lung cancer-bearing mice. *European Journal of Nuclear Medicine and Molecular Imaging,* Volume 5, p. 14.

Snoeck, V., 2013. *Current experience in immunogenicity assessment of next generation biologics-nanobodies.* European Immunogenicity Symposium, Ablynx NV.

Society of Nuclear Medicine and Molecular Imaging, n.d. *Fact sheet: what is nuclear medicine and molecular imaging?.* [Online] Available at: http://www.snmmi.org/AboutSNMMI/Content.aspx?ItemNumber=15627 [Accessed 13 December 2017].

Steeland, S., Vandenbroucke, R. E. & Libert, C., 2016. Nanobodies as therapeutics: big opportunities for small antibodies. *Drug Discovery Today,* Volume 21, pp. 1076-1113.

Stemmler, H. et al., 2006. Characteristics of patients with brain metastases receiving trastuzumab for HER2 overexpressing metastatic breast cancer. *Breast,* Volume 15, pp. 219-225.

Structural Biology Brussels, 2008. *Nanobody-aided crystallography.* [Online] Available at: http://www.structuralbiology.be/chaperones [Accessed 2 December 2017].

The American Cancer Society Medical and Editorial Content Team, 2017. *Treating breast cancer.* [Online] Available at: https://www.cancer.org/cancer/breast-cancer/treatment.html [Accessed 16 Februari 2018].

Theile, C. S. et al., 2013. Site-specific N-terminal labeling of proteins using sortase-mediated reactions. *Nature Protocols,* Volume 8, pp. 1800-1807.

U.S. National Library of Medicine, 2018. *Clinical trials.* [Online] Available at: https://clinicaltrials.gov/ct2/show/NCT02209376?term=NCT02209376&rank=1 [Accessed 18 8 2018].

Ullrich, R. T. et al., 2009. Methyl-L-11C-methionine PET as a diagnostic marker for malignant progression in patients with glioma. *Journal of Nuclear Medicine,* Volume 50, pp. 1962-1968.

Vallabhajosula, S., Killeen, R. P. & Osborne, J. R., 2010. Altered biodistribution of radiopharmaceuticals: role of radiochemical/pharmaceutical purity, physiological, and pharmacologic factors. *Seminars in Nuclear Medicine,* Volume 40, pp. 220-241.

van Tellingen, O. et al., 2015. Overcoming the blood-brain tumor barrier for effective glioblastoma treatment. *Drug Resistance Updates*, Volume 19, pp. 1-12.

Vaneycken, I. et al., 2011a. Preclinical screening of anti-HER2 nanobodies for molecular imaging of breast cancer. *The FASEB Journal*, Volume 25, pp. 2433-2446.

Vaneycken, I. et al., 2011b. Immuno-imaging using nanobodies. *Current opinion in Biotechnology*, Volume 22, pp. 877-881.

Vaneycken, I. et al., 2010. In vitro analysis and in vivo tumor targeting of a humanized, grafted nanobody in mice using pinhole SPECT/micro-CT. *Journal of Nuclear Medicine*, Volume 51, pp. 1099-1106.

Vaz-Luis, I. et al., 2012. Impact of hormone receptor status on patterns of recurrence and clinical outcomes among patients with human epidermal growth factor-2-positive breast cancer in the National Comprehensive Cancer Network: a prospective cohort study. *Breast Cancer Research*, Volume 14, p. R129.

Verma, S., 2014. Advances in treating HER2-positive breast cancer: an interview with Sunil Verma. *BioMed Central Medicine*, Volume 12, p. 129.

Verma, V. et al., 2018. Biotin-tagged proteins: reagents for efficient ELISA-based serodiagnosis and phage display-based affinity selection. *PLoS One*, Volume 13, p. e0191315.

Vincke, C. et al., 2012. Generation of single domain antibody fragments derived from camelids and generation of manifold constructs. *Methods in Molecular Biology*, Volume 907, pp. 145-176.

Vincke, C. et al., 2009. General strategy to humanize a camelid single-domain antibody and identification of a universal humanized nanobody scaffold. *The Journal of Biological Chemistry*, Volume 284, pp. 3273-3284.

Vriesendorp, H. M. & Vriesendorp, F. J., 2003. A review of the intravenous administration of radiolabeled immunoglobulin G to cancer patients. High or low protein dose?. *Cancer Biotherapy and Radiopharmaceuticals*, Volume 18, pp. 35-46.

Vrije Universiteit Brussel, 2015. *Phase II clinical trial of 68Ga-anti-HER2-Nanobody PET/CT: validation of an innovative imaging technique to optimize patient selection for HER2-targeted therapy in breast carcinoma*. [Online] Available at: https://cris.vub.be/en/projects/phase-ii-clinical-trial-of-68gaantiher2nanobody-petct-validation-of-an-innovative-imaging-technique-to-optimize-patient-selection-for-her2targeted-therapy-in-breast-carcinoma(d326d395-9659-4135-ad20-a0c44598c784).html [Accessed 17 8 2018].

Walid, M. S., 2008. Prognostic factors for long-term survival after glioblastoma. *The Permanente Journal,* Volume 12, pp. 45-48.

Weller, M. et al., 2017. Rindopepimut with temozolomide for patients with newly diagnosed, EGFRvIII-expressing glioblastoma (ACT IV): a randomised, double-blind, international phase 3 trial. *The Lancet. Oncology,* Volume 18, pp. 1373-1385.

Wen, P. Y. & Kesari, S., 2008. Malignant gliomas in adults. *The New England Journal of Medicine,* Volume 359, pp. 492-507.

Werner, R. A. et al., 2015. 68Gallium- and 90Yttrium-/177Lutetium: ''theranostic twins'' for diagnosis and treatment of NETs. *Annals of Nuclear Medicine,* Volume 1-7, p. 29.

Wikstrand, C. et al., 1998. The class III variant of the epidermal growth factor receptor (EGFRvIII): characterization and utilization as an immunotherapeutic target. *Journal of Neurovirology,* Volume 4, pp. 148-158.

Xavier, C. et al., 2012. Site-specific labeling of His-tagged nanobodies with 99mTc: a practical guide. *Methods in Molecular Biology,* Volume 911, pp. 485-490.

Yarden, Y., 2001. EGFR family and its ligands in human cancer: signalling mechanisms and therapeutic opportunities. *European Journal of Cancer,* Volume 37, pp. S3-S8.

Yip, S. et al., 2009. MSH6 mutations arise in glioblastomas during temozolomide therapy and mediate temozolomide resistance. *Clinical Cancer Research,* Volume 15, pp. 4622-4629.

Zahonero, C. et al., 2015. Preclinical test of dacomitinib, an irreversible EGFR inhibitor, confirms its effectiveness for glioblastoma. *Molecular Cancer Therapeutics,* Volume 14, pp. 1548-1558.

Zhu, M. et al., 2014. Combining magnetic nanoparticle with biotinylated nanobodies for rapid and sensitive detection of influenza H3N2. *Nanoscale Research Letters,* Volume 9, p. 528.